1-24-2024

# Broadband and Multiband Designs for Antenna Feeds and Arrays

Jeremy Michael Furgal
*Syracuse University*

# ABSTRACT

The designs for broadband and multiband antenna feeds, specifically for antenna array applications, are fabricated and evaluated to optimize the performance of these arrays. A specific power divider functionality is expanded upon for layout flexibility and amplitude tapering. A method of multiplexing antennas is used to overcome limitations caused by element spacing in arrays.

A planar power divider that has wide bandwidth performance (at least 30% BW) and uses resistors that are tied to ground is analyzed. This particular power divider has previously only been solved for the equal split 2-way case. This work simplifies the structure of the original design and then leverages that simplicity to expand the capability of the power divider for *N*-way, unequal spilt and wider bandwidth cases. A 4-way power divider, an unequal split power divider with a 2:1 power split ratio and wider band power divider with 50% bandwidth are all simulated and experimentally verified with fabricated prototypes.

However, for wider bandwidth arrays (or multiband array covering a wide bandwidth) the spacing between antenna elements becomes an issue since it can only be optimized at a single frequency. A method to overcome this limitation is presented. This method uses separate antenna elements multiplexed with isolation circuits. These antennas are treated as a single element for the design of an antenna feed. This is demonstrated with a 3 band 1D scanning array prototype of patch antennas that is validated through testing. The concept is then expanded for 2D scanning by using frequency scanning antennas. Since frequency scanning antennas do not have a sufficient stop band needed for multiplexing, an antenna with improved out of band rejection is designed for use in this type of array. A prototype of this antenna is fabricated and validated through testing.

This practical research is supported by extensive simulations and validation through prototypes. The measurements show good agreement with the simulations for the expanded power dividers showing their potential to be used in antenna feed networks. The multiband antenna array measurements show good agreement with simulation, proving it to be a good solution for array deployments. The frequency scanning antenna with improved out of band rejection measurements also shows good agreement with simulation, proving its potential to expand the previous multiband array to 2D scanning.

# BROADBAND AND MULTIBAND DESIGNS FOR ANTENNA FEEDS AND ARRAYS

by

Jeremy Michael Furgal

B.S., Syracuse University, 2007
M.S., Syracuse University, 2012

Dissertation

Submitted in partial fulfillment of the requirements for the degree of

Doctor of Philosophy in Electrical and Computer Engineering.

Syracuse University

December 2023

“If at first the idea is not absurd, then there is no hope for it“

Albert Einstein, Theoretical Physicist

“I have not failed. I’ve just found 10,000 ways that won’t work“

Thomas Edison, Inventor

To my wife, *Sarah*, for her patience and for the sacrifices she made throughout this journey.

# ACKNOWLEDGMENTS

I would like to express my gratitude to my advisor Prof. Jay Kyoon Lee, for seeing me through this last leg of my academic journey. He was my advisor when I first joined Syracuse University as an undergrad, so I am grateful that he could be my advisor again as I finish before he retires. I am also grateful to my co-advisor Prof. Jun Hwan Choi for guiding me through this journey these past few years and in particular for recognizing the challenges associated with working on a doctoral degree part time while working full time.

I would like to recognize Prof. Ercument Arvas who served as my adviser for my master's degree at Syracuse University. It was also him who connected me with TTM Technologies (formerly Anaren Microwave) which is where I am still employed 15 years later. I'm also thankful to TTM Technologies which has financially supported my doctoral studies and allowed me time to attend conferences to present my papers.

I would also like to thank Dr. Hanseung Lee for collaboration early on in my research. His consulting helped guide the direction of the multiband array research.

I am thankful to Prof. Younes Ra'di and Prof. M. Cenk Gursoy for serving as Committee members and dedicating time to review and comment on this dissertation. I am also grateful to Prof. Jeongmin Ahn for participating as Chair of the Oral Examination Committee and representing the Graduate School.

A special acknowledgment is dedicated to my wife Sarah who has been very supportive throughout this process and has made countless sacrifices to allow me to finish my research.

# CONTENTS

# LIST OF FIGURES

# LIST OF TABLES

# Chapter 1. Introduction

The topic that is discussed in this dissertation is broadband and multiband designs for antenna feeds for antenna arrays. The research is split into two parts depending on the operational bandwidth. For bandwidths less than or equal to 30%, a broadband power divider is investigated for an antenna feed of an array with single element spacing. For bandwidths larger than 30%, a technique to implement multiple antennas using a multiplex antenna feed is used in order to achieve multiple element spacing distances and maintain the proper performance of the array.

Broadband and multiband designs are important as modern systems are becoming more integrated in both commercial and military applications. Commercial applications, such as cell phones and automobiles, use different communication systems, such as 5G, GPS, V2X and Wi-Fi, and military radar uses distinct bands, such as L, S, C, X and Ku for different applications [1] [2]. These different functions and frequency bands have a wide frequency span and will require broadband antennas or separate antennas for complete coverage. GPS functions around 1.5 GHz while 5G applications could be 30 GHz or more. L-band is 1-2 GHz while Ku-band is 12-18 GHz.

Antenna systems are often implemented as arrays, or groups of antennas that operate together as a single antenna. These are utilized because they provide a more directive beam than that of a single antenna element and also provide the ability to electrically steer the beam provided that the phase between element feeds can be controlled [3]. Electrically steering the beam is superior to mechanical steering of the array because of the challenge of precisely moving such a large mass and having to manage the position of the antenna. For proper array operation, the relative spacing between elements in the array is a critical parameter which will be fixed and can only be optimized at one frequency. Also, the amplitude distribution between antenna elements can optimize the

performance of the array, specifically the side lobes of the array pattern. The details on how these parameters affect the performance of the array are explained in Chapter 2.

When the operating bandwidth is less than 30%, an array with a single element spacing will operate properly. In Chapter 3 a power divider that is capable of 30% BW that could be used in an antenna feed is analyzed and evaluated. This power divider has previously only been designed for 2-way equal power split cases [4]. This work expands this power divider to have multiple outputs, have unequal power split ratios and widening the bandwidth even further. Using a power divider with an arbitrary number of outputs can make a smaller footprint compared to cascading multiple 2-way power dividers. This is helpful for layouts that have tight space constraints. The unequal split power ratio can be used in feed networks with arbitrary amplitude distributions at the elements for optimization of side lobes. And the wider bandwidth cases extend the bandwidth to 50% and 60%.

When operating beyond 30% bandwidth (the difference between the minimum and maximum operating wavelength becomes large), the spacing of the antenna elements will start impacting the array performance. This can often be the case when combining functions into a single system since different bands work better for different functions. One such example is a target acquisition and tracking radar. L and S-bands work best for acquisition and X-band is best for tracking [5]. This could be a bandwidth of up to 170% to cover both functions and while a wideband antenna could be designed to cover the bandwidth, the elements in an array would not have optimal spacing for all frequencies.

A method to overcome this limitation is presented in Chapter 4. It uses multiband antennas with separate radiating elements that can be placed independently from the other radiators. These antennas could be used in an array with optimal element spacing for each band. The array will now

function properly at each band since the spacing can be optimized for each band. This concept is demonstrated with a 3 band, 1D scanning array implemented with patch antennas in a linear configuration using isolation networks to multiplex the antennas. The design and results will be discussed in this chapter. The concept is then expanded for 2D scanning capability. This uses frequency scanning antennas to add the additional scanning dimension while still using a linear configuration of antenna elements. The challenge introduced with using frequency scanning antennas in this way is that they do not have sufficient out of band rejection needed for multiplexing. An antenna that possesses frequency scanning capability and has sufficient out of band rejection is proposed and created. The design of this antenna and its results will also be discussed.

A conclusion is presented in Chapter 5 which summarizes the research contributions as well as providing potential areas of future research.

# Chapter 2. Fundamental Topics

## 2.1. Phased Array Antennas

Antenna arrays are groups of antennas arranged in space in order to produce a directive beam of radiation. The theory of antenna arrays is covered in [6] and [7]. The antennas are fed with a feed network that controls the phase and amplitude at each of the antennas. The phasing between elements controls how the fields of the individual elements combine in space, whether they add constructively or destructively, to steer a beam of radiation toward the desired direction. This can be achieved with different beamforming techniques discussed in the next section.

The number of elements in the array control the width of the beam. The number of elements will also decrease the level of the side lobes. With an increase in the number of elements the beam width narrows and the side lobe levels are reduced as illustrated in Figure 2-1. Element spacing is at $\lambda_0/2$ for this example, where $\lambda_0$ is the wavelength in free space at the operating frequency.

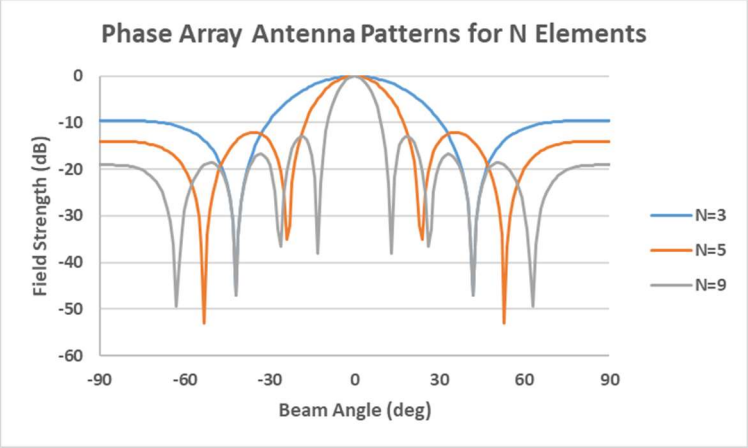


Figure 2-1 Linear phase array antenna pattern for different number of elements.

The spacing between the elements in an antenna array is a critical parameter in beam steering

applications. With the spacing too close, the main lobe becomes wider and the mutual coupling level between the antenna elements is increased. With the spacing too far apart, early onset of grating lobes will appear in the field of view as the beam is steered. The optimum element spacing is a half wavelength. This is illustrated in Figure 2-2 where d is the spacing of the antenna elements in terms of wavelength $\lambda$.

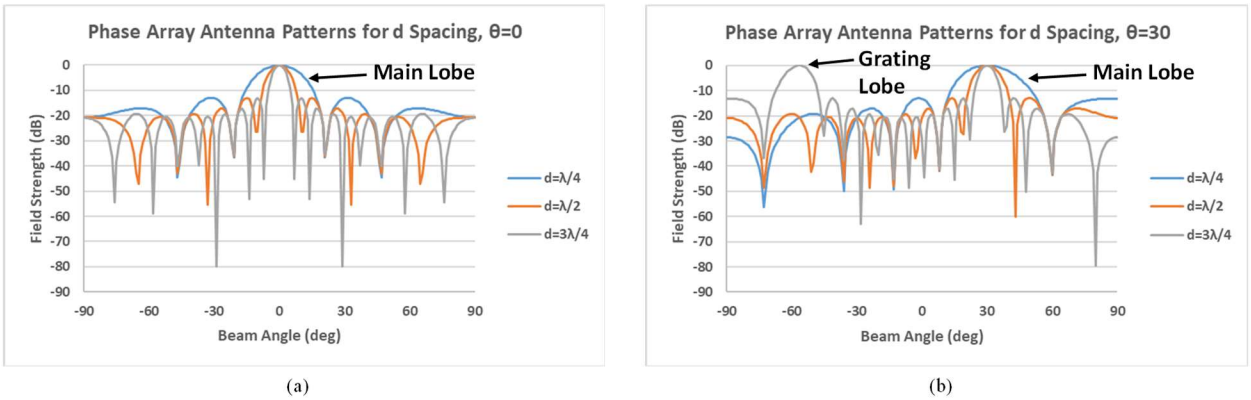


Figure 2-2 Linear phase array antenna pattern for different element spacing a) for broadside and b) for 30° steering.

The required phase difference between the elements to obtain a certain direction of beam can be solved geometrically for a linear array. This can be seen in Figure 2-3. The derived equation is shown in Eq. (2.1).

$$\Delta\Phi = \frac{360^{\circ} \cdot d \cdot \sin(\theta)}{\lambda_0} \tag{2.1}$$

where $\Delta\Phi$ is the phase difference between the elements, $d$ is the physical spacing between elements, $\theta$ is the angle of the main beam and $\lambda_0$ is the wavelength in free space at the operating frequency.

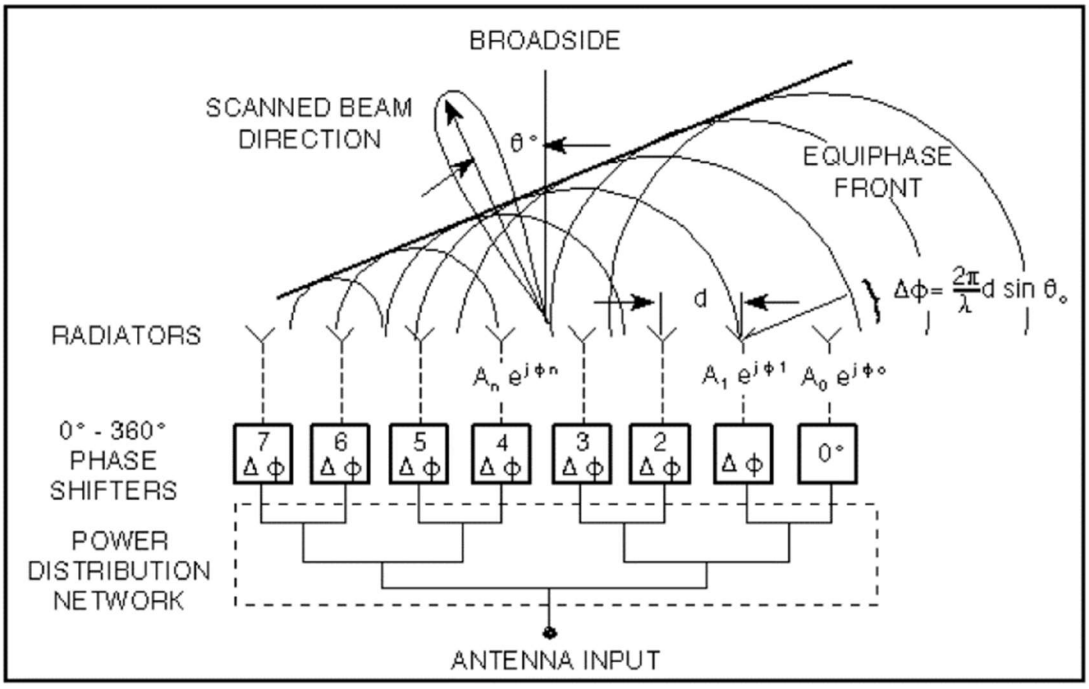


Figure 2-3 Annotated linear phased array [8].

The grating lobes are what limit the highest frequency (from the center frequency) that the array can operate. The largest scan angle also contributes to this higher frequency limit. A higher scan angle can be achieved using a frequency closer to the center frequency and a higher frequency can be used if the maximum scan angle is reduced [9].

A transformation that often occurs in electrical engineering is the Fourier transform of a rectangular pulse in one domain to a sinc pulse in another. This transform of the rectangular pulse (also known as the uniform unit pulse or the Pi function) is shown in Eq. 2.2 and is shown graphically in Figure 2-4.

$$\Pi(t) \overset{\mathcal{F}}{\Rightarrow} sinc(\omega) \tag{2.2}$$

For an antenna array, this relation occurs between the spatial domain, specifically between the power distribution at the elements of the array and the radiation pattern. If the power to the

elements in an array is applied equally, the array is said to have no weighting. For this case the first side lobe will be at -13dBc, where dBc is the power ratio of a signal to a carrier signal (the main beam in this case), expressed in decibels. By applying a type of weighting across the elements of the array, the sidelobes can be reduced at the expense of the main beam. An example of a Hanning weighting function (in the space domain for antenna problems) is shown in Figure 2-5. There is a widening of the main beam but the sidelobes are reduced to <-30dBc.

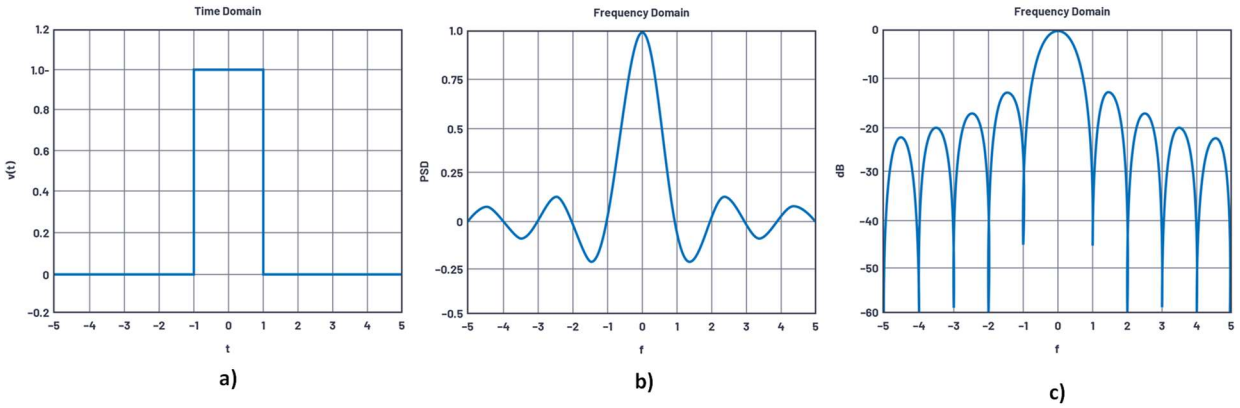


Figure 2-4 Rectangular pulse a) time domain b) frequency domain in magnitude and c) frequency domain in dB. Reproduced from [10].

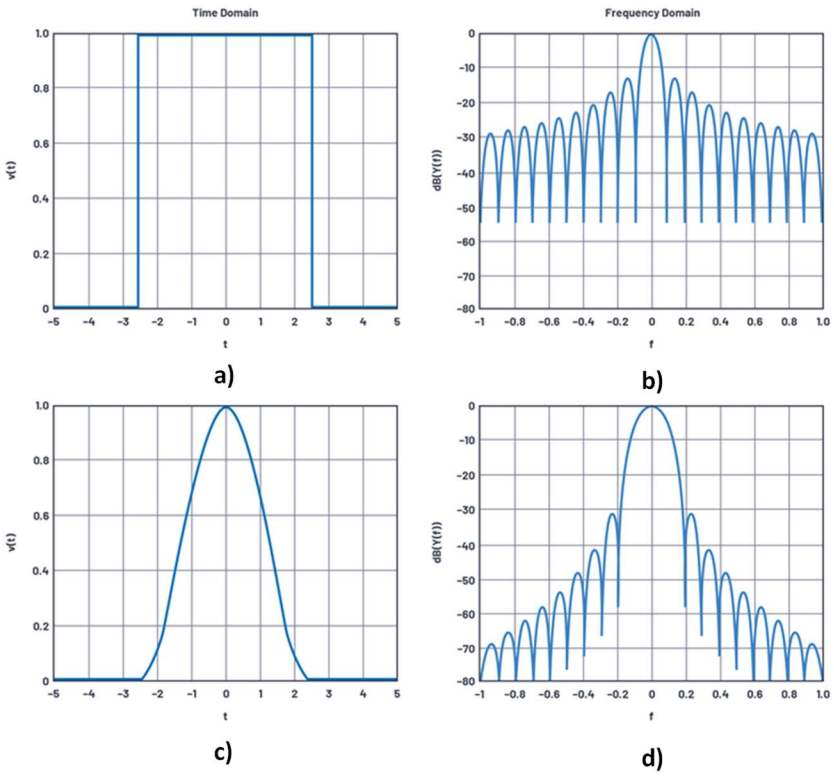


Figure 2-5 Rectangular pulse a) time domain and b) frequency domain. Hanning window c) time domain and d) frequency domain. Reproduced from [10].

### 2.2. Antenna Feeds and Beamformers

Antenna feeds are the feeding system for a group of antennas. These networks can be active or passive. Active feed networks use many transmit/receive modules, sometimes for each element. This reduces the amount of power the phase shifters have to process. Passive feed networks can be divided into two categories, space feeding and constraint feeding. Space feeding involves a feed horn antenna that illuminates elements placed in precise locations. This is rarely used because of the difficultly to implement and the large space required. Constraint feeding is the most common type of antenna feeding. These types of feed networks can be easily implemented with planar technology and can be designed independent of antenna geometry. They can be in a serial or parallel configuration. A serial configuration is shown in Figure 2-6. The elements that are further

away from the feed point have the largest phase delay. This effect can be useful for frequency scanning applications but in other cases is undesirable since the phasing between elements is a function of frequency. A parallel configuration, shown in Figure 2-7, does not suffer from phase variation over frequency and is the most common antenna feeding used.

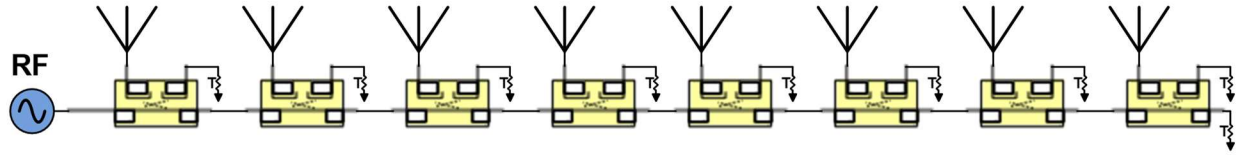


Figure 2-6 Serial antenna feed example.

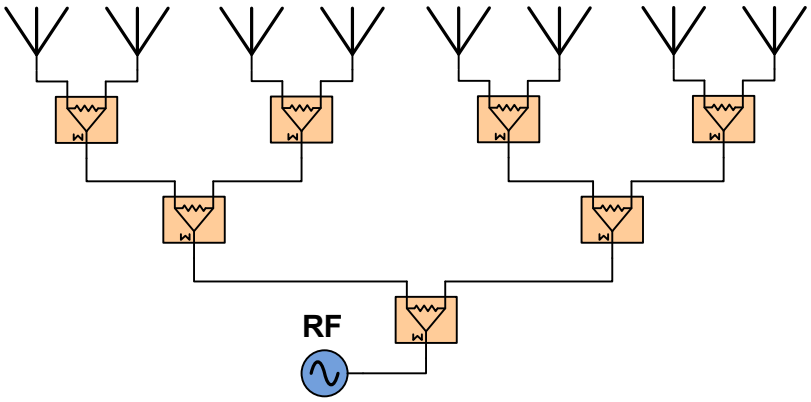


Figure 2-7 Paralell antenna feed example.

A beamformer is an antenna feed network that controls the phase and amplitude to each of the elements of an antenna array. This can be done with fixed beamformers, such as a Butler matrix [11] or a Rotman lens [12], or an electronically scanned array, usually called a phased array. With the case of the phased array, controllable phase and amplitude adjusters to each element are used to steer the beam in a particular direction. In the case of the Butler matrix or the Rotman lens the

phase difference between the output ports is different depending on the input port used, this will steer the beam in a fixed direction.

### 2.3. Leaky Wave Antennas

A leaky-wave antenna (LWA) is a traveling wave antenna that uses a guiding structure with a leaky boundary that radiates along the structure [13]. A simple diagram of a leaky wave antenna is shown in Figure 2-8. In the guided structure the wave travels in the z direction with the propagation constant $\beta(\omega)$. In the section with the leaky surface, to support wave propagation, the dispersion relation $k_x$ must be real, which occurs when $\beta(\omega)$ is less than the free space wave number $k_0$, as seen in Eq. (2.3). The region where this is the case is also illustrated in the dispersion diagram in Figure 2-9. This region is called the fast wave region and there will be a radiated beam from the leaky surface at scan angle $\theta_0$. This angle is defined by Eq. (2.4) which is frequency dependent. This allows beam steering in one dimension using only one antenna just by changing the input frequency.

$$k_x = \sqrt{k_0^2 - \beta(\omega)^2} \tag{2.3}$$

$$\theta(\omega) = \sin^{-1}\left[\frac{\beta(\omega)}{k_0}\right] \tag{2.4}$$

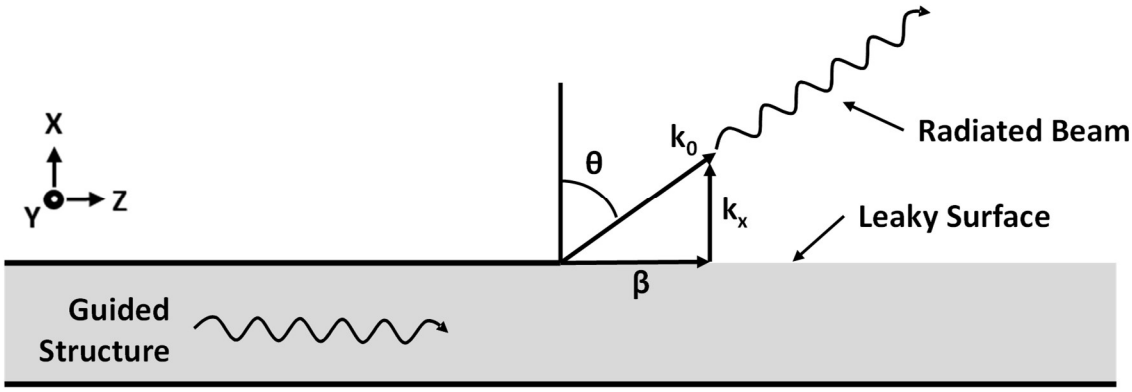


Figure 2-8 Side view of a typical leaky-wave antenna.

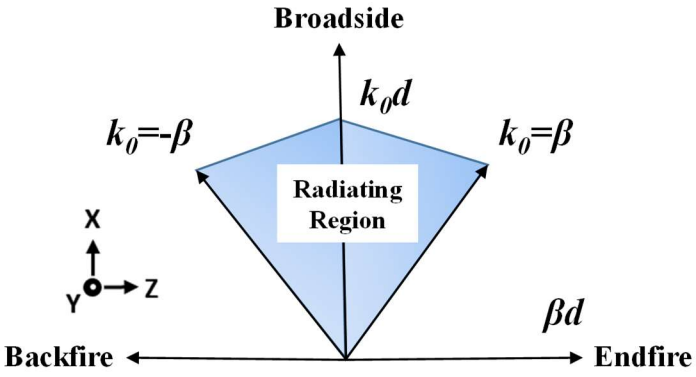


Figure 2-9 Leaky wave antenna dispersion diagram.

### 2.4. Composite Right/Left-Handed Transmission Lines (CRLH-TLs)

The concept of left handed materials, "substances with simultaneously negative $\varepsilon$ and $\mu$", was first speculated in 1967 by Viktor Veselago [14]. No known natural material has a $\mu < 0$ and is homogeneous.

In the last 20 years significant research has been conducted into the fabrication of components that have this behavior, starting with [15] that presents a planar CRLH-TL. The equivalent circuit schematic of a CRLH-TL unit cell and the dispersion diagram are shown in Figure 2-10. There are two separate regions in the dispersion diagram: the left handed region, where the left-handed

components ($C_L$ and $L_L$) are dominant and the right-handed region, where the right-handed components ($C_R$ and $L_R$) are dominant. A purely left hand (PLH) response and a purely right hand (PRH) response are also shown for reference in these regions. These regions are generally separate but the components can be tuned in a way so that the end of the left-handed region ends where the right-handed region begins. In this configuration there is a smooth transition between the regions and the CRLH-TL is said to be balanced.

A typical microstrip implementation of a CRLH-TL is shown in Figure 2-11. It uses a periodic structure with unit cells whose length, $p$, is significantly less than the operating wavelength ($p << \lambda$) so that at its operating frequency, the structure appears homogeneous. The right-handed components ($C_R$ and $L_R$) are inherent in the microstrip structure and the left-handed components are implemented with an interdigital capacitor for $C_L$ and a shorted stub for $L_L$.

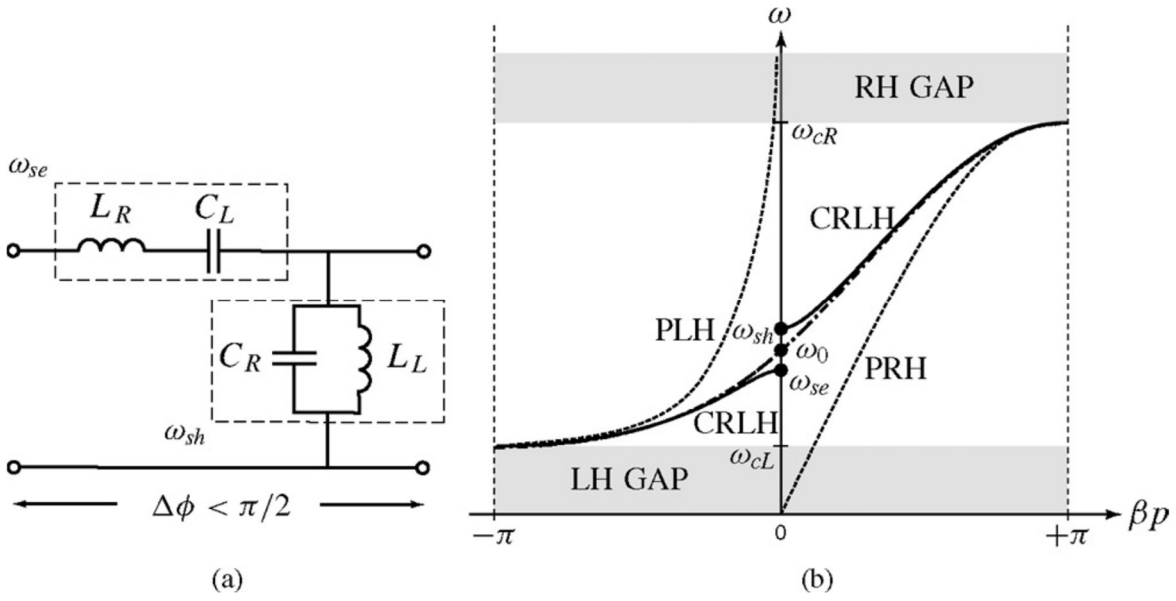


Figure 2-10 CRLH-TL a) schematatic and b) dispersion diagram. Reproduced from [16].

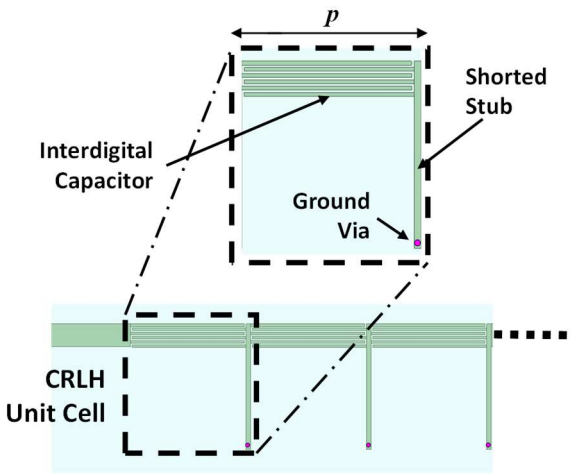


Figure 2-11 Typical CRLH-TL planar implementation.

# Chapter 3. Broadband Power Dividers for Antenna Array Feeds

## 3.1. Introduction

An array with a bandwidth of 30% will properly function using a single element spacing. An antenna feed that will cover the bandwidth is all that is required. Power dividers/combiners are one of the main components in such antenna feed networks. The Wilkinson power divider/combiner [17] is the most commonly used component for the above-mentioned function due to its simplicity and its ability to isolate the output ports using a balanced resistor. The main drawback of this component, however, is its power handling capability. Since the resistor is positioned between transmission lines, the heat generated cannot be effectively dissipated from the circuit to the ground plane. Thus, the potential for high power operation becomes severely limited by the ungrounded resistor. While there is no limit on the power handling of the Wilkinson as such, the ability to heat sink the resistor and the fact that a larger resistor needed for higher power becomes difficult to design around for RF performance, make it not very conducive for high power designs.

The Gysel divider/combiner [18] provides a solution to improve the power-handling capability of the Wilkinson by replacing the balanced resistor with a quarter-wavelength line at each output port, terminated by a resistor. Additional quarter-wavelength lines extend from each resistor to connect at a single point. Furthermore, these shunt isolation resistors can be pulled any desired distance away from the rest of the circuit by inserting a transmission line of the same impedance directly before the resistor. Such freedom in design allows for many different heat sinking schemes to be implemented, which is particularly useful for applications requiring higher power handling. This also provides some flexibility with implementing the layout of the component. Since the resistor is tied to ground instead of being in the RF path, this resistor can be placed on other layers

in a multi-layer design and also matching network can be included without impacting the performance of the component. Despite the aforementioned advantages, the main drawback of the Gysel power divider/combiner is its relatively narrower bandwidth compared to the Wilkinson power divider/combiner.

The Knochel-Mayer divider/combiner [4] provides similar advantages as the Gysel in terms of power handling capability, but can ideally be designed with -25 dB bandwidth that exceeds even that of the Wilkinson. To achieve this performance, additional half-wavelength stubs separated by quarter-wavelength lines are added to the input and output networks. In essence, the Knochel-Mayer is a multi-section implementation of the Gysel. Thus, this bandwidth-enhanced Knochel-Mayer structure is also designed with the resistors isolated and tied to ground, which maintains the power handling capability and layout flexibility of the Gysel power divider.

Sample layouts of these types of power dividers are shown in Figure 3-1 for comparison. The Knochel-Mayer is larger than the Wilkinson and the Gysel but that is the trade-off for the additional bandwidth. The typical performance of these power dividers, as shown by the common port return loss, is seen in Figure 3-2 to illustrate the bandwidth capabilities of each type. The components used in this comparison are ideal 2-way power dividers/combiners presented on a normalized frequency axis (frequency $f$ divided by center operating frequency $f_c$).

A broadband antenna feed with 30% bandwidth can be designed using Knochel-Mayer power dividers. An antenna array with elements spaced at a fixed width of $\lambda_0/2$ (where $\lambda_0$ is the wavelength in free space) at $f_c$ would be cable of ±30° of beam steering for an operating bandwidth of 30%. Figure 3-3 shows the array pattern for the case of operating an array ±15% away from its center operating frequency. Within these operating conditions, the performance of the antenna array does not suffer any significant degradation of the main beam and it has side lobes better than

-10dB and is grating lobe free.

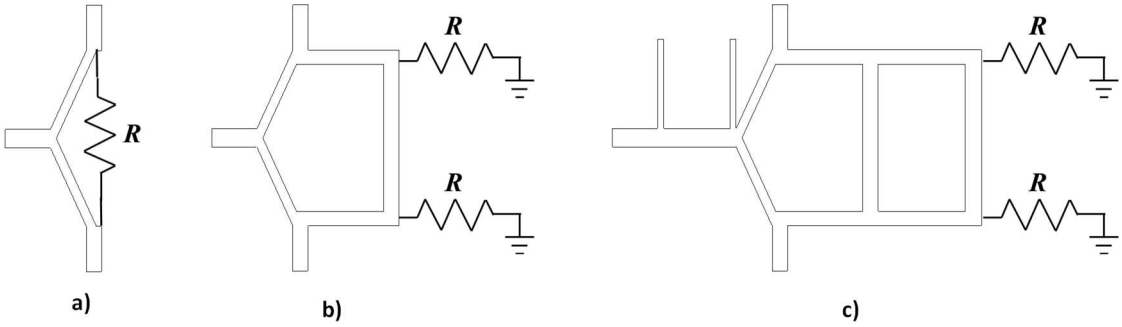


Figure 3-1 Layout comparison of 2-way a) Wilkinson, b) Gysel and c) Knochel-Mayer power dividers.

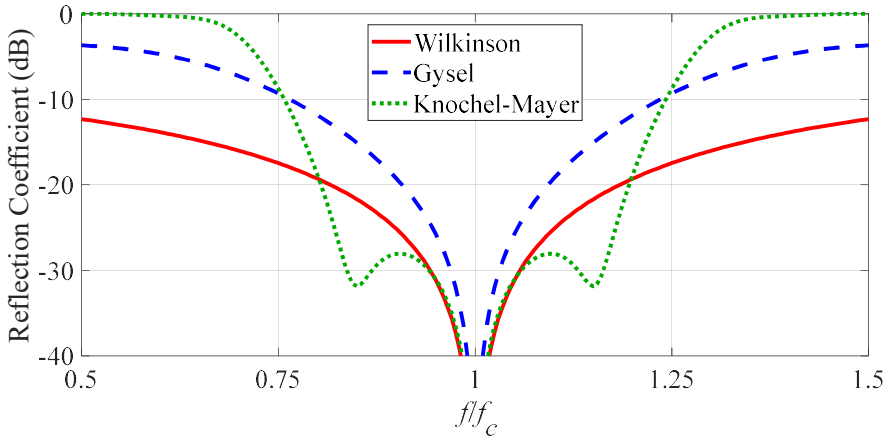


Figure 3-2 Common port return loss comparison of Wilkinson, Gysel and Knochel-Mayer power dividers.

While the Wilkinson and the Gysel have been described in detail for multiple ($N \geq 2$) outputs [19]-[29] and unequal split case [30]-[37] in previous literature, the Knochel-Mayer was introduced specifically as a 2-way power equal split divider/combiner in the original paper [4] and has not been expanded on previously. In this chapter the structure of this divider is analyzed and the concept is expanded to N-way, unequal split and ultra-wide band cases making it more versatile for antenna feed networks.

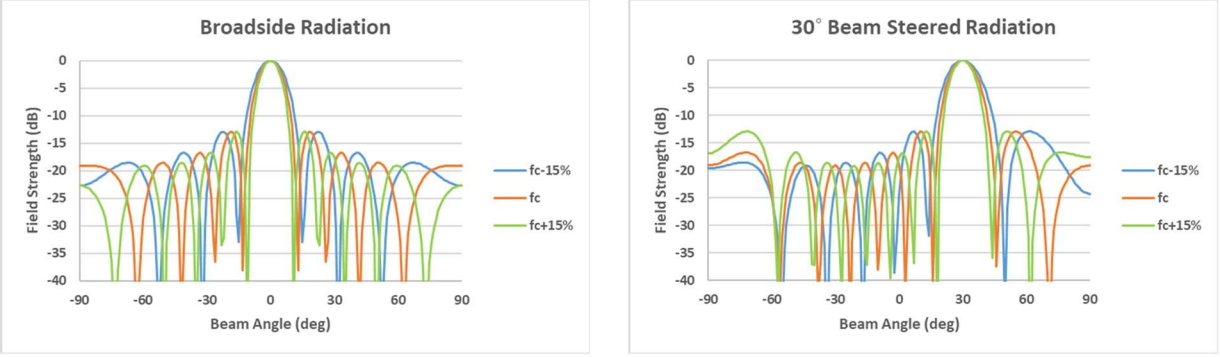


(a) (b)

Figure 3-3 Nine element array example.

The structure of the original Knochel-Mayer power divider is analyzed and the functions of the different sections are defined. The concept is then expanded for the *N*-way case, unequal split and wider bandwidth cases. All of these different cases maintain the wideband performance as the original as well as the power handling potential/layout flexibility with the added capability. The following sections detail the analysis and results of the simulations and measurements of the prototypes of these different cases.

### 3.2. Knochel-Mayer Circuit Analysis

The layout of the original equal split 2 way case is shown in Figure 3-4 with a line of symmetry shown through the common port. The parallel open stubs ($Z_6$ and $Z_8$) shown, were single open stubs in the original. They are shown as two lines in a parallel configuration here in order to illustrate the symmetry. The simplified schematic is shown in Figure 3-5, where three distinct sections can be observed. The transformer section, $Z_1$, transforms the impedance between the input and output ports. The isolation network controls the output return loss and the isolation between

output ports. And finally, the input network provides the match for the input return loss.

This symmetry allows for the circuit to be exploited for even and odd mode analysis. The equivalent even and odd mode schematics are shown in Figure 3-6.

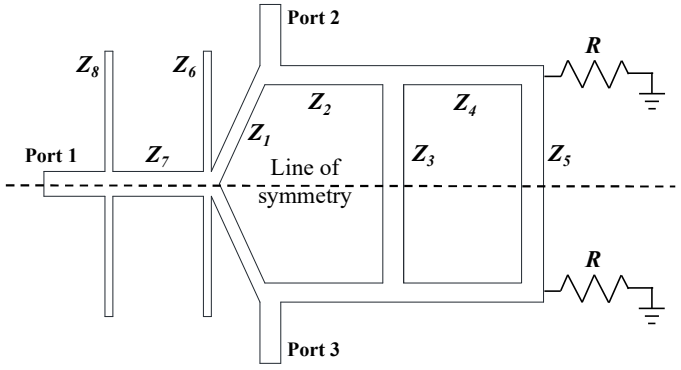


Figure 3-4 Knochel-Mayer power divider layout.

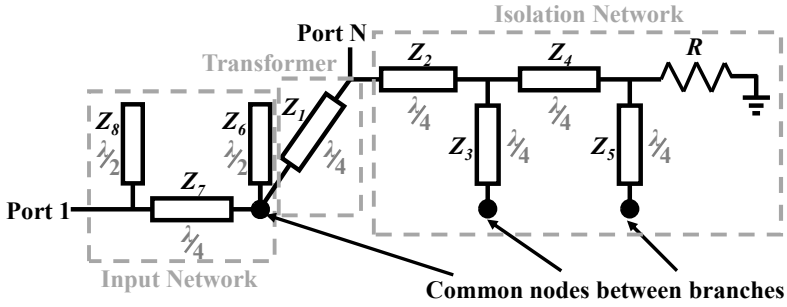


Figure 3-5 Knochel-Mayer circuit schematic of a single branch.

### 3.2.1. Even Mode

The even mode circuit has quarter-wavelength lines of impedance $Z_3$ and $Z_5$ terminating in opens along the plane of symmetry. The input network, with lines of impedance $Z_6$, $Z_7$, and $Z_8$, remains connected, but these are now multiplied by 2 because of the symmetry. At the center frequency, the half-wavelength open stubs at the input transform to opens at $Z_7$ and have no influence on the circuit. The open-circuited quarter-wavelength stubs in the isolation network transform to shorts at either side of $Z_4$, which are seen as opens at the output port due to the quarter-

wavelength series lines $Z_2$ and $Z_4$. This leaves only the transformer section, $Z_1$ which connects the input and output ports and transforms the impedance.

### 3.2.2. Odd Mode

The odd mode circuit has lines of impedance $Z_1$, $Z_3$, and $Z_5$ terminating in shorts at a length of $\lambda/4$ along the plane of symmetry. At the center frequency, these shorted stubs transform into open-circuits and thus have no influence on the circuit and the short at the first common node removes the input network from the circuit. Only $Z_2$, $Z_4$, and $R$, remain in the odd mode circuit and if they are equal to the system impedance, the odd mode port is perfectly terminated.

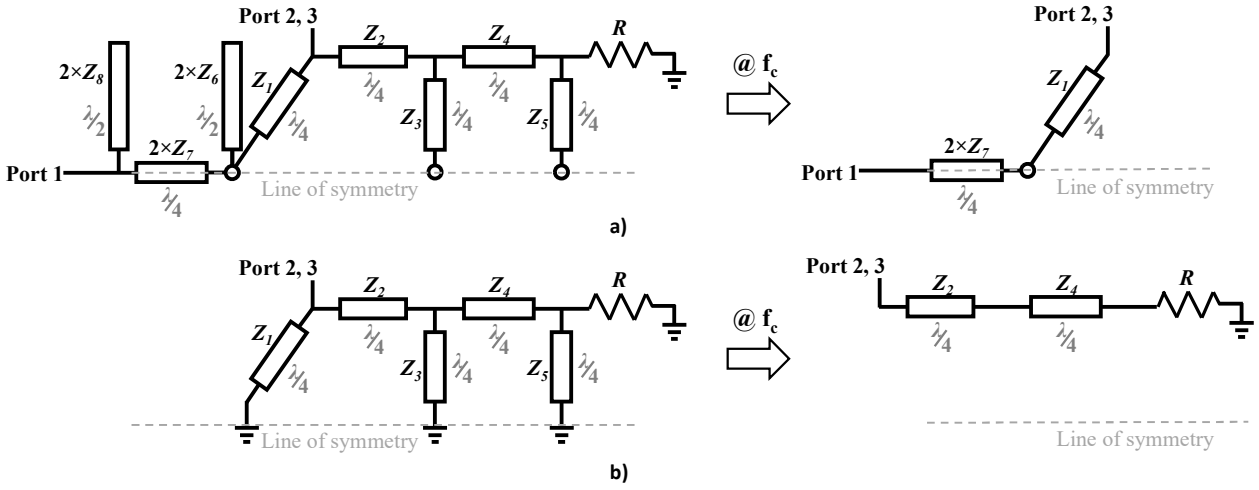


Figure 3-6 Knochel-Mayer equivalent circuits of a) even mode b) odd mode.

### 3.2.3. Design Procedure

At the center frequency, the even and odd mode schematics of the Knochel-Mayer power divider reduce to a very similar structure to the Wilkinson. In the even mode circuit at the center frequency, the shunt lines $Z_6$ and $Z_8$ as well as the isolation circuit are unseen in this circuit. This is the same even mode circuit as the Wilkinson with the addition of transmission line $Z_7$, which is the same impedance as the input port. In the odd mode circuit at the center frequency the shunt lines $Z_1$, $Z_3$ and $Z_5$ are unseen in this circuit leaving only series transmission lines $Z_2$ and $Z_4$

connecting to the terminated resistor. If these transmission lines and terminated resistor are set to the system impedance $Z_0$, the odd mode circuit is the same as the Wilkinson with the addition of the series transmission lines. All of the series transmission lines and the terminating resistor are defined in Eq. (3.1),

$$Z_2 = Z_4 = Z_7 = R = Z_0. \tag{3.1}$$

Since the even and odd mode circuits are the same (with the exception of additional transmission line of the same impedance), $Z_1$ will be equal to $Z_0\sqrt{2}$ for the 2-way case. The original paper from Wilkinson [17] also solved the divider for the $N$-way case, which can be used for the $N$-way Knochel-Mayer as well and thus,

$$Z_1 = Z_0\sqrt{N}, \tag{3.2}$$

with $N$ being the number of outputs. Using this simplification, the design will always be perfectly tuned to the center frequency. There is a slight degradation in bandwidth by fixing these impedances to $Z_0$ because it makes the complex impedance cross the Smith chart at the center instead of these impedance loops being centered on the center of the Smith chart. This sacrifices some bandwidth but this degradation is minimal and it simplifies the design significantly, only leaving $Z_3$, $Z_5$, $Z_6$ and $Z_8$ as unknowns. From the even and odd mode analysis, it is seen that the input port is completely decoupled from the odd mode circuit at the center frequency and through simulation it is observed that $Z_3$ and $Z_5$ can be used to control the output match without significantly affecting the input match. Then with $Z_3$ and $Z_5$ set, $Z_6$ and $Z_8$ can then be used to tune the input match. The optimal values can be found by manually tuning in a circuit simulator by first adjusting $Z_3$ and $Z_5$ to achieve the desired performance and bandwidth of the output return loss and

then adjusting $Z_6$ and $Z_8$ to achieve the final desired performance and bandwidth of input and output return loss and the isolation. Alternately, any type of computer optimization could be used to find the impedances of all four impedances at once. This procedure is the basis for the design of the different cases: N-way, unequal split and wider band.

### 3.2.4. High Power Considerations

The power handling of a planar device can be evaluated in three distinct areas: the connectors, the transmission lines, and any discrete components. The connectors usually have inherent high power handling due to the relatively high metal mass and low loss. A typical SMA connector can handle around 150 W at 20GHz. And transmission lines similarly have relatively higher power handling due to the low loss. A 12.5 mil wide line on ½ oz. copper can handling up to 50 W and this power handling can be increased by increasing the copper weight. The limiting factor in power handling of a power divider is the resistors. These resistors can dissipate half of the input power or more. A surface mount resistor in an 0402 package can typically handle around 1/8 W. Larger package sizes can handle more power but larger sizes are more difficult to implement at high frequencies in the Wilkinson configuration where the resistor connects to the output ports. Resistors specifically designed for higher power (> 1 W) usually have one terminal with a larger pad meant for heat sinking which will not work in a Wilkinson design.

The layout flexibility of the Gysel or the Knochel-Mayer allows for these higher power resistors to be implemented in the component. Many different heat sinking schemes to improve the power handling of the component can be implemented because these structures remove the resistors from the RF path. The resistors can be connected to a transmission line of the same value and any length. This moves the resistor away from the transmission lines of the component which can create space for necessary heat sinking. Larger resistors and large ground planes can be implemented without

impacting RF performance and this is why the structures are more suited to high power applications.

## 3.3. N-way Knochel-Mayer Power Divider

Power dividers that can have an arbitrary number of outputs provide ease of layout implementation. The footprint for an *N*-way power divider will be smaller than cascaded 2-way power dividers to achieve the same number of outputs. The Knochel-Mayer design can be expanded to an N-way divider while maintaining its capability for high power handling. The equations generated in the analysis of the 2-way are scalable for the N-way case and the same design procedure can be used. The concept is demonstrated with the implementation of a 4-way prototype operating at S-band.

### 3.3.1. Circuit Analysis

The Knochel-Mayer divider/combiner introduces an additional common node between output branches to the Gysel in order to extend the bandwidth. There are two in the isolation network plus the one at the input gives a total of three common nodes of the circuit that are connected together. Although the schematic is simple, a planar implementation for an $N>2$ requires crossovers for the common nodes between branches.

#### 3.3.1.1. Circuit Stack Up

The stack-up is realized by using a stripline sandwiched between two microstrips, which gives a total of 5 metal layers (3 signal layers and 2 ground layers). The 3 signal layers are enough to avoid any crossovers so that it can be implemented in a planar design and will not impact the potential for power handling because the resistors will be terminated to a ground plane that can be

optimize for heat dissipation. The dielectric cores of the stack up are chosen (based on the dielectric constant and thickness) to keep the transmission line widths from getting too wide or too narrow. Lines that are too narrow are difficult to manufacture and lines that are too wide can cause problems with higher order modes. Figure 3-7 shows the details of the stack-up. The input and outputs (including $Z_1$, $Z_6$, $Z_7$ and $Z_8$) of the circuit are located on the stripline signal layer, Layer 3. Layer 1 is the top microstrip signal layer, which contains the isolation resistors and their adjoining lines ($Z_4$ and $Z_5$). Layer 5 is the bottom microstrip signal layer and includes the remaining pair of lines ($Z_2$ and $Z_3$) between the output and the line ($Z_4$) leading to the resistor. Layer 2 and Layer 4 serve as the ground planes, which are shared between the stripline and the microstrips. There will also need to be transitions to connect the different layers called vias. There is a L1-L2 via that grounds the resistors, a L2-L4 via to provide grounding in the stripline of the connector launch, a L1-L5 via to connect the microstrip signal traces and a L3-L5 to connect the stripling to the L5 microstrip.

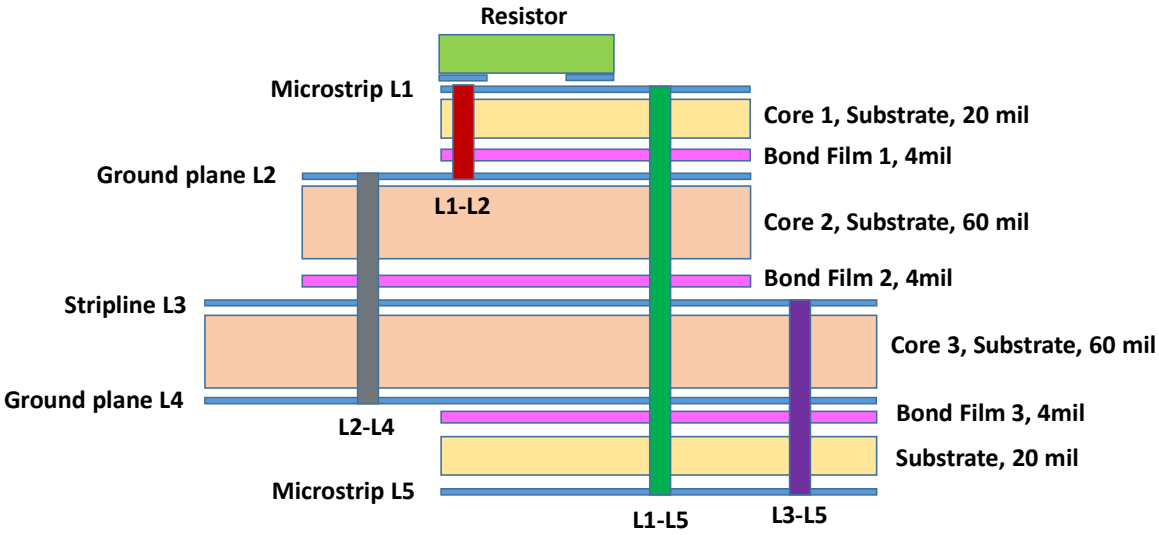


Figure 3-7 4-way Knochel-Mayer circuit stack-up.

### 3.3.2. Design Procedure

An N-way power divider can be designed using the same procedure as the 2-way case. The transformer of impedance $Z_1$ between the input and output ports is defined by Eq. (3.1), which is 100 Ω for a 4-way power divider and the series transmission lines are defined by Eq. (3.2). This leaves the same unknown impedances, $Z_3$, $Z_5$, $Z_6$ and $Z_8$, as in the 2-way case and the procedure in Section 3.2.3 is used. The final values of the design are; $Z_1$ = 100 Ω, $Z_2$ = 50 Ω, $Z_3$ = 35 Ω, $Z_4$ = 50 Ω, $Z_5$ = 50 Ω, $Z_6$ = 84.6 Ω, $Z_7$ = 50 Ω, $Z_8$ = 100 Ω, $R$ = 50 Ω.

### 3.3.3. EM Modeling and Simulation

A 3D electromagnetic model of the proposed circuit is built in ANSYS HFSS (shown in Figure 3-8). The circuit stack-up defined previously uses Rogers RO3003 ($\varepsilon_r$ = 3.00, tan δ = 0.0013) with thickness 0.508 mm (0.02″) or 1.524 mm (0.06″), as indicated, as the main dielectric layers and a 0.101 mm (0.004″) thin layer of Rogers RO4450B ($\varepsilon_r$ = 3.54, tan δ = 0.004) as the bond film. The materials were chosen for the thickness and the $\varepsilon_r$ value in order to keep the transmission lines from becoming too narrow to produce or too wide which could support higher order modes. The line widths and lengths are calculated using the impedances obtained from the circuit model.

The model is simulated from 2–4 GHz and the results are shown in Figure 3-9. The operational band of the component is from 2.25–3.25 GHz which gives a 36% BW. The return loss for all ports is -10 dB or better in the entire band. All combinations of port to port isolation are shown to be -15 dB or better for the entire band as well. The amplitude balance (or variation in amplitude across the output ports) stays within a window of ±2 dB. The phase balance (or variation in phase across the output ports) stays within a window of ±5°.

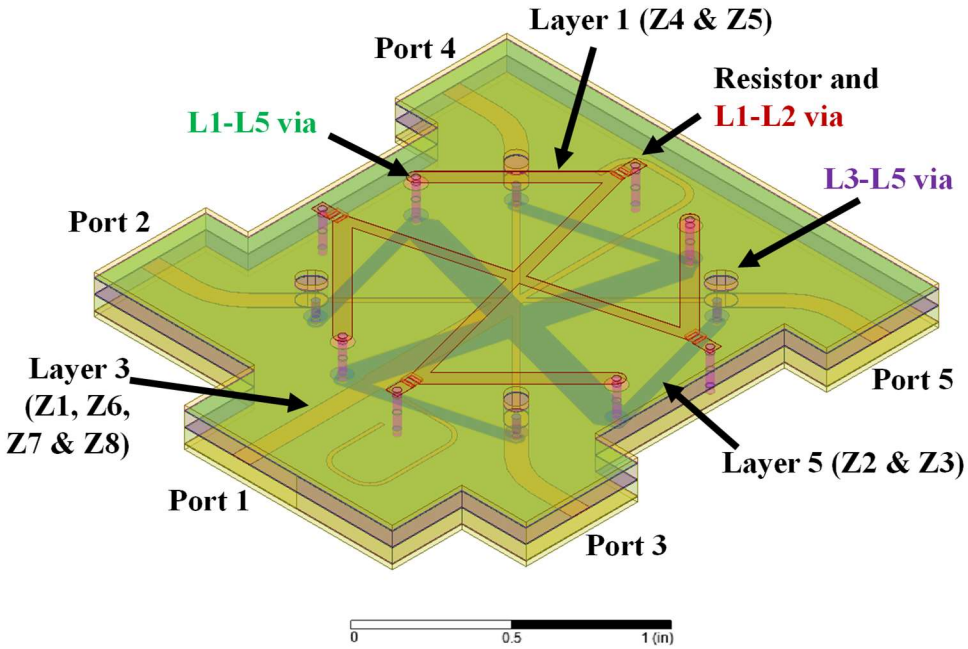


Figure 3-8 3D EM model of the 4-way Knochel-Mayer power divider.

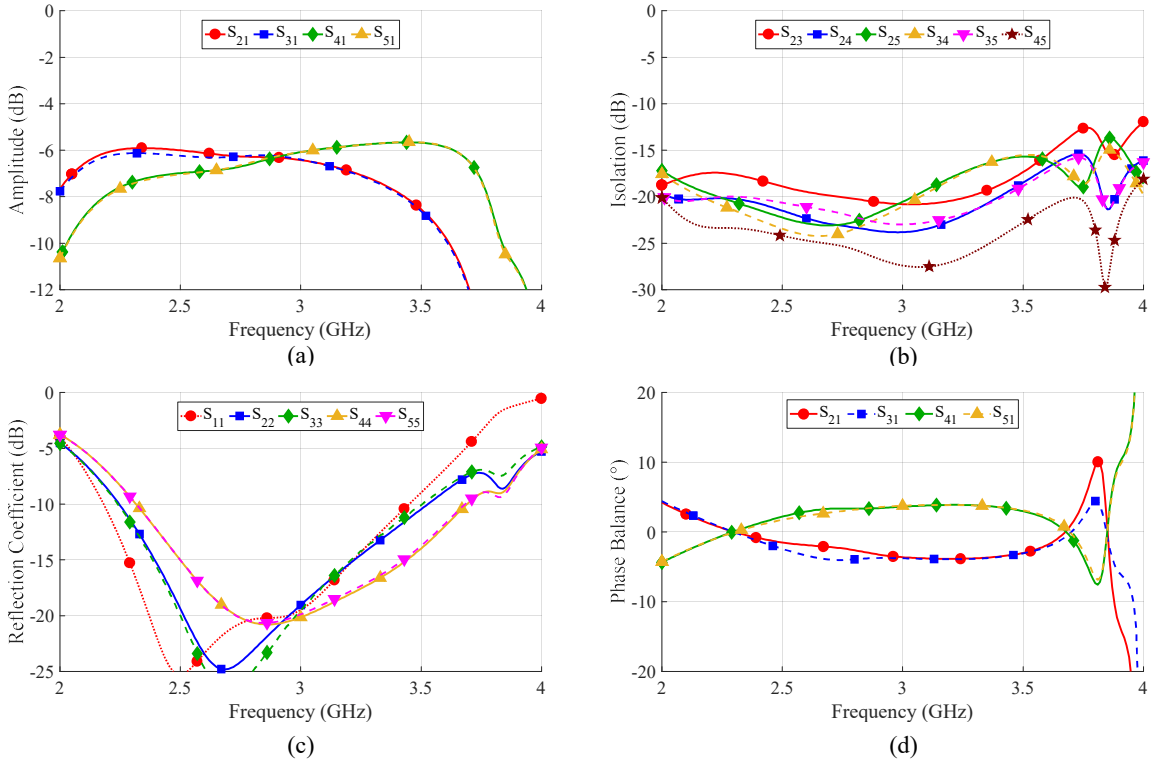


Figure 3-9 Simulated results (a) return loss (b) isolation (c) amplitude (d) phase.

### 3.3.4. Fabrication and Measured Results

The prototype circuit is fabricated by first milling the individual cores and bond films. The milled cores are shown in Figure 3-10. The cores and bond films are then stacked together using pins in the alignment holes, shown in Figure 3-11. The bond film needs pressure and high temperature to cure. The temperature and pressure profile recommended by the manufacturer is shown in Figure 3-12. The pressure profile required is a constant 400 psi. This is achieved using locking pliers clamping the stacked cores and bond films between two metal plates. These locking pliers can typically provide around 1000 lbs. of pressure. The circuit is 3.5" x 2.5" (10.5 $in^2$) and four locking pliers are used which gives 380 psi, which is within 5% of the recommended value. The required temperature has a ramp up and ramp down profile. This is achieved in an oven with a manually controllable temperature. The clamped fixture in the oven is shown in Figure 3-13.

The bonded circuit is then drilled through for the interconnecting vias. The vias are created with wires fed through the holes and soldered on the applicable layers. Finally, the resistors are soldered on the top microstrip layer and the connectors are soldered to the stripline layer through cutbacks in the layers above. The assembled prototype is shown in Figure 3-14.

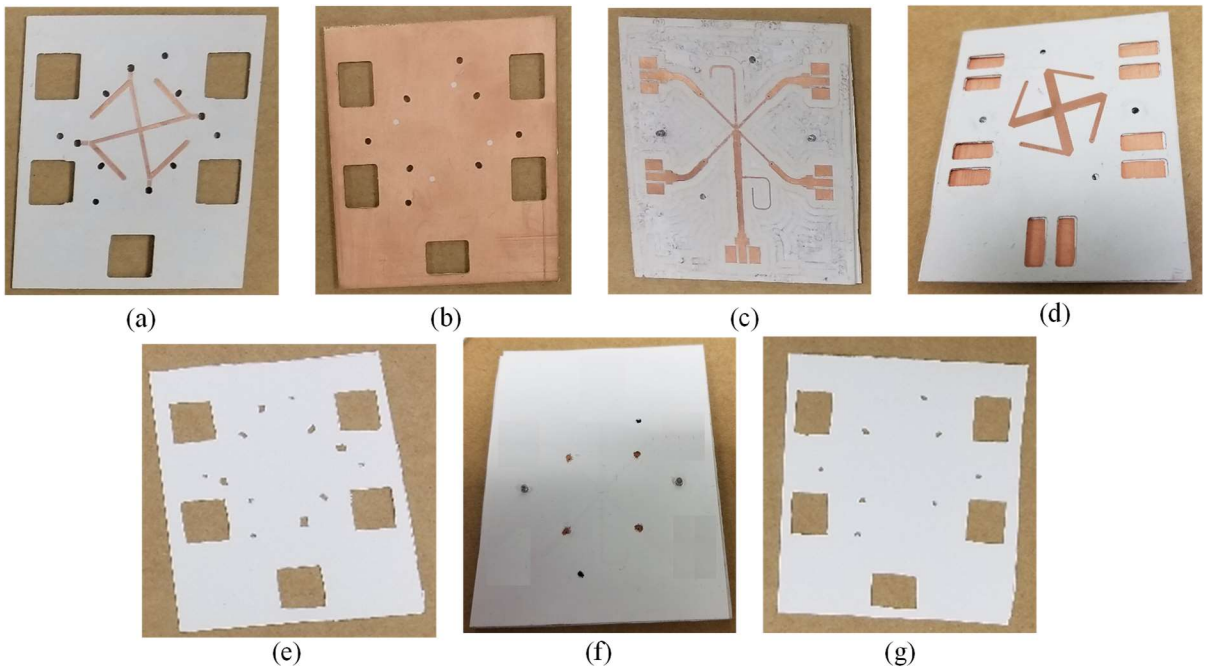


Figure 3-10 4-way Knochel-Mayer prototype milled cores and bond films: a) core 1, b) core 2, c) core 3, d) core 4, e) bond film 1, f) bond film 2 and g) bond film 3.

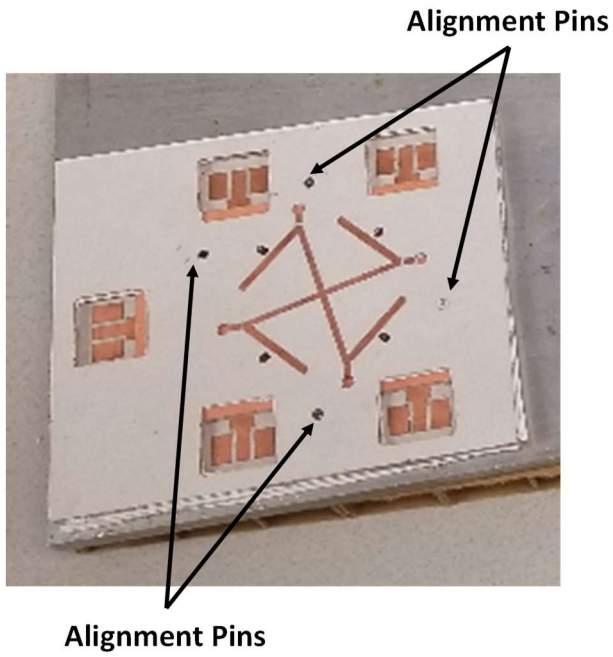


Figure 3-11 4-way Knochel-Mayer stacked cores and bond films.

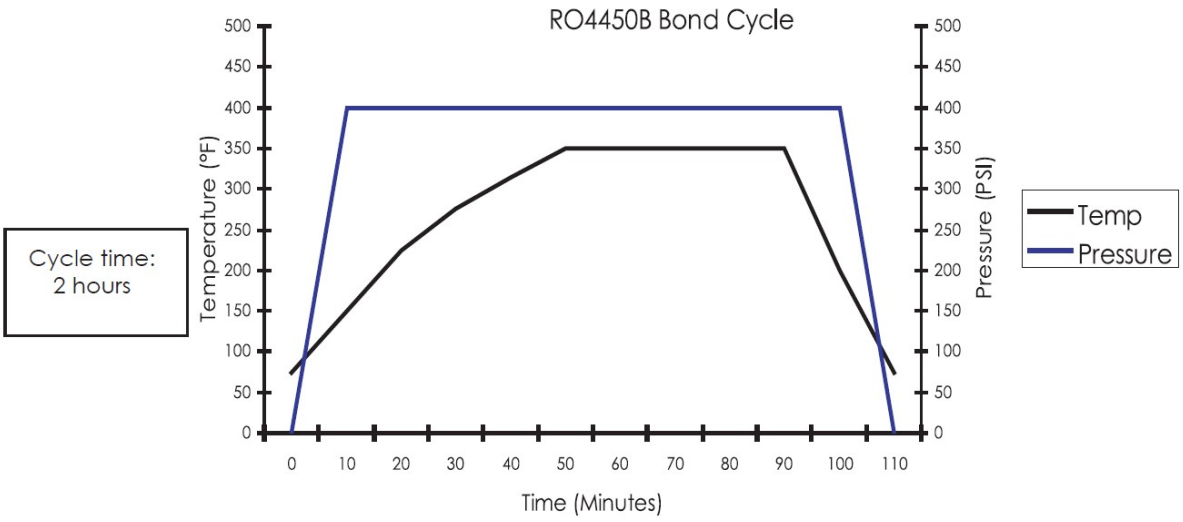


Figure 3-12 Temperature and pressure profile for RO4450. Reproduced from [38].

Figure 3-13 Clamped circuit and bonding oven.

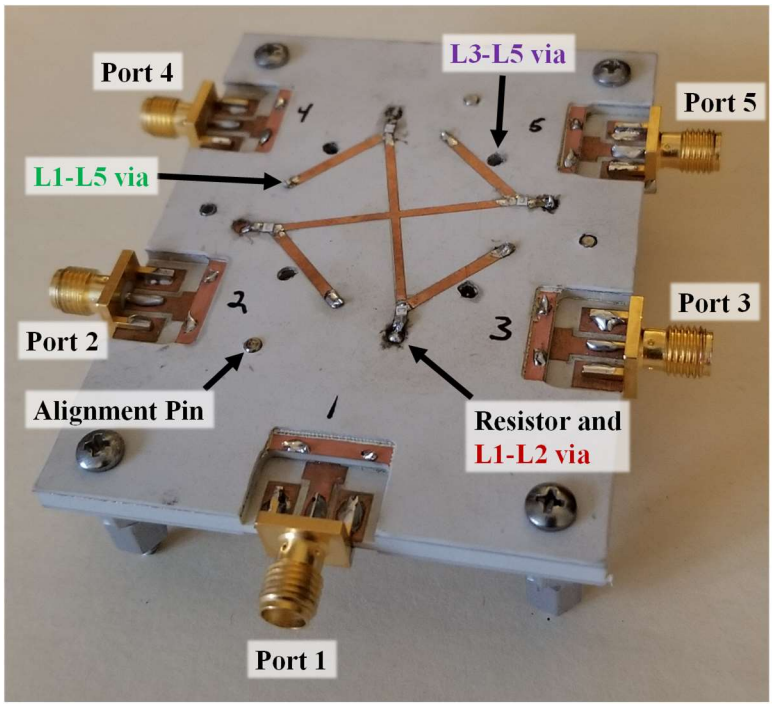


Figure 3-14 Assemble 4-way Knochel-Mayer prototype.

The measured results of the prototype are shown in Figure 3-15. The same parameters that are shown for the simulation are shown in these plots for the measured data. The measured results show good agreement with the simulated results within the operating frequency band. Using a -10 dB criteria, the circuit has over 30% bandwidth. The return loss is better than -10 dB and the isolation is better than -12 dB over the entire bandwidth. The amplitude imbalance is within ±2 dB and the phase balance is within ±5° over the entire bandwidth. A single path of each type of parameter is shown in Figure 3-16 for easier comparison of measured and simulated data. The measured performance shows some deviation from the simulated results but it still follows the general response. These deviations are the results of fabrication issues with the complex assembly. Despite some deviations from the simulated results, the measurements show less than -10 dB for both return loss and isolation, less than ±2 dB of amplitude imbalance and ±5° of phase imbalance from 2.25–3.25 GHz.

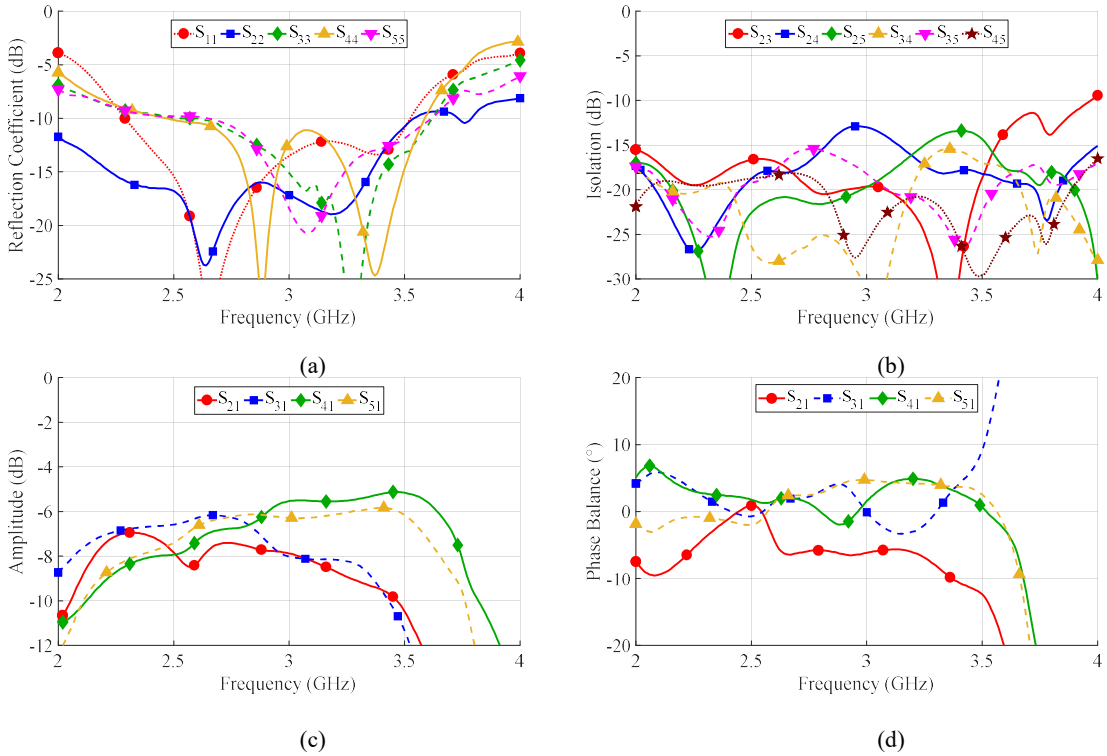


Figure 3-15 Measured results (a) return loss (b) isolation (c) amplitude (d) phase.

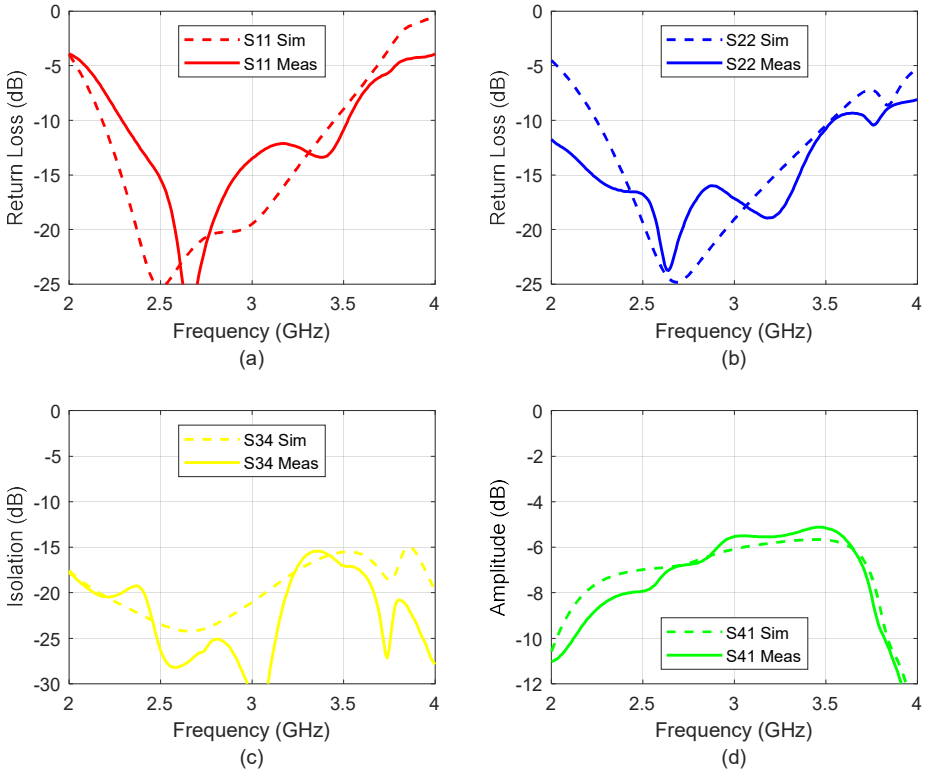


Figure 3-16 4-way Knochel-Mayer single path measured vs simulated.

The phase balance from simulated and measured data is shown together in Figure 3-17. The phase balance is calculated by subtracting the phase response of each path from the average phase response of all paths. The data from the linear transmission line model (dashed black trace) shows a perfect phase balance. The data from the HFSS model (dashed colored traces) shows two distinct phase balances. This is due to the layout implementation at the junction of the transformer sections of each branch and the vias between the layers not being tuned to the same impedance as the lines. The vias could be tuned with standard PCB manufacturing processes, such as arbitrary pad dimensions on each layer for tuning not available for this prototype. The data from the measured results (solid colored traces) shows the same two distinct phase balances. These match the HFSS results for the $S_{51}$ path closely and somewhat closely for the $S_{21}$ path. These deviations from the HFSS results are due to the complex fabrication, specifically the implementation of the vias. The L3-L5 via in the $S_{21}$ path was particularly challenging which explains the difference between the simulated and measured phase balance in this path.

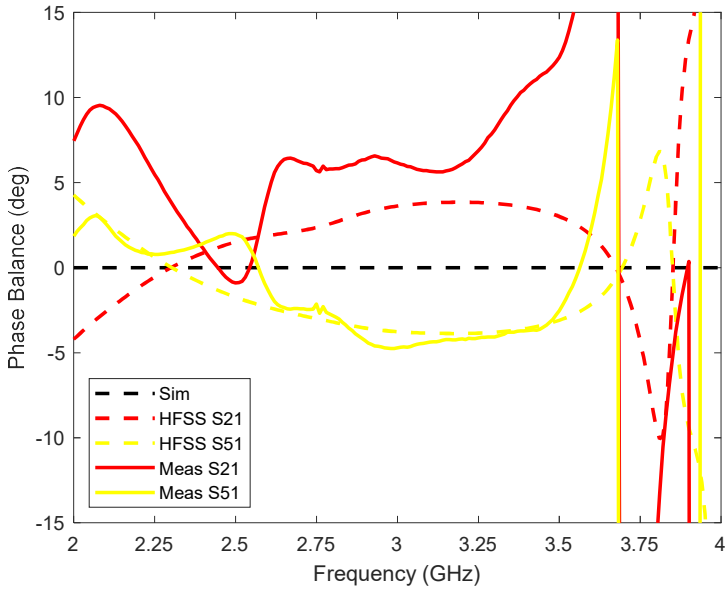


Figure 3-17 4-way Knochel-Mayer phase measured vs simulated.

### 3.3.5. Conclusion

A design procedure for an *N*-way Knochel-Mayer power divider has been shown and a 4-way Knochel-Mayer prototype has been built and tested. The prototype construction is a multilayer board with 5 total conductor layers. The layers are bonded together with a specific process defined by the bond film manufacturer and special consideration was taken to guarantee the registration between the layers. The connections between layers are achieved by soldering wires directly on the layers to be connected. There are cavities in the stack up that expose the necessary layers for each via type in the proper location. The prototype was measured and the results show reasonable agreement with the simulated data. The measured data has some deviation from the simulated results, through it still follows the general response. These deviations are due to the imperfections in the assembly due to the prototype being assembled manually. These imperfections could be eliminated with standard electrical board manufacturing processes, which will make the measured data agree more closely with the simulated data. Even with these deviations, the return loss is less than -10 dB for both return loss and isolation, less than ±2 dB of amplitude imbalance and ±5° of phase imbalance from 2.25–3.25 GHz, which is a bandwidth of 36%.

## 3.4. Unequal Split Knochel-Mayer Power Divider

In cases where an antenna feed requires some amount of amplitude taper, such as for side lobe suppression, power dividers with an unequal power division ratio are needed. The design concept used for the *N*-way divider is further expanded for the case of an unequal split power divider. In this case, the input network remains common but each branch is now treated separately because the output ports are now impedances different from $Z_0$. This is to provide the different power in each leg resulting in an unequal split. Figure 3-18 shows the schematic for an unequal split

Knochel-Mayer with the different sections designated.

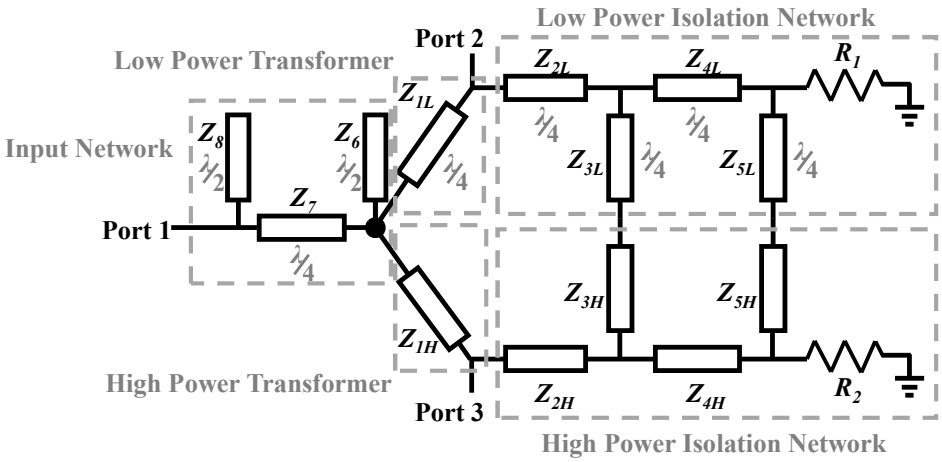


Figure 3-18 Unequal split Knochel-Mayer circuit schematic.

### 3.4.1. Circuit Analysis

Some additional considerations need to be made for the unequal split case due to the transformer sections and the isolation networks no longer being the same between branches. The equations for the unequal Wilkinson power divider (outlined in [39]) can be used to the unequal Knochel-Mayer as well. The output power ratio is defined as $K^2$ in Eq. (3.3), where $P_2$ is the power at port 2 and $P_3$ is the power at port 3 and $P_3 > P_2$. The transformers, $Z_{1H}$ and $Z_{1L}$ are defined by the same equations used for the unequal Wilkinson power divider shown in Eq. (3.4) and Eq. (3.5) [39]. These transformers will transform to the unequal port impedances in order to achieve the desired power ratio. These output port impedances are defined in Eq. (3.6) and Eq. (3.7). The series transmission lines and resistor in each branch will also equal this impedance. And the series transmission line in the input network $Z_7$ is defined in Eq. (3.8).

$$K^2 = P_3/P_2 \tag{3.3}$$

$$Z_{1H} = Z_0\sqrt{\frac{1+K^2}{K^3}} \tag{3.4}$$

$$Z_{1L} = K^2 Z_{1H} = Z_0\sqrt{K(1+K^2)} \tag{3.5}$$

$$Port\ 3 = \ Z_{2H} = Z_{4H} = R_2 = \ Z_0\text{K} \tag{3.6}$$

$$Port\ 2 = \ Z_{2L} = Z_{4L} = R_1 = \ Z_0/\text{K} \tag{3.7}$$

$$Z_7 = \ Z_0 \tag{3.8}$$

### 3.4.2. Design Procedure

With the impedances defined in the circuit analysis section, this leaves the same unknowns as for that of the *N*-way case except that the $Z_3$ and $Z_5$ lines are no longer equal between the branches, which gives a total of six unknown impedance values. However, it is seen through simulation that the ratio of these lines share the same relationship as the ratio of the output port impedances. This relationship is shown in Eq. (3.9) and Eq. (3.10).The design can once again be tuned using only four unknowns and the same design procedure can be used from the *N*-way case.

$$Z_{3H}/Z_{3L} \ = \frac{Port\ 3}{Port\ 2} = K^2 \tag{3.9}$$

$$Z_{5H}/Z_{5L} = \frac{Port\ 3}{Port\ 2} = K^2 \tag{3.10}$$

The final values of the design for a 2:1 power split ratio ($K^2 = 2$) are; $Z_{1H}$ = 52 Ω, $Z_{1L}$ = 103 Ω, $Z_{2H}$ = 35.5 Ω, $Z_{2L}$ = 70.5 Ω, $Z_{3H}$ = 30 Ω, $Z_{3L}$ = 60 Ω, $Z_{4H}$ = 35.5 Ω, $Z_{4L}$ = 70.5 Ω, $Z_{5H}$ = 35 Ω, $Z_{5L}$ = 81 Ω $Z_6$ = 75 Ω, $Z_7$ = 50 Ω, $Z_8$ = 66 Ω, $R_1$ = 35.5 Ω, $R_2$ = 70.5 Ω.

A final consideration for the unequal split case is the fact that the output ports are no longer equal to the system impedance. A matching network would be required to transform the ports back to the system impedance if necessary. Any type of matching network can be used to achieve this. A dual section quarter wave transformer is used to realize the same bandwidth of this prototype.

### 3.4.3. EM Modeling and Simulation

A 3D electromagnetic model of the proposed circuit is built in ANSYS HFSS (shown in Figure 3-19). The circuit is designed in microstrip on a core of 0.508 mm (0.02″) thick and $\varepsilon_r$ = 3.0. The line widths and lengths are calculated using the impedances obtained from the circuit model.

### 3.4.4. Fabrication and Measured Results

The proposed device is realized in microstrip technology on Isola Astra substrate ($\varepsilon_r$ = 3.0, Height = 0.508 mm). SMA connectors and surface mount resistors from KOA Speer Electronics are soldered to the board. The assembled prototype is shown in Figure 3-20.

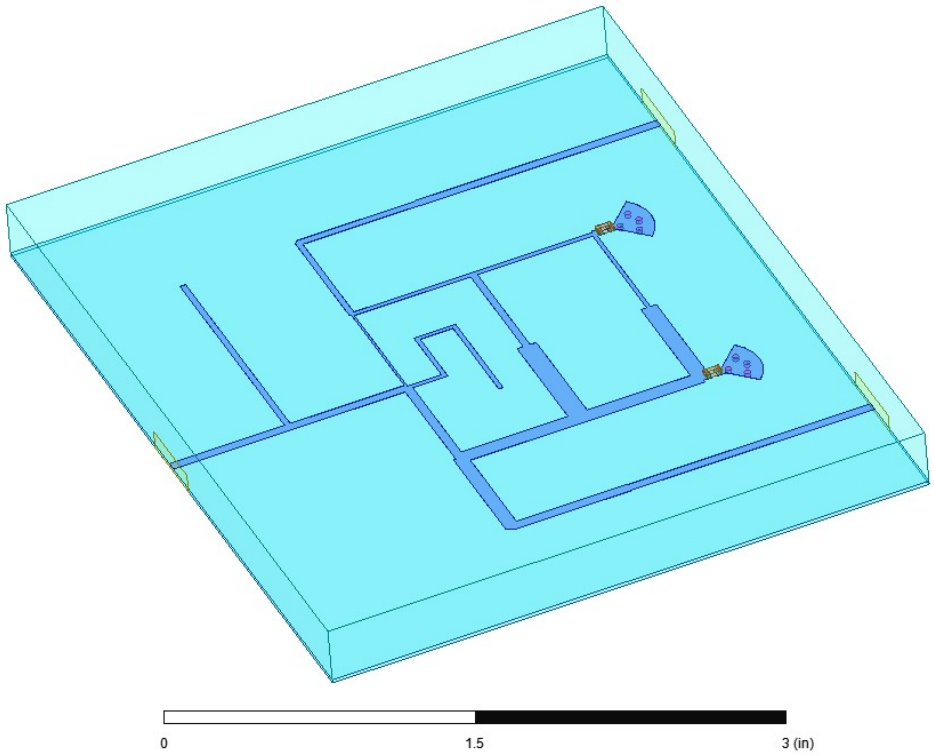


Figure 3-19 3D EM model of the unequal split Knochel-Mayer power divider.

The S-parameters of the assembled prototype are measured and the results are shown in Figure 3-21 along with the simulated results. The prototype is centered around 3 GHz and the

measurements show good agreement with the simulation. The operational band of the component is from 2.5–3.5 GHz which gives a 33% BW. The input return loss in a) is -12 dB worst case at the low end of the band but is better than -20 dB for most of it. The output return loss for both ports in b) is -15 dB or better for the entire band. The output port to port isolation in c) is -17 dB worst case at the low end of the band but is better than -20 dB for most of it. The amplitudes at the output ports in d) is within 0.5 dB of the expected value for each path. The measured data shows more loss in both paths from the simulated data. The model does not include the connectors and the input transmission lines. This indicates that the additional loss is due to these omissions. The power split ratio, despite these differences, remains close to the goal of 2:1 ($K^2 = 2$). The power split ratio from the simulated and measured data is shown in Figure 3-22. Both the simulated and the measured data shows a power split ratio of close to 2:1 from 2.5-3.5 GHz.

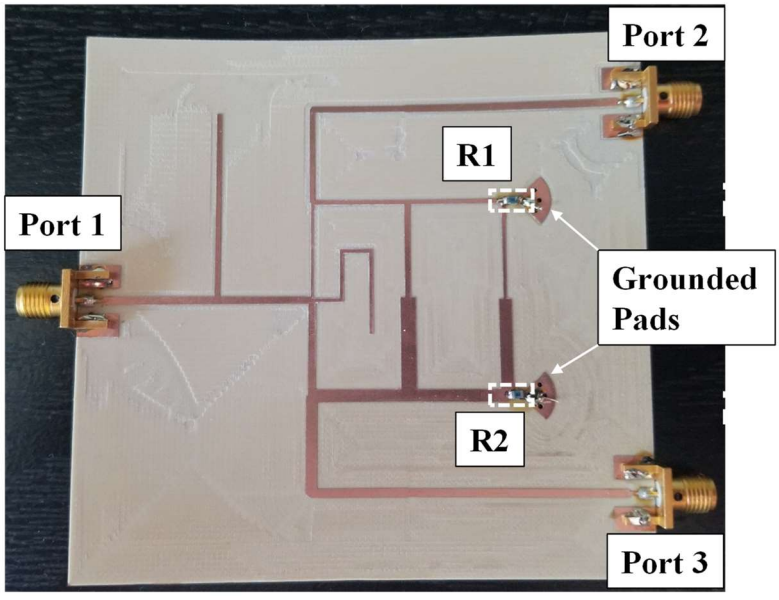


Figure 3-20 Assembled unequal split Knochel-Mayer prototype.

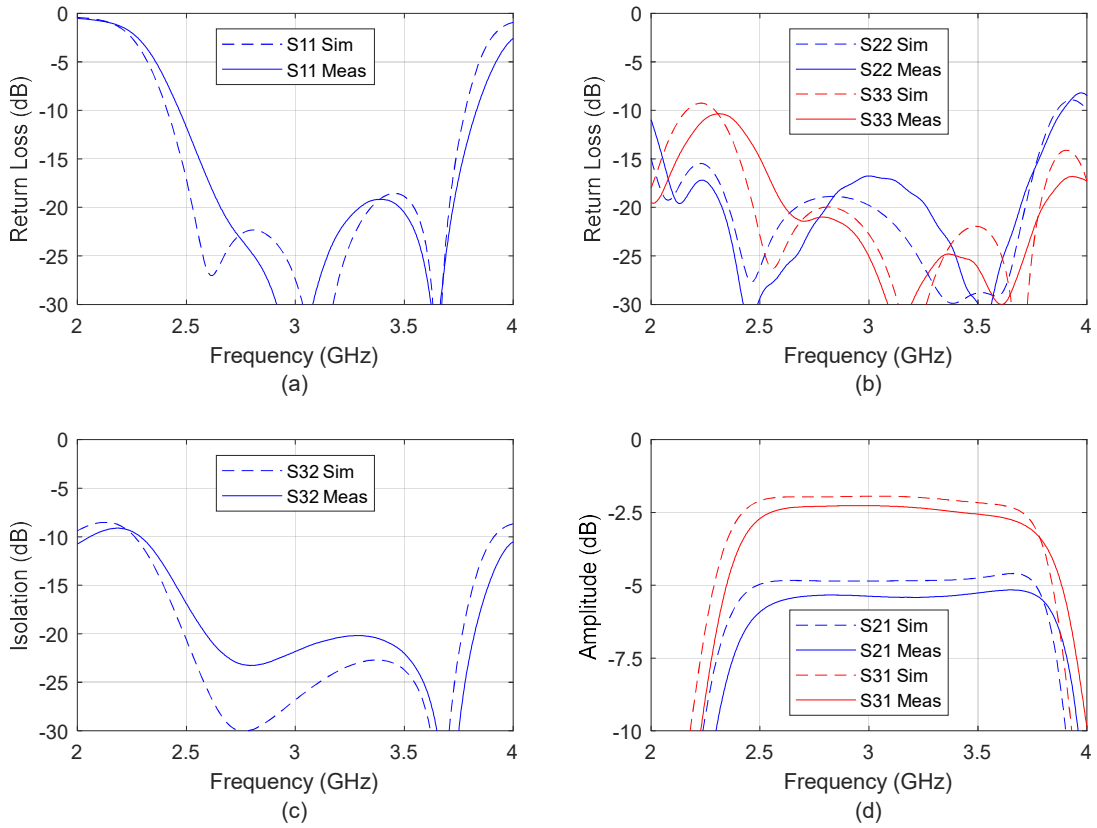


Figure 3-21 Unequal split (2:1) Knochel-Mayer simulation and measured results a) input return loss, b) output return loss, c) isolation and d) amplitude.

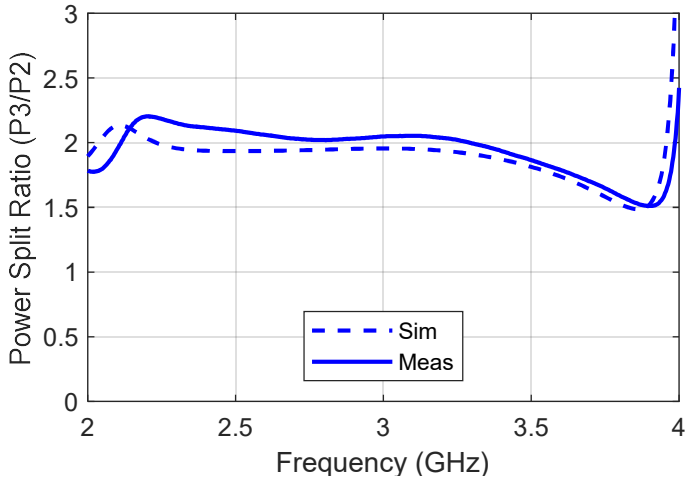


Figure 3-22 Unequal split (2:1) Knochel-Mayer simulation and measured power split ratio.

The phase balance from the simulated and measured data is shown together in Figure 3-23. The data from the linear transmission line model (dotted black trace) shows very tight phase balance of less than ±0.5˚ in the operating band and becoming more imbalanced outside of the band. The data from the HFSS model (dashed blue trace) shows a similar tight phase balance but with a slight offset to -1˚. The data from the measured results (solid blue trace) shows the phase balance being +2˚ to +7˚ in the operating band. This shows that there is a longer phase length through the high power path than through the low power path. This is caused by a slightly longer 50 Ω line to the connector in the prototype because there is a difference in length of the dual section quarter wave transformers on the output ports due to the dispersive nature of microstrip. The phase over frequency for a 50Ω microstrip line on the correct substrate with the physical length of this difference is calculated in a circuit simulator. This value was removed from the measured results of the high power path to deemed the data and evaluate the component alone. This is shown in the graph is the dashed green trace and shows 0/+3˚ phase balance.

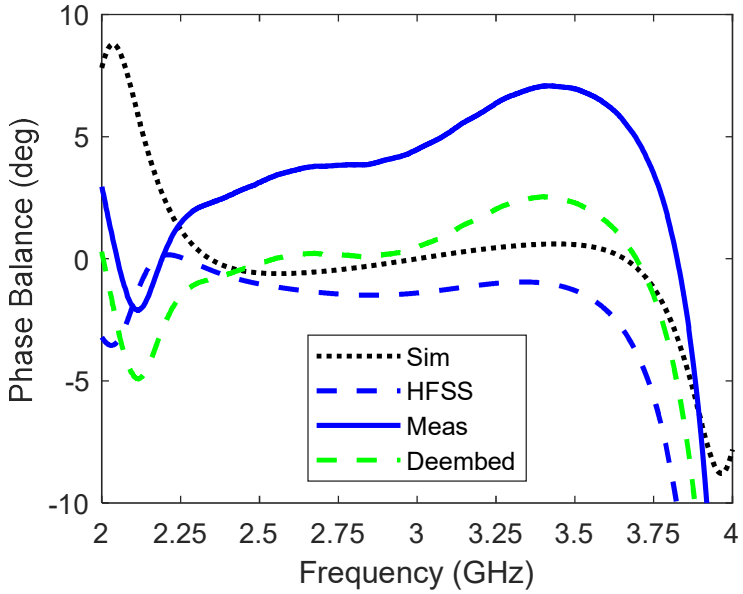


Figure 3-23 Unequal split (2:1) Knochel-Mayer simulation and measured phase balance.

### 3.4.5. Conclusion

A method of designing an unequal split Knochel-Mayer power divider has been shown. The design procedure has been outlined and the results of a 2:1 power split ratio ($K^2 = 2$) Knochel-Mayer prototype have been shown in detail. The simulated and measured data for the proposed component show broadband performance of greater than 30% bandwidth. The return loss and isolation are less than -15dB and the amplitude of each port is within 0.5 dB of the ideal value from 2.5-3.5 GHz.

## 3.5. Bandwidth Enhanced Knochel-Mayer Power Divider

The bandwidth of the original Knochel-Mayer can be increased (or enhanced) to 50% by adding additional sections to the input and isolation network. The component will be referred to as a wideband Knochel-Mayer (WBKM). The design concept used for the *N*-way dividers previously is applied the same way. The bandwidth comparison to other power dividers is shown in Figure 3-24. In this case, there is an additional stub in both the input network and isolation network. Figure 3-25 shows the schematic for a WBKM.

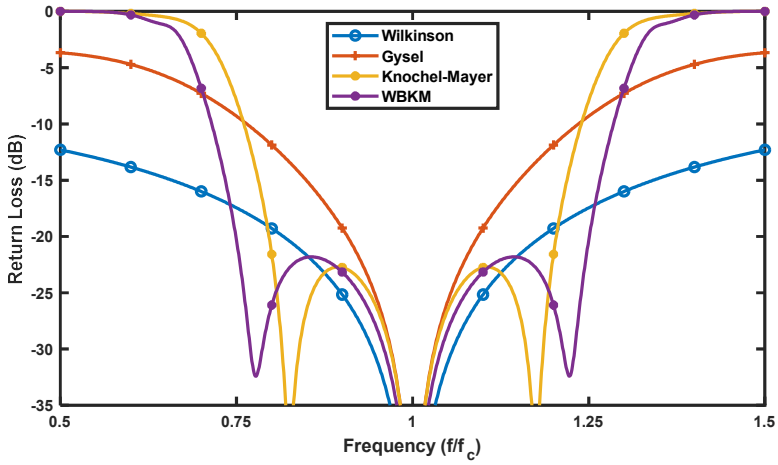


Figure 3-24 Common port return loss comparison of Wilkinson, Gysel, Knochel-Mayer and the WBKM power dividers.

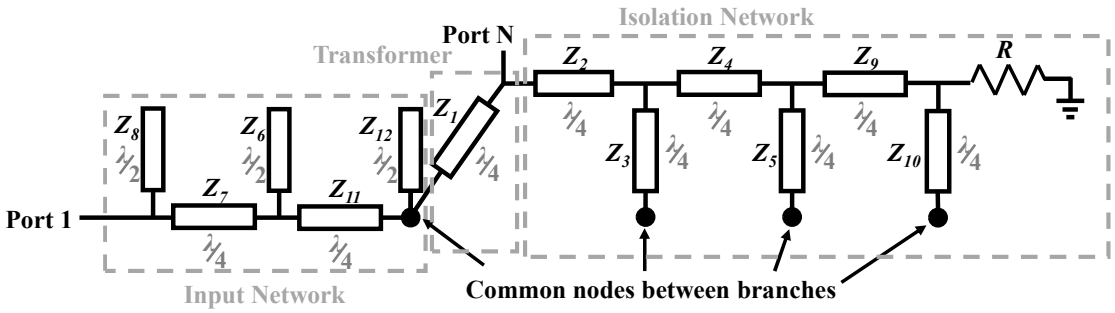


Figure 3-25 Wideband Knochel-Mayer schematic

### 3.5.1. Design Procedure

This design adds sections to the input and isolation networks from the *N*-way Knochel-Mayer. The transmission lines $Z_9$ and $Z_{10}$ are added to the isolation network and transmission lines $Z_{11}$ and $Z_{12}$ are added to the input network. The series lines ($Z_9$ and $Z_{11}$) will be the system impedance, $Z_0$, like in the *N*-way case and the shunt lines $Z_{10}$ and $Z_{12}$ will be part of the tuning. The design procedure is similar to the *N*-way Knochel-Mayer but with the lines $Z_{10}$ and $Z_{12}$ included in the tuning process. The final values of the design for a 2-way equal split power divider are; $Z_1$ = 70.7 Ω, $Z_2$ = 50 Ω, $Z_3$ = 30 Ω, $Z_4$ = 50 Ω, $Z_5$ = 30 Ω, $Z_6$ = 61 Ω, $Z_7$ = 50 Ω, $Z_8$ = 100 Ω, $Z_9$ = 50 Ω, $Z_{10}$ = 42 Ω, $Z_{11}$ = 100 Ω, $Z_{12}$ = 91 Ω, $R$ = 50 Ω.

The simplification of the design that has been used holds the series lines to the system impedance. This simplification will not give an additional null in the band that would be expected from an additional stub. This is because an even order filter transforms to a different impedance and there will not be a null at the center frequency. The performance of the device is not significantly impacted by this simplification.

### 3.5.2. EM Modeling and Simulation

A 3D electromagnetic model of the proposed circuit is built in ANSYS HFSS (shown in Figure 3-26). The circuit is designed in microstrip on a core of 0.508 mm (0.02″) thick and $\varepsilon_r$ = 3.0. The line widths and lengths are calculated using the impedances obtained from the circuit model.

### 3.5.3. High Power Consideration

The prototype is implemented in microstrip technology with edge launch connectors and surface mount resistors. There are three areas of consideration for power handling: the connectors, the microstrip traces, and the surface mount components. The power handling of SMA connectors is widely available from many RF connector suppliers and is well over 200 W in the S-band. The narrowest circuit trace in the design is 12.5 mil and according to IPC 2221A can handle over 1 A of current.

The worst case for the resistors is when the component is used as a combiner. In this case half of the power is delivered to the common port and the other half goes to the resistors. The other branched port is isolated. The full-wave EM simulation is used to show the power distribution with 10 W input into one of the branched ports shown in Figure 3-27. Half of the power is delivered to the common port (Port 1) for the full band. The rest of the power is split between the two resistors. R1 is the resistor closest to Port 2 and R2 is the resistor closest to Port 3. The balance of power is split evenly between the resistors at the center of the band and at the band edges the resistor that is physically closer to the port accepts more of the power. The highest power at either of the resistors is 3 W at the low end of the band. Surface mount resistors with 5 W power handling are used that have a large wrap around ground terminal for effective heat dissipation.

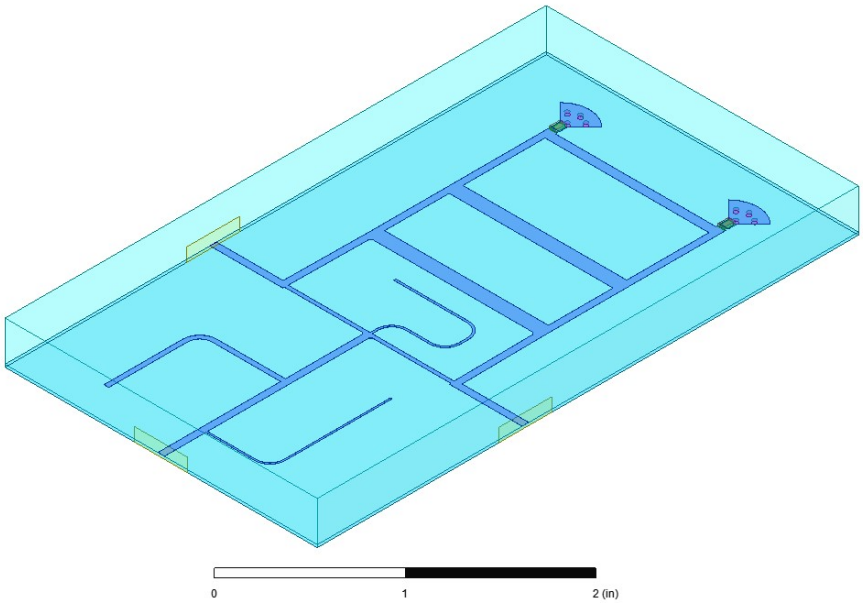


Figure 3-26 3D EM model of bandwidth enhanced Knochel-Mayer prototype.

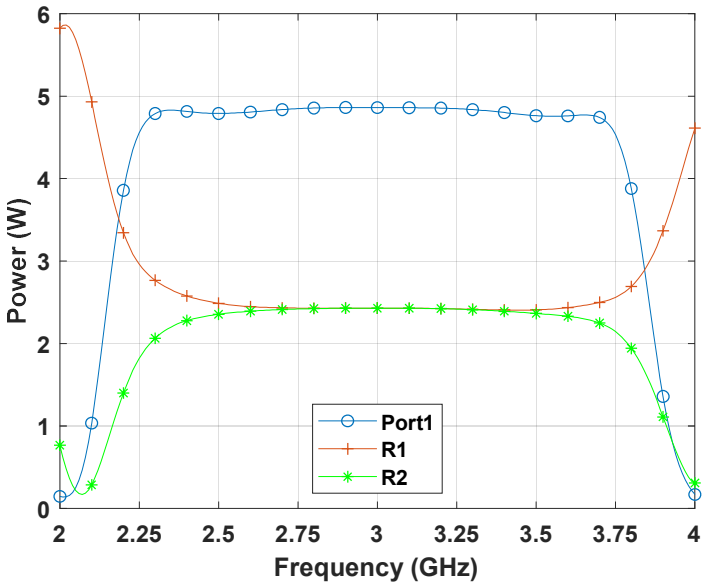


Figure 3-27 Bandwidth enhanced Knochel-Mayer power distribution.

### 3.5.4. Fabrication

The proposed power divider/combiner is realized in microstrip technology on Isola Astra substrate ($\varepsilon_r$ = 3.0, Height = 0.508 mm). SMA edge launch connectors and the resistors are soldered

to the board. The resistors used are surface mount high power thin film chip terminations from Susumu. The assembled prototype is shown in Figure 3-28.

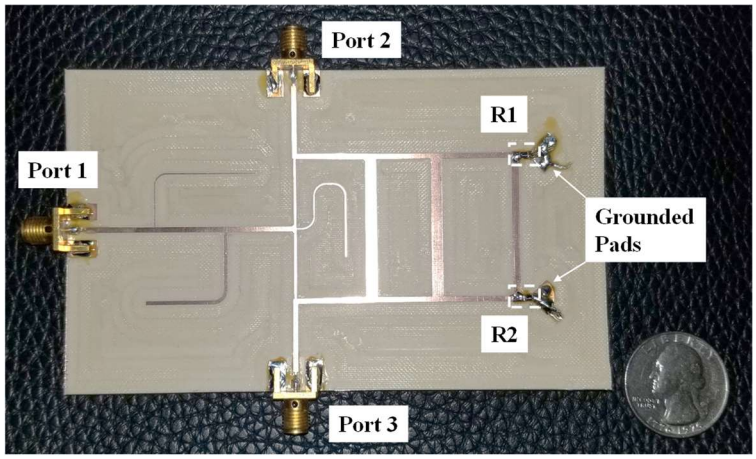


Figure 3-28 Assembled bandwidth enhanced Knochel-Mayer prototype.

### 3.5.5. Testing and Measured Results

The fabricated WBKM power divider has been tested for validation. To perform the high power testing, RF power of 10 W at 2.25GHz and 3.75 GHz is applied to Port 2, terminating Port 3 in 50 Ω. These frequencies are the band edges and represent the highest power into the resistors. This input power level is measured and monitored through a directional coupler. This reduces the power to the power meter so that it does not exceed the max power requirement of the meter. The power at Port 1 is monitored during testing to verify proper output power. The block diagram of the test setup is shown in Figure 3-29. The power is applied at each frequency for a duration of 10 min to ensure that temperature of the component has stabilized. The temperature stabilization shows that prototype has reached equilibrium and is able to handle the input power. Another power divider not specifically designed for high power (such as the Wilkinson) would not be able to handle this power and the resistor would fail, causing a significant degradation in output return loss and isolation. The temperature is measured using a thermocouple mounted to the ground plane

underneath R1. The monitoring data of the temperature and the output power are shown in Figure 3-30. These show that the temperature stabilized and that the component maintained functionality because the output power remained stable at the expected value.

The S-parameters are measured before and after high power exposure to verify the power handling capability. The simulated results, along with the pre and post high power exposure measurement data are shown in Figure 3-31. The return loss and isolation are ≤ -15 dB and the amplitude balance is ±0.25 dB from 2.25-3.75 GHz. The pre and post high power exposure data correlates, confirming the high power handling capability of the prototype.

The phase balance from simulated and measured data is shown together in Figure 3-32. The simulated phase data from HFSS (solid red trace) shows nearly perfect phase balance. The measured phase data (solid blue and green traces) shows a -2˚ phase balance worst case over the operating bandwidth. There is slight change of 2˚ at the low end of the band between the pre and post high power exposure measurements but this is minimal. A slight change is also seen between the pre and post high power exposure measurements of the other parameters previously discussed at the low end of the band but this is also minimal and could be due to test repeatability.

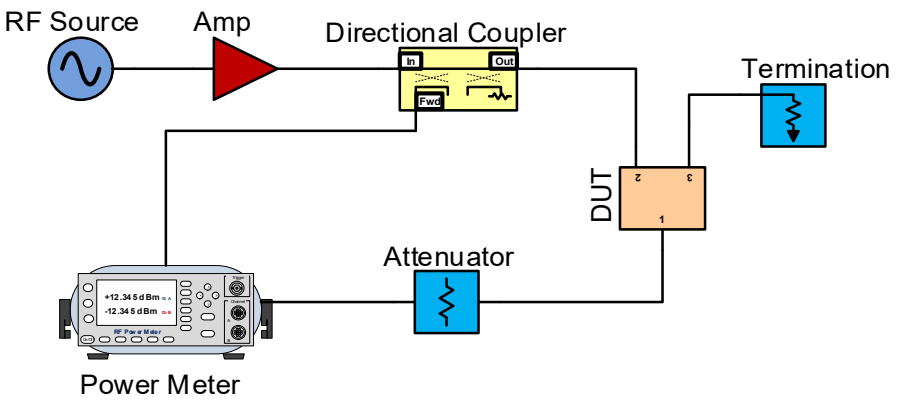


Figure 3-29 High power test setup.

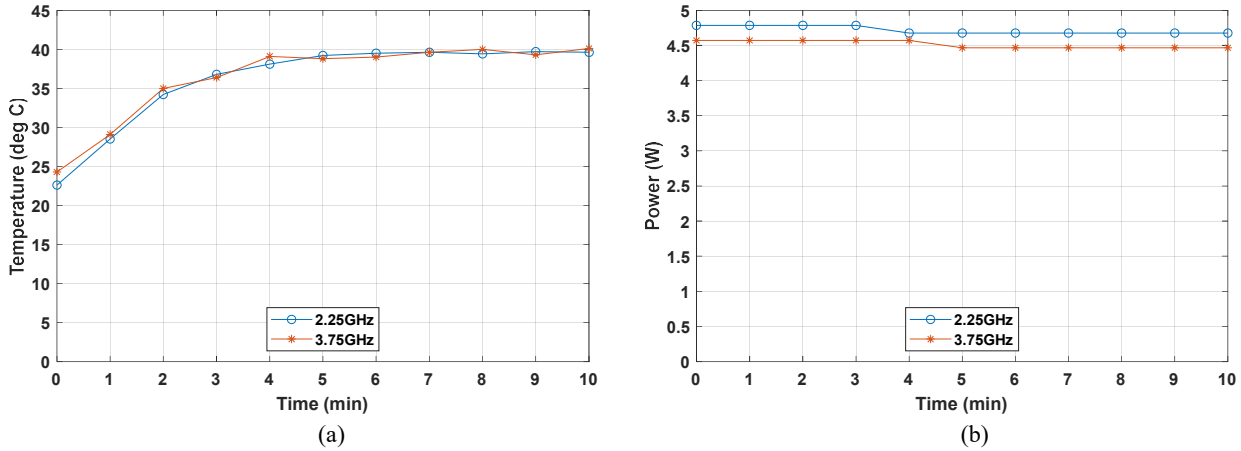


Figure 3-30 High power test monitoring results a) temperture of prototype and b) output power.

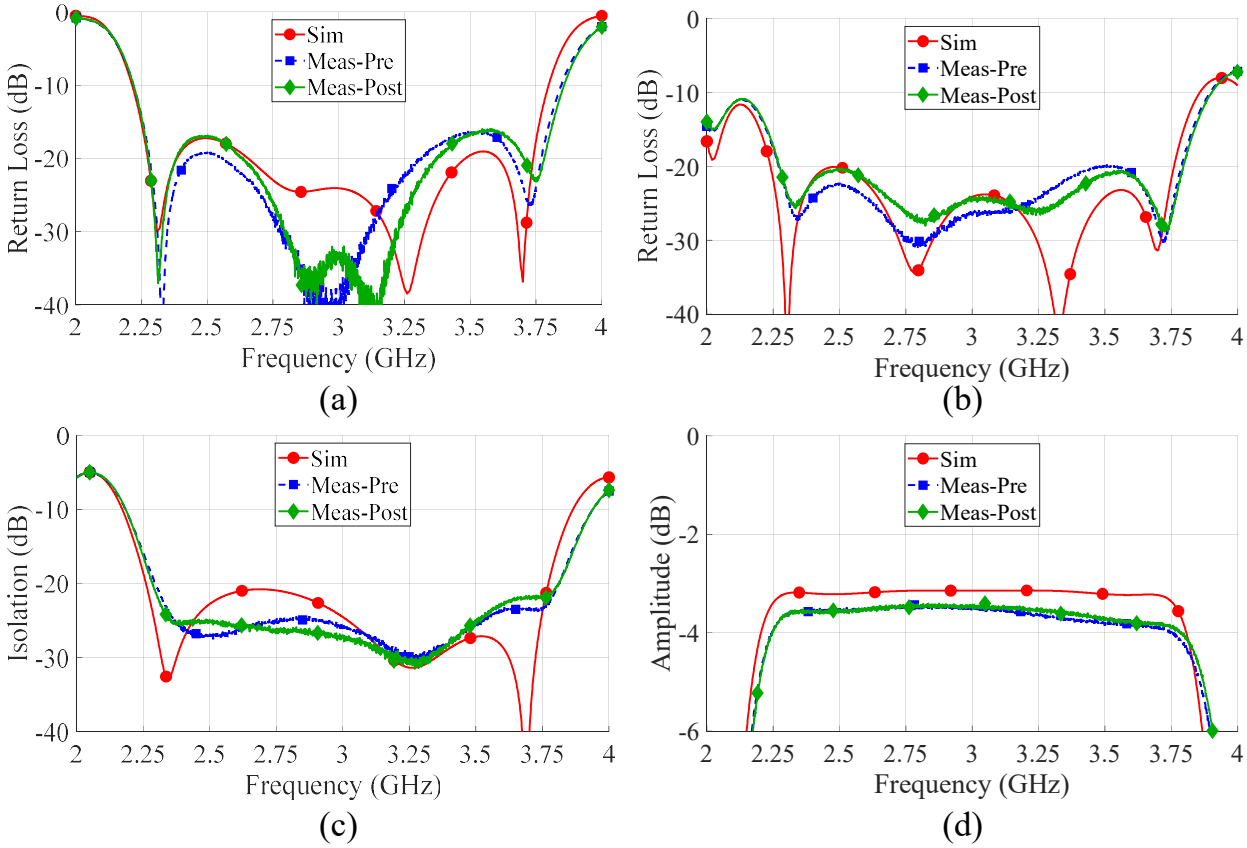


Figure 3-31 Measured results (a) common port return loss (b) branched port return loss (c) isolation (d) amplitude.

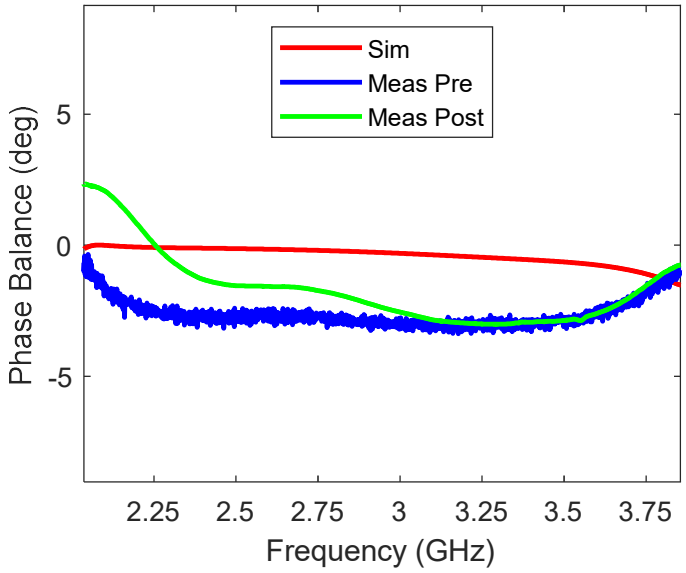


Figure 3-32 Measured phase balance results.

### 3.5.6. Conclusion

A method of broadening the bandwidth of the Knochel-Mayer and designing the *N*-way case has been proposed in this section. The design procedure has been outlined and the results of a 2-way prototype have been shown in detail. The simulated and measured data for the proposed component show broadband performance from 2.25-3.75 GHz (50% bandwidth) and a power handling capability of 10 W average power. The prototype validated the wideband performance and the high power capability of the design improving upon the typical Wilkinson that would be less than 1 W on the same substrate and frequency range.

## 3.6. Ultra-Wideband Knochel-Mayer Power Divider

The bandwidth of the Knochel-Mayer structure is further increased to 60% by adding additional sections to the input and isolation network. The component will be referred to as an ultra-wideband Knochel-Mayer (UWBKM). The design concept used for the *N*-way dividers previously is applied the same way. The bandwidth comparison to other power dividers is shown in Figure 3-33. In this

case, there is an additional stub in both the input network and isolation network. Figure 3-34 shows the schematic for an UWBKM.

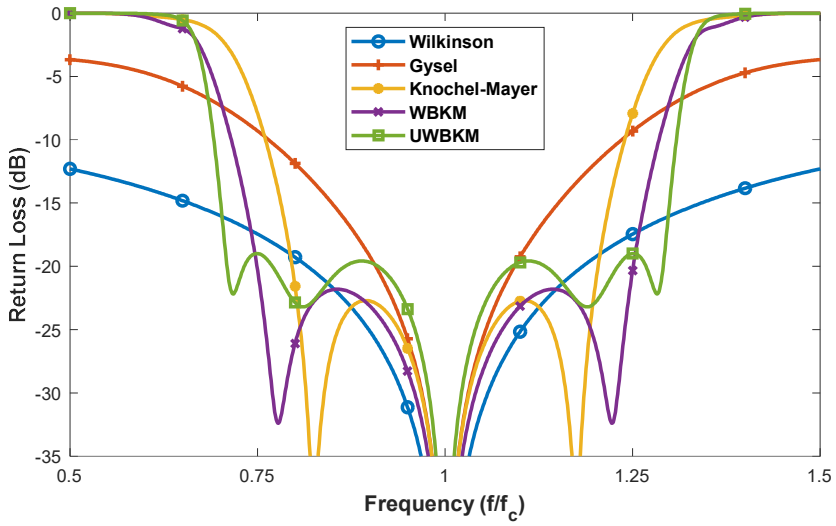


Figure 3-33 Common port return loss comparison of Wilkinson, Gysel, Knochel-Mayer, wideband Knochel-Mayer and ultra-wideband Knochel-Mayer power dividers.

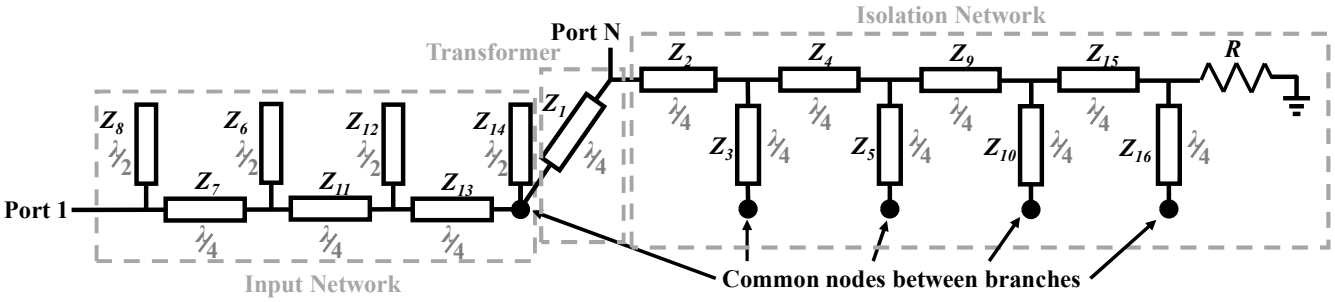


Figure 3-34 Ultra wideband Knochel-Mayer schematic.

### 3.6.1. Design Procedure

An UWBKM can be designed using the same procedure as previously used for the other cases. This design adds sections to the input and isolation networks from the wideband Knochel-Mayer. The transmission lines $Z_{15}$ and $Z_{16}$ are added to the isolation network and transmission lines $Z_{13}$ and $Z_{14}$ are added to the input network. The series lines ($Z_{13}$ and $Z_{15}$) will be the system impedance

$Z_0$ like in the $N$-way case and the shunt lines $Z_{14}$ and $Z_{16}$ will be part of the tuning. The design procedure is similar to the $N$-way Knochel-Mayer but with the lines $Z_{14}$ and $Z_{16}$ included in the tuning process. The final values of the design are; $Z_1$ = 70.7 Ω, $Z_2$ = 50 Ω, $Z_3$ = 31 Ω, $Z_4$ = 50 Ω, $Z_5$ = 27 Ω, $Z_6$ = 112 Ω, $Z_7$ = 50 Ω, $Z_8$ = 90 Ω, $Z_9$ = 50 Ω, $Z_{10}$ = 33 Ω, $Z_{11}$ = 50 Ω, $Z_{12}$ = 52 Ω, $Z_{13}$ = 50 Ω, $Z_{14}$ = 165 Ω, $Z_{15}$ = 50 Ω, $Z_{16}$ = 27 Ω, $R$ = 50 Ω.

### 3.6.2. EM Modeling and Simulation

A 3D electromagnetic model of the proposed circuit is built in ANSYS HFSS (shown in Figure 3-35). The circuit is designed in microstrip on a core of 0.508 mm (0.02″) thick and $\varepsilon_r$ = 3.0. The line widths and lengths are calculated using the impedances obtained from the circuit model.

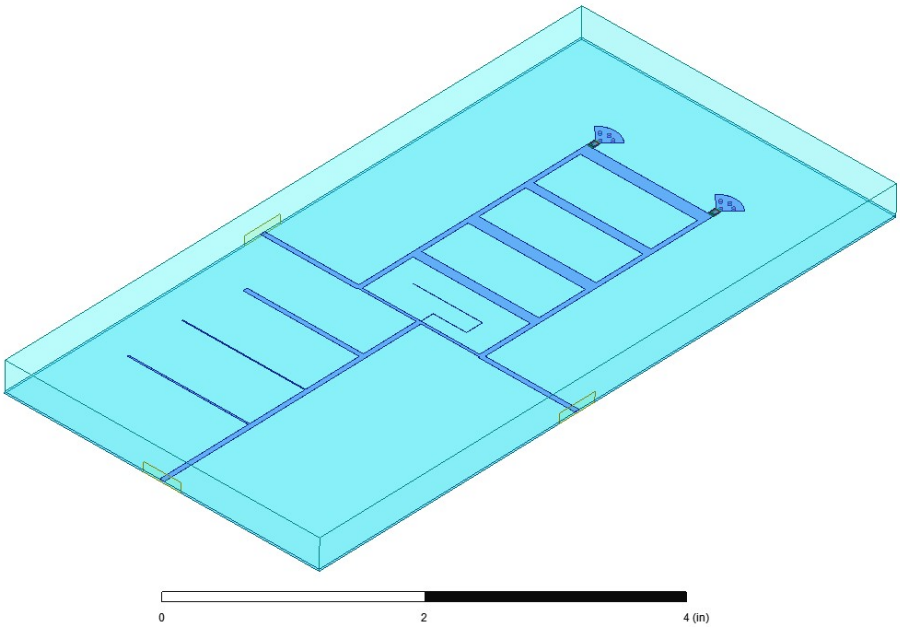


Figure 3-35 3D EM model of ultra-wideband Knochel-Mayer prototype.

The simulated results are shown in Figure 3-36. The UWBKM operates from 2.1-3.9 GHz (60% WB). The input return loss, output return loss and isolation are all -15 dB or better and the

amplitude has less than 1 dB of variation for the entire band. The phase balance results are shown in Figure 3-37 and it has less than 1˚ of variation for the entire band.

### 3.6.3. Conclusion

The bandwidth is shown to be expanded to 60% (2.1-3.9 GHz). The line impedances of some of the lines are becoming prohibitively high and the increase in bandwidth is not as much as the previous section so it is approaching diminishing returns. Due to the narrow line widths required to implement the high impedances, a prototype was not possible to be fabricated with the available equipment.

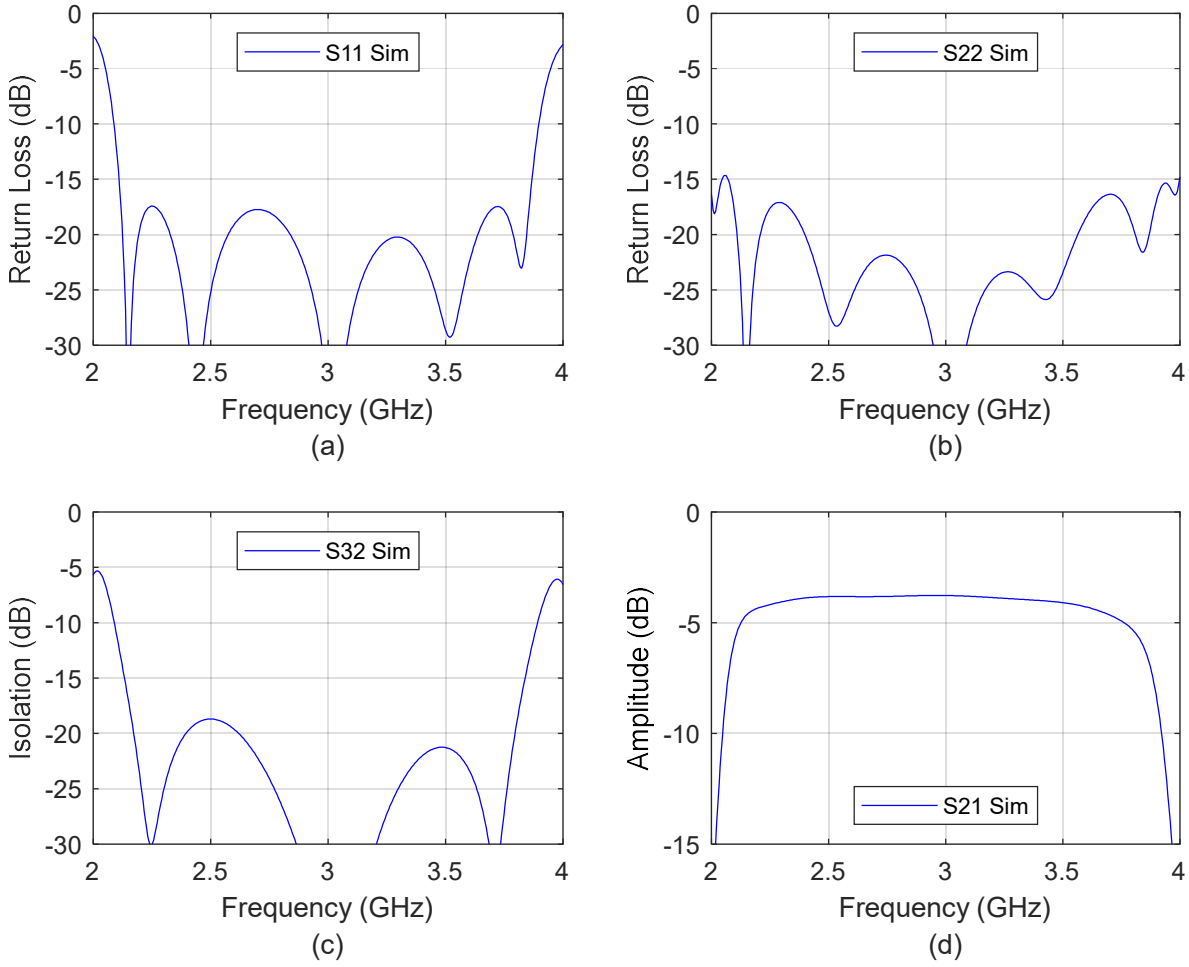


Figure 3-36 Ultra wideband Knochel-Mayer simulated results (a) common port return loss (b) branched port return loss (c) isolation (d) amplitude.

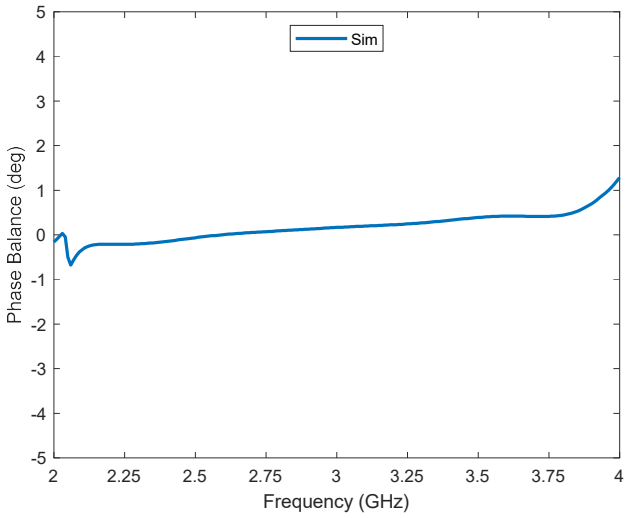


Figure 3-37 Ultra wideband Knochel-Mayer simulated phase results.

### 3.7. Broadband Power Dividers Conclusion

The original Knochel-Mayer power divider structure has been thoroughly analyzed and the concept has been expanded to designs with multiple outputs and unequal power split ratios. These altered variations maintain the broad bandwidth of 30% and the potential for high power handling. This was demonstrated with a 4-way power divider and a 2:1 unequal split ratio 2-way power divider. The bandwidth was also widened by adding additional sections. This was demonstrated with a 2-way equal split prototype that achieves 50% bandwidth. The high power handling of this device was verified with test showing a capability of 10W input power handling over the entire operating bandwidth. A design capable of 60% BW was also shown through simulation, though not fabricated.

# Chapter 4. Multiband Antenna Arrays Using Multiplexed Antenna Feeds

## 4.1. Introduction

An array with a bandwidth greater than 30% will not operate properly when using a single element spacing. An antenna feed that will cover the bandwidth is still required, but another solution needs to be implemented to address the degradation due to the element spacing previously discussed. The concept of creating multiband antenna arrays using multiplexed antenna feeds to address this problem is presented in this chapter. CRLH-TL isolation circuits are used to multiplex the antennas. A 1D multiband scanning array is designed using CRLH-TL isolation circuits and microstrip patch antennas in a linear arrangement. A concept is proposed to expand the linear array for 2D scanning by using leaky-wave antennas (LWAs). This type of array can steer the beam in one dimension with frequency and the other with the phase between elements. This requires a LWA that is suitable for multiplexing. A LWA with improved out of band rejection is designed for this purpose.

Consider a system using GPS, 5G, and Vehicle-to-everything (V2X) (IEEE 802.11p). For the GPS, $f_1$ = 1.59 GHz, for the 5G the $f_2$ = 3.75 GHz (in the n77 band) and for the V2X $f_3$ = 5.9 GHz. The array performance is calculated for all three bands in each case with the spacing optimized at one of the bands. The degradation of the array performance of the other bands with the spacing between elements optimized at one band can be seen in Figure 4-1 through Figure 4-3. In these plots a nine element array is used with a beam steered to +30˚. With the element spacing optimized for Band 1, grating lobes appear in the field of view for Bands 2 and 3, as shown in Figure 4-1. With the element spacing optimized for Band 2, the main beam in Band 1 is degraded (widened) and grating lobes appear in the field of view for Band 3, as shown in Figure 4-2. With the element

spacing optimized for Band 3, the main beams in Bands 1 and 2 are degraded with the main beam of Band 1 severely degraded, as shown in Figure 4-3.

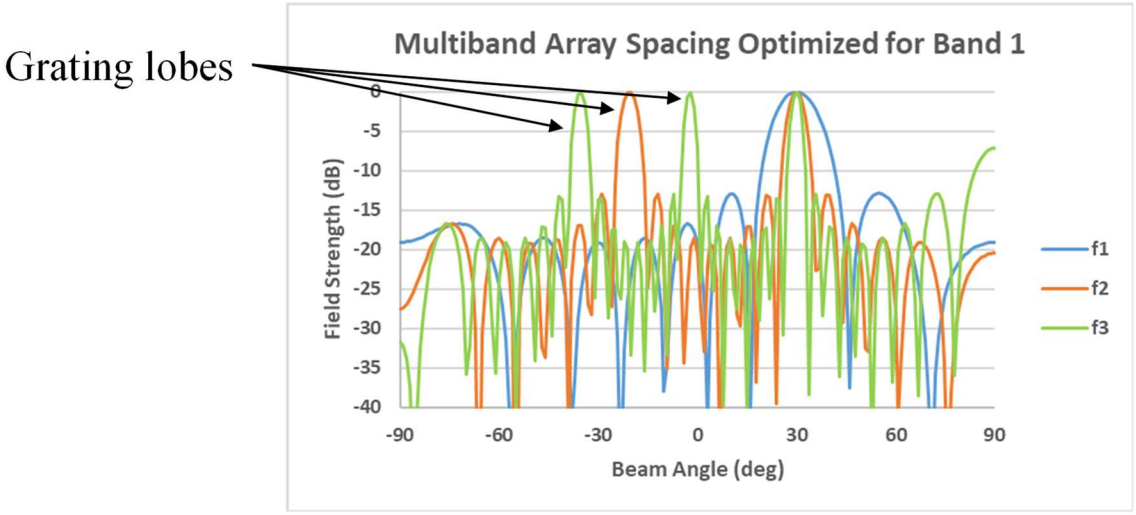


Figure 4-1 Nine element antenna array with spacing optimized for Band 1.

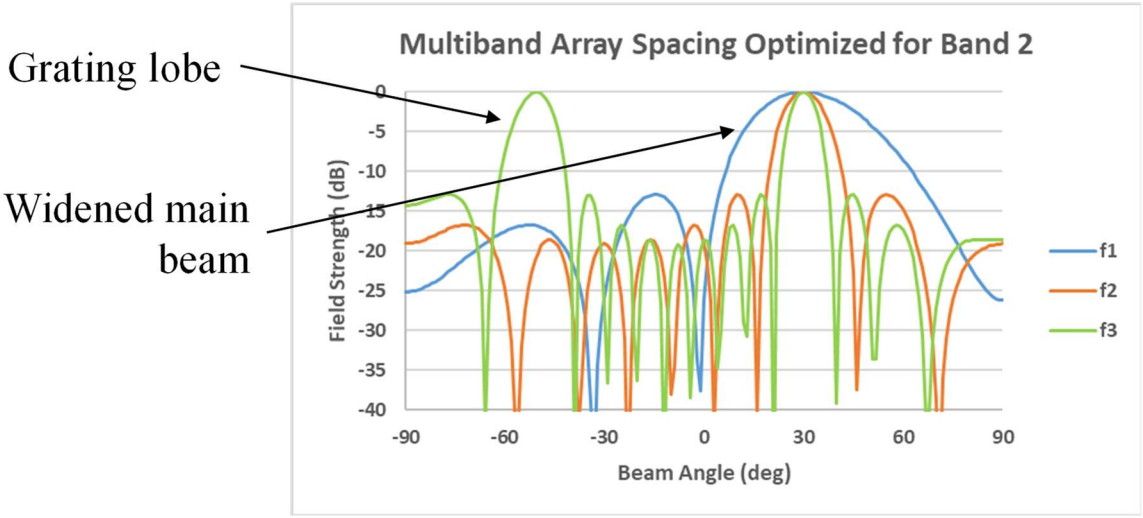


Figure 4-2 Nine element antenna array with spacing optimized for Band 2.

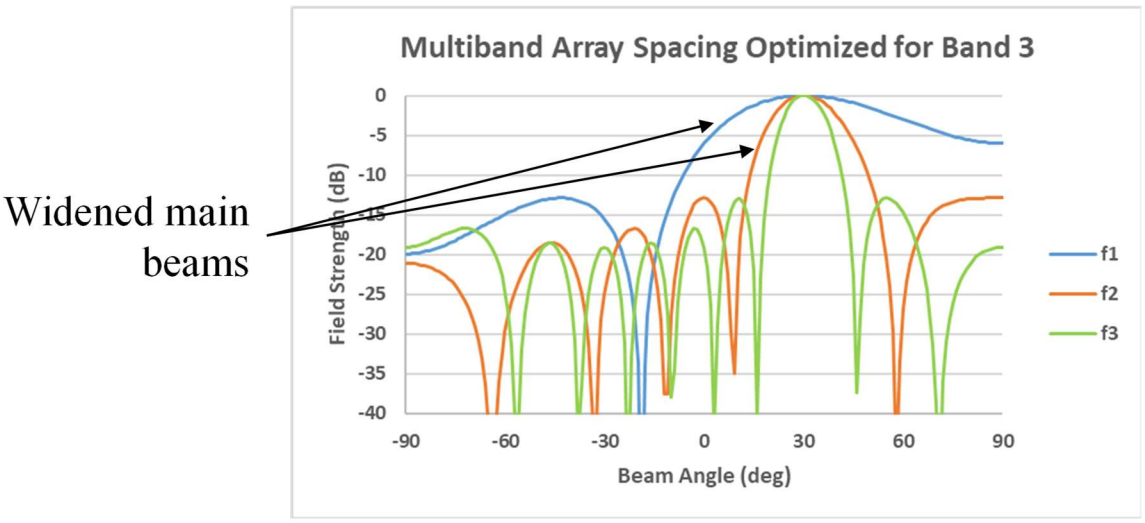


Figure 4-3 Nine element antenna array with spacing optimized for Band 3.

A method to overcome this limitation is to use a multiband antenna with separate radiating elements so that could each band's radiators can be placed independently from the other band's radiators. These antennas could be used in an array with optimal element spacing for each band. A convenient way to implement this is to use separate antennas for each band and combine them to a common input. This approach will simplify the antenna design because each band will only require simple single band antennas which should not present any significant design challenge. With this configuration, the group of antennas can be handled as a single element in an antenna feed and the element spacing at the different bands can be optimized uniquely. The concept of this type of antenna is illustrated in Figure 4-4. The implementation of connecting of these multiple antenna elements to a single input can be done in several ways such as some type of switching or multiplexing.

Switches can be used to connect multiple antennas to common node. Switches are available with multiple positons and very wide frequency ranges. Switches have been used in multiple antenna systems in several different ways though typically not for multiband purposes. The

function of the switches in these systems is to switch beams or change beam shape.

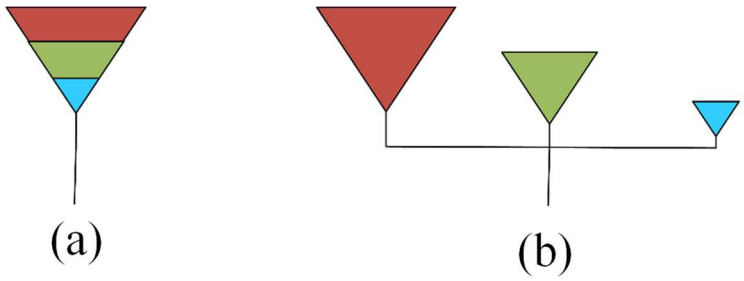


Figure 4-4 Multiband antennas a) typical single radiator and b) separarte radiators with a common feed.

Switches are sometimes used to change the 'look" direction. This is achieved by switching between antenna elements that are physically aimed in different directions. In the work of Yang et al. [40] two antennas (on either side of a back-to-back microstrip) are switched between to "look" in one direction or the opposite. In the work of Li and Hao [41], four antennas (on four sides of an enclosure) are switched between for 360° scan capability.

Switches can also be used to switch between ports on a fixed beamformer. In the work of Lamminen et al. [42], a single RF input port is switched to the different input ports of a Rotman lens to control the beam direction. The same approach is done by Kim et al. [43] with a Butler matrix replacing the Rotman lens in the previous example. The switches in Nguyen and Park [44] are used to change the direction and pattern of the beam for MIMO applications.

Wideband switches are readily available and could be used for the connecting the different antennas to a single port, however there are several downsides to this approach. Switches are active devices and require additional sources of power and control. Also, only one antenna can be selected

at a time with the others isolated from the common port. A scheme of when to switch to which antenna would need to be implemented. In receive mode there would be no way to know which band to be switched to without some additional sensors. The switching speed of the switches could also reduce the effective use of the multiple bands and the switching frequency could cause interference issues that would need to be mitigated.

A multiplexed solution is a preferred option because it can be implemented passively and all bands would always be active and can be used simultaneously. This can be done with conventional RF multiplexers that implement RF filter technology. The implementation of this however is not trivial and becomes more difficult as the number of channels increases. Also, at low frequencies these will become large.

Composite Right/Left-Handed Transmission Lines (CRLH-TL) isolation networks from Lee and Itoh [45] were implemented to realize multiplexers using commercial off the shelf filters. These networks used lumped element components to implement the left-handed values and standard transmission lines for the right-handed values. This approach has advantages over conventional RF multiplexers because of its simple design procedure and that it does not become larger at lower frequencies. The size only depends on the filters used. This concept can be used with antennas in place of the filters to multiplex antenna feeds directly without the need for discrete filters. This will work due to the band limiting nature of most antennas. In this chapter multiplexed antenna feeds composed of these lumped element CRLH-TLs are used in antenna arrays. These are used to design a multiband 1D scanning array of patch antennas in a linear configuration and is experimentally demonstrated. The antennas used in this case are a reflective type and can be directly connected to the CRLH-TL multiplexing network.

A concept for expanding the beam steering of this approach to 2D is presented later in this

chapter. This is implemented while maintaining the linear array configuration for ease of layout. It is much easier to implement multiple linear arrays as opposed to multiple N x M arrays on the same plane. By using a linear array of frequency scanning antennas, 2D beam scanning can be achieved by using a combination of phase control and frequency. This type of array has been previously implemented in Enders and Choi [46] and Kaneda et al. [47]. In this configuration, the phase between elements would be used to steer the beam in one direction and the frequency will steer the beam in the other direction. A key challenge with implementing these types of antennas with the CRLH-TL isolation circuits is the fact that frequency scanning antennas do have sufficient stop bands and therefore cannot be directly multiplexed like the resonant antennas used in the 1D scanning case. A frequency scanning antenna with improved out of band rejection will be analyzed and designed to overcome this issue and allow for use in the 2D scanning array. The prototype antenna will be designed and fabricated and then validated experimentally. The results are discussed in this chapter.

### 4.2. CRLH-TL Isolation Circuits

CRLH TL's have a left hand region and a right had region in which the phase behaves differently and can be controlled independently. Isolation circuits can be designed with CRLH TLs using this dual nature. A CRLH TL connected to a band pass filter (or any band limited device with strong out of band rejection) can have an input impedance of $Z_0$ for in band frequencies and $\infty$ for out-of-band frequencies. This can be accomplished with the proper phase shift before the filter. A Smith chart representation for this concept is shown in Figure 4-5. The real part of the complex impedances ($Z = \alpha + j\beta$) of the antennas at the non-operating frequencies is nearly zero ($\alpha \approx 0$). This leaves only the imaginary part of the impedance which places it on

the edge of the Smith chart. A transmission line can be used to move this impedance to the open-circuit position on the Smith chart. The clockwise direction, $\phi_1$, shows the right-handed phase delay and the counter clockwise direction, $\phi_2$, shows the left-handed phase advance. Phase rotation, either clockwise or counter clockwise, is achieved using CRLH TL in the balanced condition with the method described in [48] and [49].

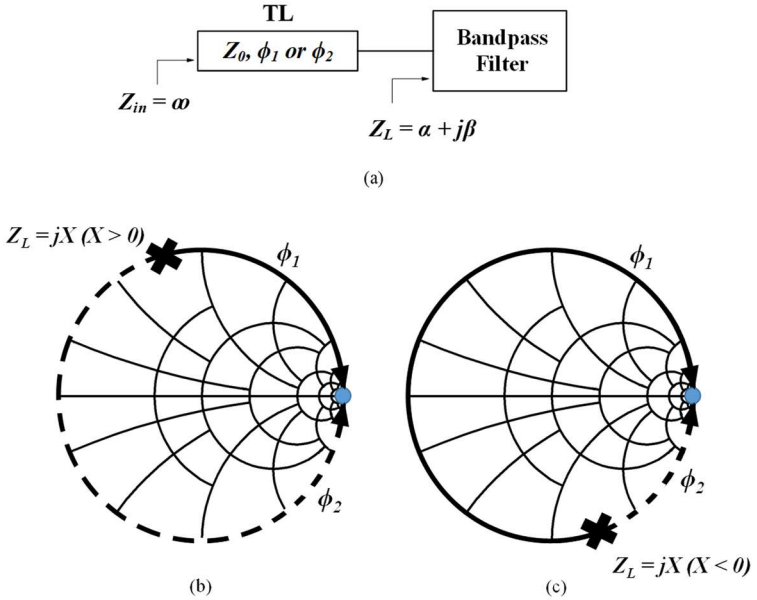


Figure 4-5 (a) An isolation circuit diagram. (b) An example of the input impedance $Z_L$ shown on the Smith chart (Case 1: X > 0 and α = 0). (c) An example of the input impedance $Z_L$ shown on the Smith chart (Case 2: X < 0 and α = 0).

The input impedance that is required for these isolation networks out of band is infinite and this occurs when the denominator of Eq. (4.1) is zero,

$$Z_{in} = Z_0 \frac{Z_L + jZ_0 \tan(-\phi)}{Z_0 + jZ_L \tan(-\phi)}. \tag{4.1}$$

The required phase shift $\phi$ can be found using the following equation [39],

$$\phi = n\pi - \arctan\left(\frac{Z_0}{Z_L}\right) + \psi \tag{4.2}$$

where $n$ is -1, 0, or 1. $Z_0$ is the characteristic impedance of the TL and $Z_L$ is the input impedance of the filter. $\psi$ is a tuning term for reasonable values and it is close to zero. The proper n is chosen from the input impedance of the filter at the center frequencies of the other filters to be isolated.

These isolation circuits can be implemented using a hybrid of traditional transmission line and lumped element left-handed components. A schematic representation is shown in Figure 4-6. These can be connected using a star junction (single node) without effecting the performance of each other in their own operating bands. The branches leading to the out-of-band filters are high impedance at the center frequency of the desired filter. Only the branch leading to the desired filter has a 50 Ω impedance and therefore all the power is transferred to that filter.

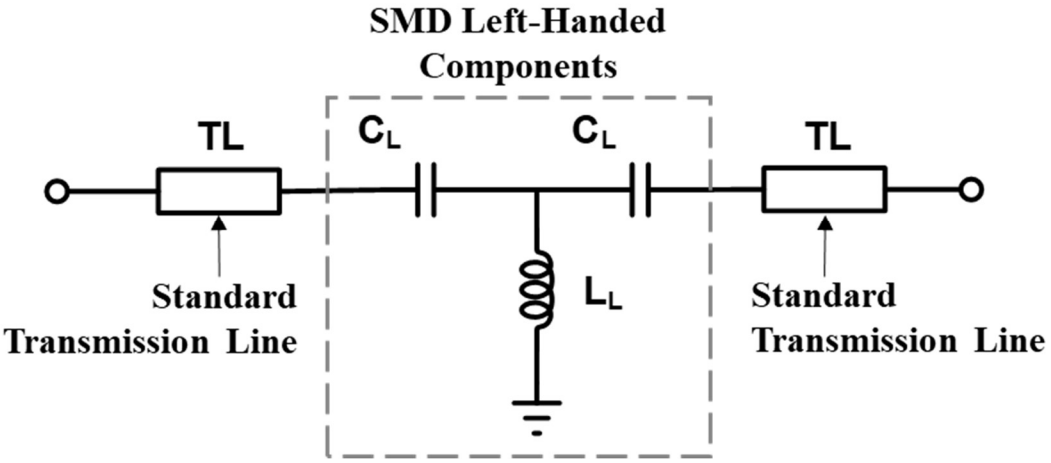


Figure 4-6 Schematic of hybrid lumped element CRLH-TL isolation circuit.

Antennas used in place of the filters in these isolation circuits will create a multiplexed antenna feed. This will enable the multiple antennas to be connected to a single input and allow the antenna elements to be located independently. The input to this isolation network can be treated as a single

element for the purposes of array design. A wide band feed network can feed an array of these multiplexed antenna feeds with each band having its own optimized element spacing for proper array performance.

The tri-band antenna array consists of three operating bands: 1.59 GHz, 3.75 GHz, and 5.9 GHz. The inter-element spacing is designed to be $\lambda_0/2$ at each band's center frequency. The element spacing in band 1 (1.59 GHz) is 94.34 mm, band 2 (3.75 GHz) is 40 mm and band 3 (5.9 GHz) is 25.42 mm. If the physical spacing of the band 1 elements was used for the band 2 elements, the equivalent spacing would be equal to $1.2\lambda_0$ at the band 2 center frequency and if that spacing was used for the band 3 elements, the equivalent spacing would be equal to $1.9\lambda_0$ at the band 3 center frequency. This would result in early onset of grating lobes of band 2 and band 3 as the beam was steered. If a multiband antenna was used instead of the multiplexed antenna network proposed, the inter-element spacing would be fixed across the bands and the performance of the array could only be optimized for one band and would suffer at the others. The ability to control this spacing uniquely for each band is the main advantage of this design to maintain proper operation of the array in each band.

### 4.3. 1D Scanning Antenna Array Comprised of Multiplexed Antenna Feeds

A multiband antenna array with 1D scanning capability is created using the multiplexed antenna feeds created with the CRLH-TL isolation circuits. Figure 4-7 shows the block diagram of the multiplexed antenna feed. Individual patch antennas are designed for each band and arranged in linear arrays with the proper spacing for each band and then connected with the isolation circuits. The linear array spacing gives the array beam scanning capability in one dimension.

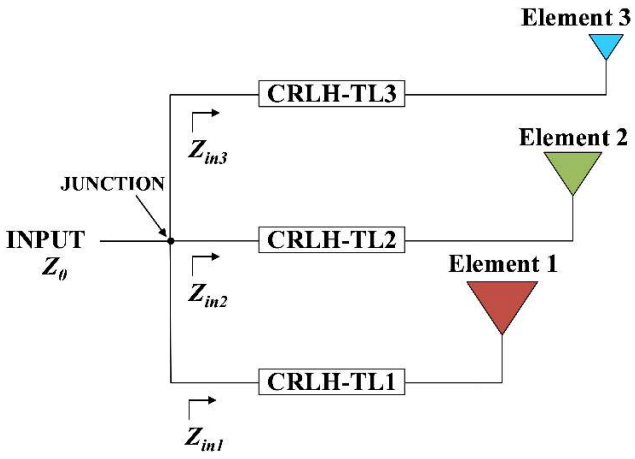


Figure 4-7 Multiplexed antenna feed block diagram.

### 4.3.1. Antenna Element Design

The antenna elements that are used for the1D scanning array are microstrip rectangular patch antennas. These are one of the simplest planar antennas. They are simply a patch of metal on the top metal of a substrate above the ground plane and therefore are easily implemented in microstrip technology. The design of these type of antennas has been discussed in many publications. The procedure in [50] was used to design these antennas which includes the design equations Eq. (4.3) through Eq. (4.7).

$$W = \frac{1}{2f\sqrt{\varepsilon_0\mu_0}}\sqrt{\frac{2}{\varepsilon_r+1}}, \tag{4.3}$$

where $f$ is the operating frequency and $W$ is the width of the antenna.

$$\varepsilon_{reff} = \frac{\varepsilon_r+1}{2} + \frac{\varepsilon_r-1}{2\sqrt{1+12d/W}}, \tag{4.4}$$

where $d$ is the thickness of the microstrip substrate.

$$L = \frac{1}{2f\sqrt{\varepsilon_{reff}}\sqrt{\varepsilon_0\mu_0}} - 2\Delta L \tag{4.5}$$

$$\Delta L = 0.412d(\varepsilon_{reff} + 0.3)(\frac{W}{d} + 0.264)/\left[(\varepsilon_{reff} + 0.258)(\frac{W}{d} + 0.8)\right] \quad (4.6)$$

$$x_0 = \frac{L}{\pi}\cos^{-1}\sqrt{\frac{50}{122.69}} \quad (4.7)$$

First the width $W$ is calculated using Eq. (4.3). Then the effective permittivity $\varepsilon_{reff}$ is calculated using Eq. (4.4). The length $L$ can then be calculated with Eq. (4.5) using the effective length due to fringing $\Delta L$, defined in Eq. (4.6). Finally the insert length $x_0$ can be calculated using Eq. (4.7). The layout implementation of this type antenna is shown in Figure 4-8.

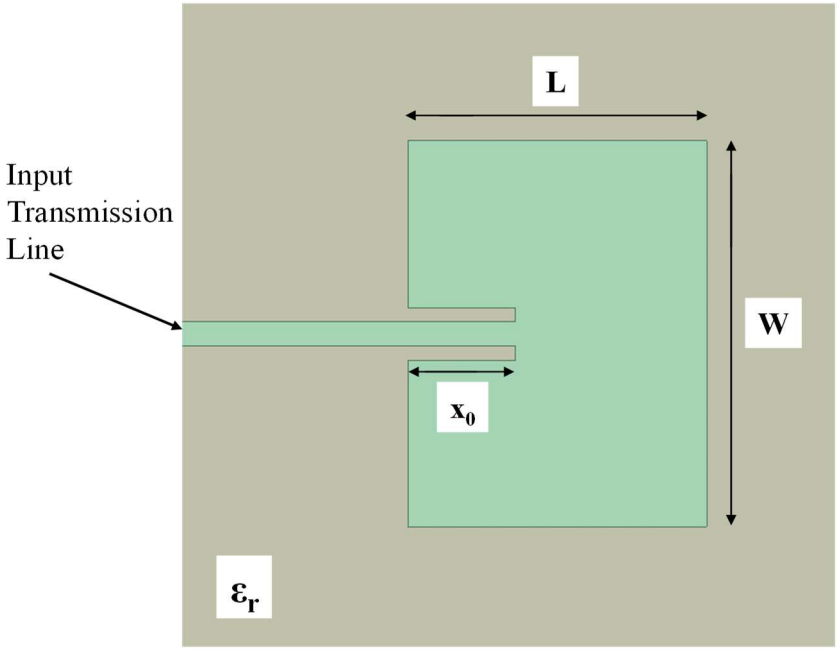


Figure 4-8 Microstrip patch antenna.

The radiation pattern of the microstrip patch antenna can be seen in Figure 4-9. It has a broad radiation pattern above the ground plane. It has a maximum gain at broadside and diminishes as it gets to the end fire direction. The reduced radiation as the angle moves away from broadside is what limits the angle that the beam can be steered when used in an array.

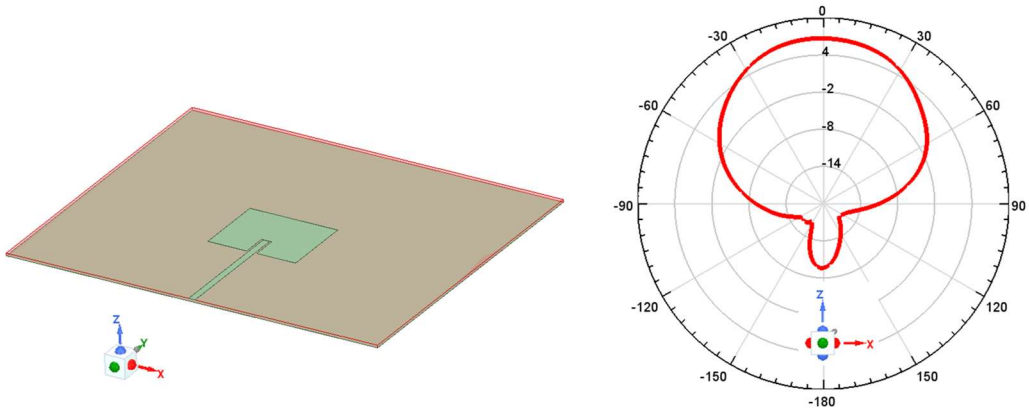


(a) (b)

Figure 4-9 Microstrip rectangular patch antenna a) layout orientation and b) radiation pattern.

The final dimensions for all three band antennas are shown in Table 4-1. The simulated results of the antenna elements for each band are shown in Figure 4-10. In the figure the layout is shown for each antenna element, the return loss of each element is shown to be tuned to each band frequency and that each antenna shows typical radiation pattern for a microstrip patch antenna.

Table 4-1 Patch antenna dimensions.

| | L (in) | W (in) | $x_0$ (in) |
|---|---|---|---|
| **Band 1** | 2.122 | 2.64 | 0.9 |
| **Band 2** | 0.8975 | 1.11 | 0.31 |
| **Band 3** | 0.709 | 0.567 | 0.2 |

### 4.3.2. Multiplexed Antenna Feed and Multiband Array Design

The isolation circuits are designed using the simulated performance of the antenna elements. The schematic of CRLH-TL circuits used is shown in Figure 4-11. There are 5 lumped elements in each circuit and each antenna has its own unique component values and line lengths. The isolation circuits are connected to the applicable antennas and tied to a common port to make the multiplexed antenna feed. The return loss of the common port is evaluated at the three operating

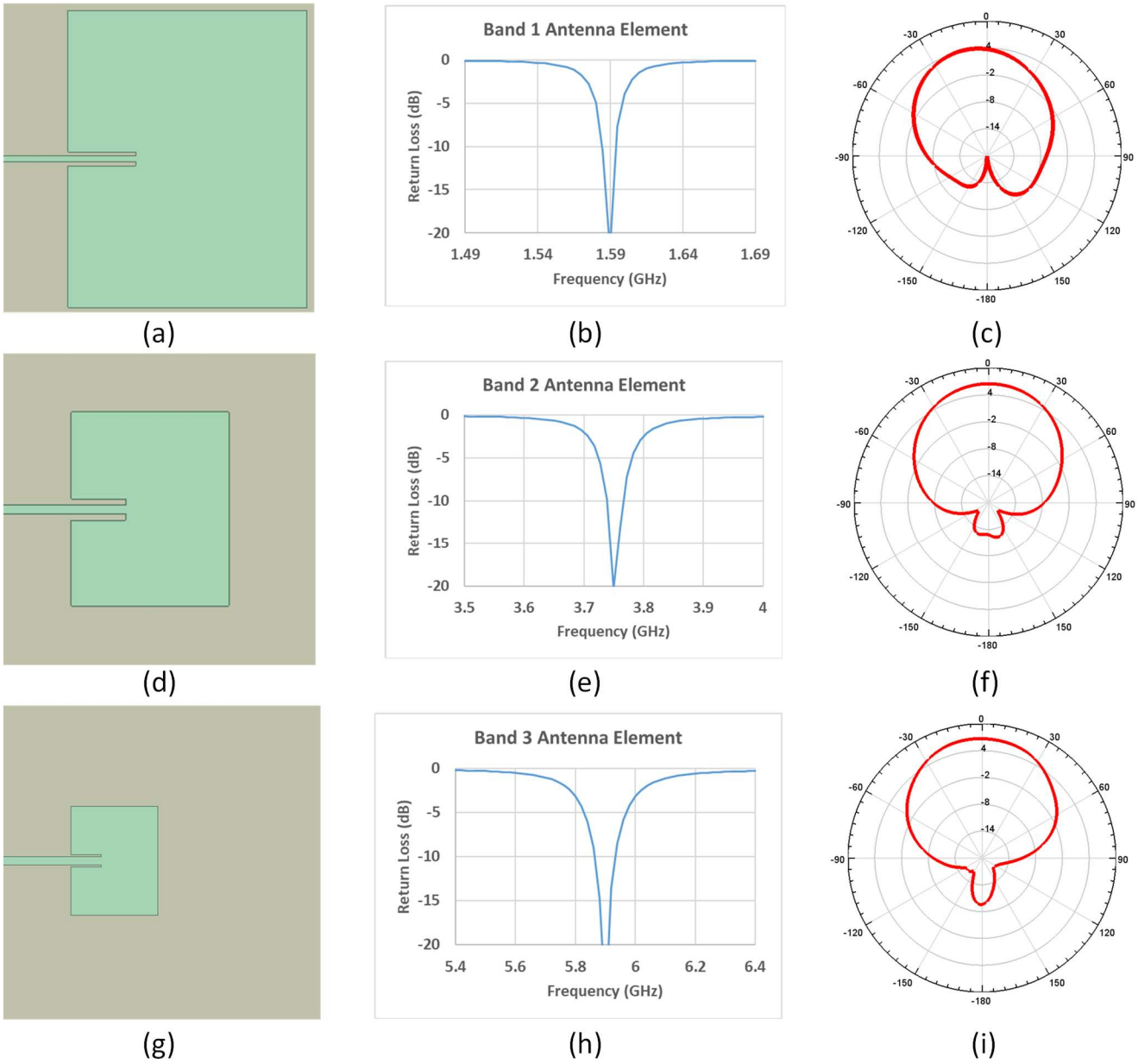


Figure 4-10 Patch antennas simulation: Band 1 a) layout, b) return loss, c) radiation pattern; Band 2 d) layout, e) return loss, f) radiation pattern; and Band 3 g) layout, h) return loss, i) radiation pattern.

bands. It has good performance at the bands of interest, shown in Figure 4-12. There are additional frequencies with good return loss (such as the nulls seen just above and below 3 GHz and around 5.5 GHz) that are not in any of the bands but that does not affect the performance at the bands of interest.

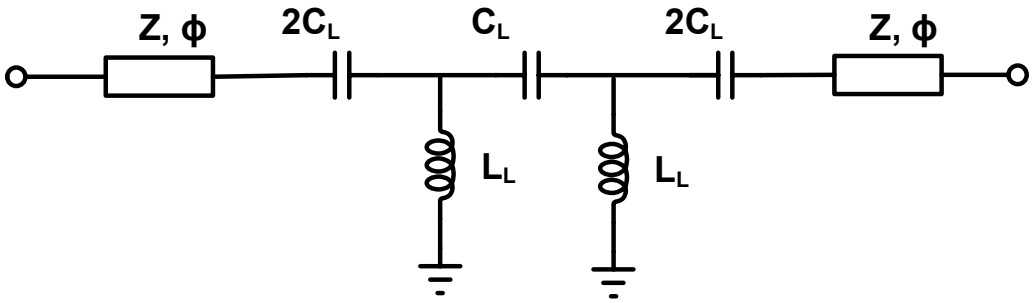


Figure 4-11 Schematic of 5 element CRLH-TL isolation circuit.

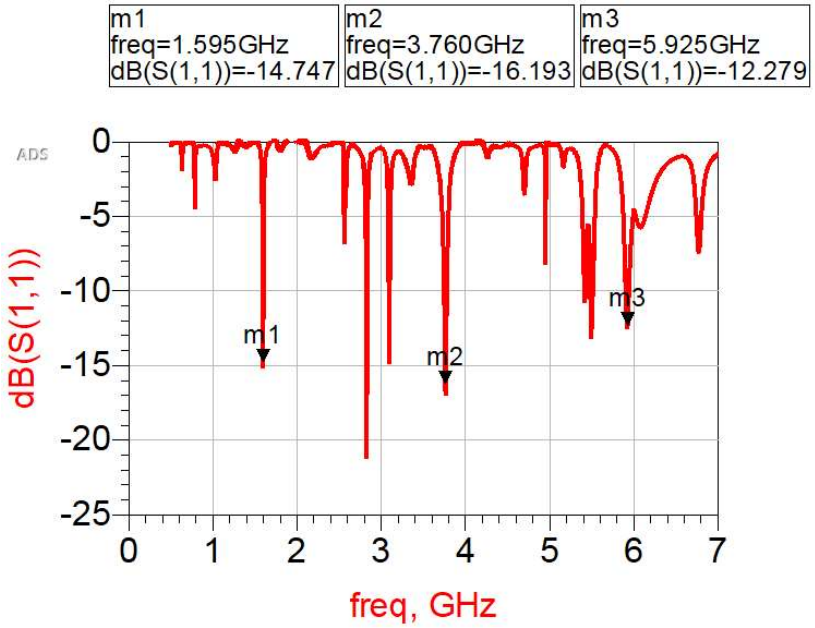


Figure 4-12 Multiplexed antenna feed simulation result.

Each element in the multiplexed antenna feed network can be placed independently. With

multiples of these feed networks, elements of the same band can be spaced uniquely to each other to optimize the performance of the array. The block diagram is shown in Figure 4-13.

### 4.3.3. Fabrication

The full system as well as all the intermediate circuits for design purposes are realized in microstrip technology on Isola Astra substrate ($\varepsilon_r$ = 3.0, Height = 0.508 mm) and using lumped elements for the left handed components of the CRLH-TL isolation circuits. A through-reflect-line (TRL) calibration is used to de-embed the antenna feed to the elements. This type of

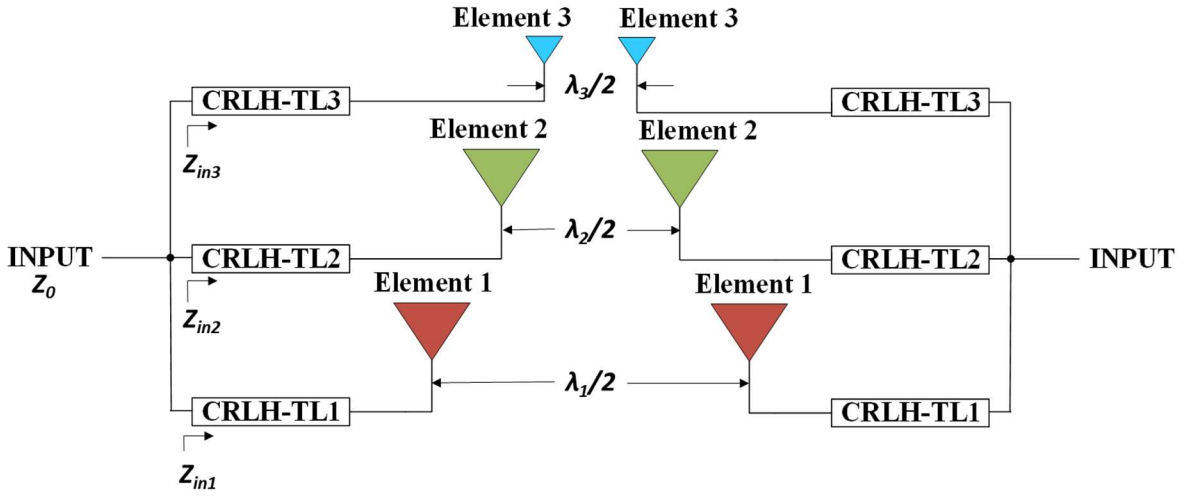


Figure 4-13 Multiband antenna array block diagram.

calibration can eliminate the effects of the connector and feed lines so that the impedance of the antenna element alone. This impedance is then used to properly design the isolation circuits and guarantee first pass yield. A TRL calibration requires unique calibration standards to be created. These are fabricated on the same substrate as the antennas, CRLH-TL and ultimately the final array. There are three types of standards needed; a through, a reflect and a transmission line. The fabricated standards are shown in Figure 4-14.The through standard consists of the connector and

feed lines connected together with no additional line length between them. The reflect standard consists of the connector and feed line terminating in either an open or a short to ground. The line standard is the same as the through standard but with a length of transmission line added. The length of this line determines where the calibration is valid. The electrical length of the line, $\phi$, is defined in Eq. (4.8).

$$\phi = \frac{l}{\lambda} \times 360^{\circ}, \tag{4.8}$$

where $l$ in the physical length of the line, $\lambda$ is the wavelength in the transmission line technology and $\phi$ is in degrees. The electrical length of the line should be between 20˚-160˚ from the low frequency to the high frequency of the valid calibration. A line length of 12.2 mm gives a valid calibration from 0.9-7 GHz which is enough to cover all operating frequencies with guard bands on either side.

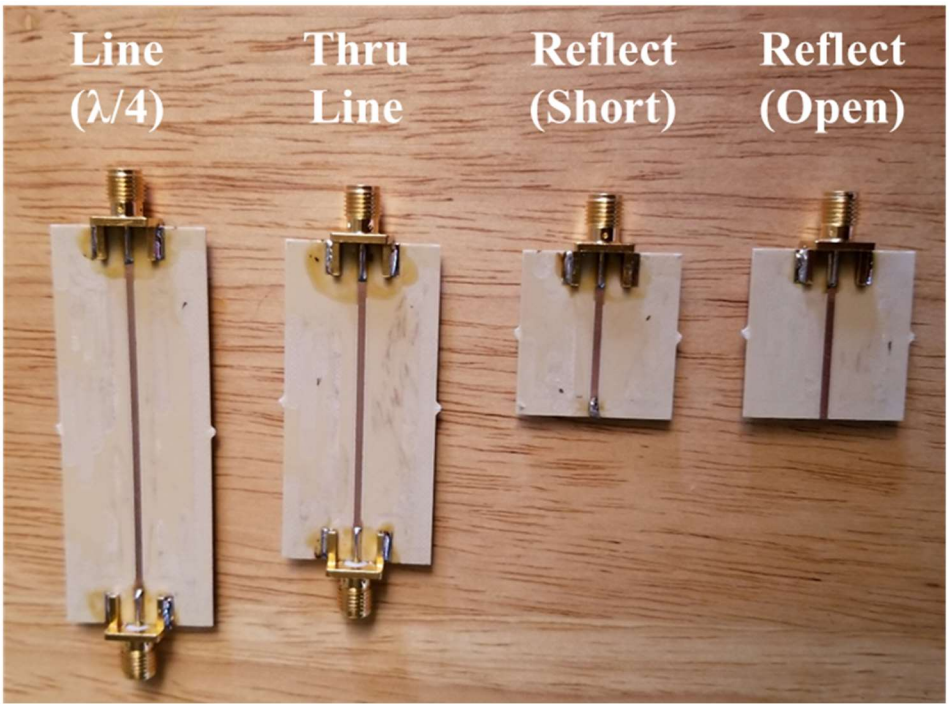


Figure 4-14 TRL calibration standards.

The individual antenna elements are first fabricated. These can be seen in Figure 4-15. The TRL calibration allows the input impedance of the antenna element directly measured. This input impedance is used to determine the exact values needed for the isolation circuits. Then, a circuit that contains the SMT components for the left-handed response of the CRLH-TL's is fabricated. These can be seen in Figure 4-16. These use the same connector and feed line so the response of the left-handed components can be directly measured. This will account for any parasitic due to the SMT components and allow the length of conventional transmission line needed for each isolation circuit to provide the proper isolation. Now the final layout of the multiband array can be configured.

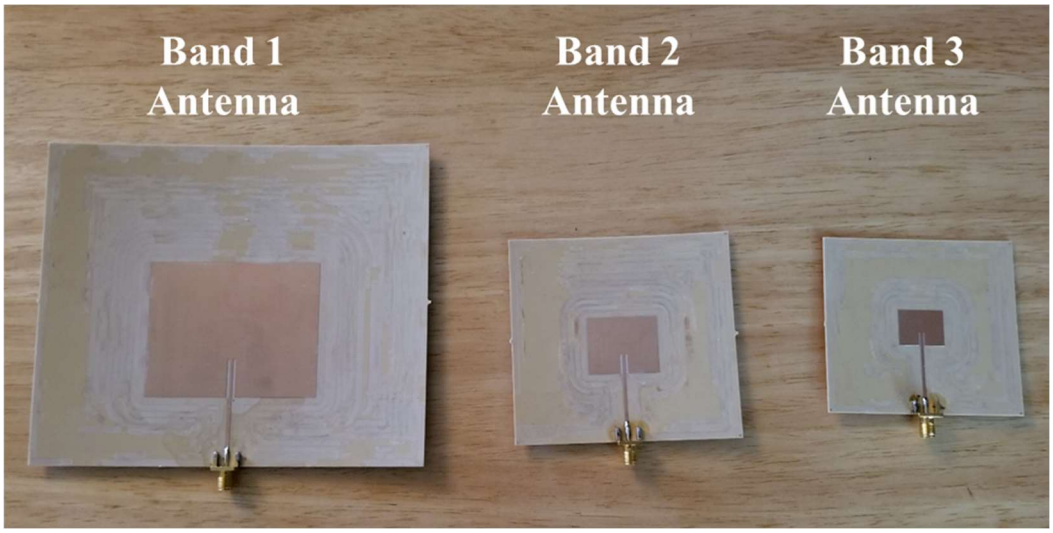


Figure 4-15 Microstrip patch antennas for 1D scanning array.

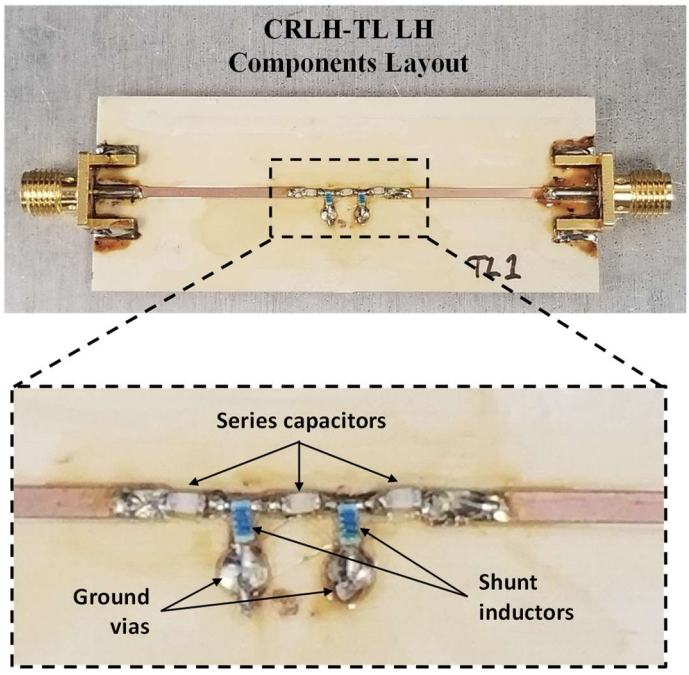


Figure 4-16 SMT componet layout for isolation circuits.

The final layout of the multiband 2x1 linear array composed of multiplexed antenna feeds is shown in Figure 4-17. The antenna elements of each band are first placed at $\lambda_0/2$ in the x direction. With this x spacing fixed, the isolation circuits can be routed to each element adjusting the pairs of the elements in the y direction and meandering the transmission line to accommodate routing.

### 4.3.4. Testing and Measured Results

The fabricated multiband antenna array has been tested. The performance shows good agreement with simulation and the beam steering capability of the array at each of the frequencies is demonstrated.

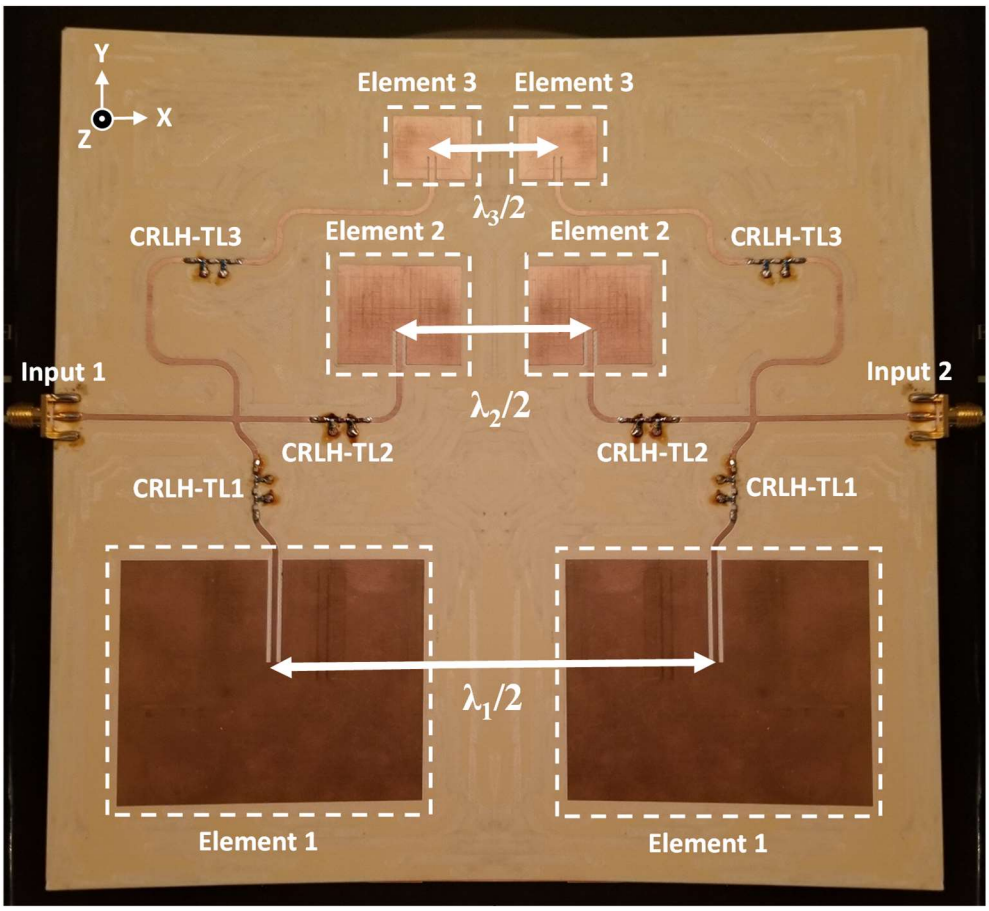


Figure 4-17 Annotated photograph of the fabricated array.

The testing is done in two parts — the S-parameters and the antenna radiation pattern. The S-parameters are simply tested with a network analyzer. This verifies the matching function of the multiplexed antenna feeds. The antenna pattern is measured to verify the operation of the antennas and the beam steering capability of the array and this requires a more elaborate test setup. The test consists of supplying RF power to both branches of the array with different phase differences between ports and using a receiving horn antenna connected to a spectrum analyzer to measure the received power at different rotation angles of the array. The receiving antenna is fixed and the antenna array is rotated around the *y*-axis. The *z*-axis is oriented pointing towards the receiving antenna ($\theta = 0°$) and rotated in both directions until normal to the receiving antenna ($\theta = \pm 90°$).

The far field is the region where the antenna pattern is valid and is the region where measurements need to be made. This minimum distance for the far field region $r$ is defined in Eq. (4.9) from [7] where $D$ is the largest dimension of the antenna and $\lambda_0$ is the wavelength in free space. The distance between the array and the receiving antenna is set to 2 meters which is enough to ensure it is in the far field range for all operating frequencies.

$$r \geq \frac{2D^2}{\lambda_0}, \tag{4.9}$$

The phase difference between the two inputs is varied by ±90° with antenna pattern measurements being taken with -90°, 0° and +90° phase delta between the input ports. This phase difference is enough to steer the beam to the maximum angle achievable with a linear patch array. The block diagram of the test setup is shown in Figure 4-18.

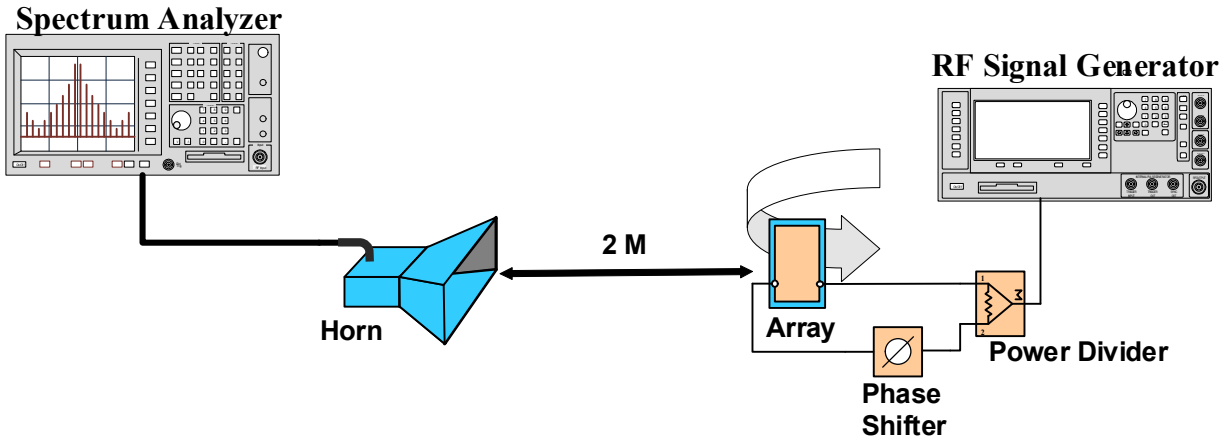


Figure 4-18 Multiplexed antenna array radiation pattern test setup block diagram.

To implement the test, the fabricated antenna array is secured to a backer board to avoid flexing and damaging the panel. The backer board is installed in a vice to hold it perpendicular to the

receiving antenna. An angle finder (Pittsburg Tools 94963) is used to measure the rotation of the array with respect to the receiving antenna and a measurement is taken every 10˚ from -90˚ to +90˚. The phase difference between ports is provided by commercial connectorized power dividers and a coupler. The power dividers (Anaren P/N 40710 for band 1 and ATM P/N P214F bands 2 and 3) are used for the equal phase distribution case and the coupler (Anaren P/N 10350-3 for all bands) is used for the case with 90˚ difference between the ports. A single wide band horn antenna (AEL P/N H-1479) is used for thr reciving antenna. Though an antenna chamber would be ideal for this measurement, one was not available at the time of testing. The test was performed in a lab with any potential interferance moved as far away as possible from the test area. The test setup is shown in Figure 4-19.

Figure 4-19 1D multiplexed antenna array radiation pattern test setup.

The return loss at each input of the array is measured to verify the match at each of the bands. The measurements of the individual antenna elements used for comparison. The return loss results

of each input of the array and the antenna elements are shown in Figure 4-20 a), c) and e). The measurements at each input are consistent and both show good agreement with the measured results of the individual elements. The response of the 5.9 GHz antennas shows a slight shift in frequency in the array compared to the individual antenna element due to the close proximity of the antennas in the array. The return loss measured in band 3 at input 2 is slightly degraded a few dB compared to input 1. This can be attributed to the higher frequency being more sensitive to assembly variations. A return loss of -12 dB is still more than sufficient to demonstrate the concept of the design.

The antenna pattern results are shown in Figure 4-20 b), d) and f). The individual band arrays were modeled and simulated without the other antenna elements for comparison to the full measured system. The measured results show that the main beam has a steering capability of ±30° with side lobe levels -10 dB or better at each band which agrees with the simulated results that are shown as the dashed lines of the same color in the graphs.

### 4.3.5. Conclusion

This method of connecting multiple antennas with one input and its application into a multiband array has been demonstrated successfully. The fundamental theory has been presented with a two element linear array at three operating frequencies and experimental results have shown good agreement with the theory. This procedure allows any resonant antenna elements to be implemented and the placement of these antenna elements to be arbitrarily spaced in an array for each operating band without compromising the power transfer efficiency from the input to the antennas.

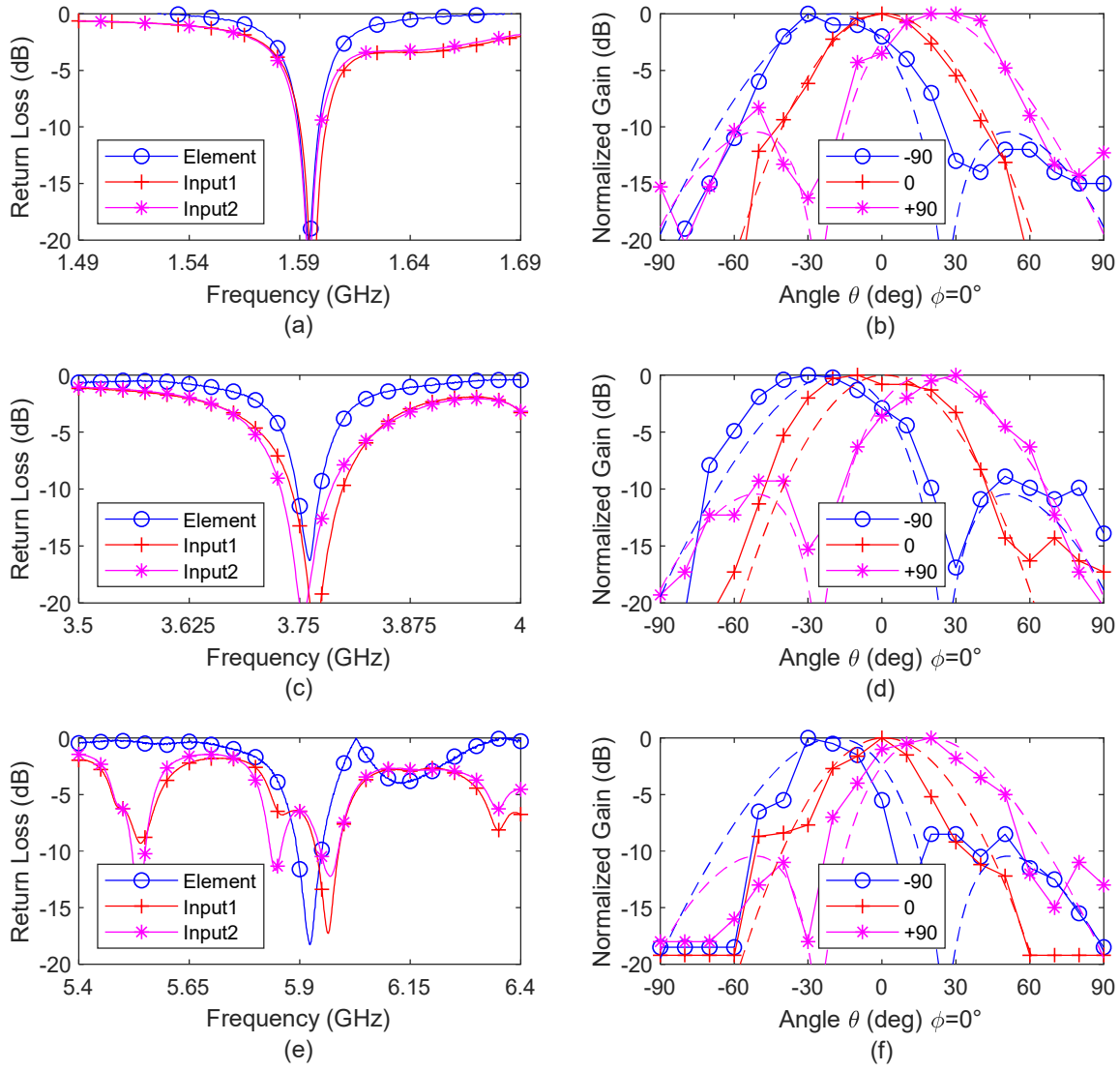


Figure 4-20 Measured results (a) 1.59GHz antenna return loss (b) 1.59GHz antenna pattern (c) 3.75GHz antenna return loss (d) 3.75GHz antenna pattern (e) 5.9GHz antenna return loss (f) 5.9 GHz antenna pattern.

### 4.4. 2D Scanning Antenna Array Comprised of Multiplexed Antenna Feeds

The previous concept can be expanded for 2D scanning by arranging the elements in an M x N configuration. The phase difference between elements can be controlled along 2 axis which will control the beam angle in two dimensions. One drawback to this approach is that the arrays will

take up much more space and would be difficult to implement on the same surface. The feeding network for this configuration would be complicated requiring a stack up with many conductive layers. By using a linear array of LWA's, the frequency scanning capability can be used for beam steering in one direction and using the phase difference between elements for beam steering in the other direction. Linear arrays of LWA's with 2D scanning have been presented in and [51]-[52]. This approach will simplify the layout of a multiband antenna array with multiplexed antenna feeds that will have 2D scanning capability. The design of this type of antenna that is suited for an array with 2D scanning capability is discussed and demonstrated in this section.

### 4.4.1. Antenna Element Design

For the leaky wave structure of the element, a microstrip CRLH-TL is used. The nature of these transmission lines provide phase delay as well as phase advance depending on frequency. This will provide forward and backward radiation and when used in a linear array, will provide full hemisphere scanning.

The CRLH-TL structure used is completely planar. This approach keeps the cost lower and reduces any additional assembly. The left handed series capacitors are printed interdigital capacitors and the left handed shunt inductors are narrow lines tied to ground. This connection to ground is typically achieved with a plated via. This can be difficult to implement without a full board house fabrication capability of creating plated through holes and even with this, it can be a cost driver. This plated through hole is able to be eliminated by using a large metal patch. This patch provides a large capacitance which will look like a short at higher frequencies (virtual ground) and provide this grounding without the need for a plated through hole. This has been previously demonstrated in [53] and [54].

#### 4.4.1.1. CLRH Leaky Wave Antenna

The design of the antenna starts with the unit cell. The equivalent circuit of the proposed LWA unit cell is shown in Figure 4-21a. The CRLH-TL is comprised of the components $C_R$, $C_L$, $C_P$, $L_R$ and $L_L$. The series components ($C_L$ and $L_R$) are realized with interdigital capacitors. The shunt components ($C_R$, $C_P$ and $L_L$) are implemented with inductive stubs terminated in the virtual ground. The microstrip layout along with the dimensions of the unit cell is also shown in Figure 4-21b.

The performance of the unit cell is tuned by adjusting the dimensions $w_i$, $g_i$, $d_i$, $g$, $w_s$, $d_s$, and $p$ so that $\beta$ is operating in the fast wave region (or radiating region, $\beta<k_0$) and with a closed band gap to ensure continuous beam scanning from backward to forward. The simulated performance of the unit cell is seen in Figure 4-22.

The LWA antenna is designed using 5 cascaded unit cells for manufacturability. More unit cells would make the antenna more efficient but would be difficult to handle in testing due to the large size. A prototype of 5 unit cells is sufficient to demonstrate the concept without making it difficult to handle during testing. It is centered at 4.2 GHz for broadside radiation and has continuous beam scanning from backward to forward radiation at 3.9-4.4 GHz. The model of the 5 cell LWA prototype is shown in Figure 4-23.

The simulated return loss of the LWA is shown in Figure 4-24. The return loss is acceptable in the operating band although it was not tuned in for match. This would typically be done with a type of matching network, such as a quarter wave or multi-section transformer, but it was not considered for this prototype due to size concerns. The performance is still within acceptable limits to prove the antenna functionality. The input impedance is shown in the Smith chart in Figure 4-25. The input impedance for Band 1 is on the circumference of the Smith chart, showing that there is almost total reflection, however at Band 3 the input impedance is almost in the center,

showing a nearly perfect match. This will not work in a multiplexed antenna feed application without some additional filtering.

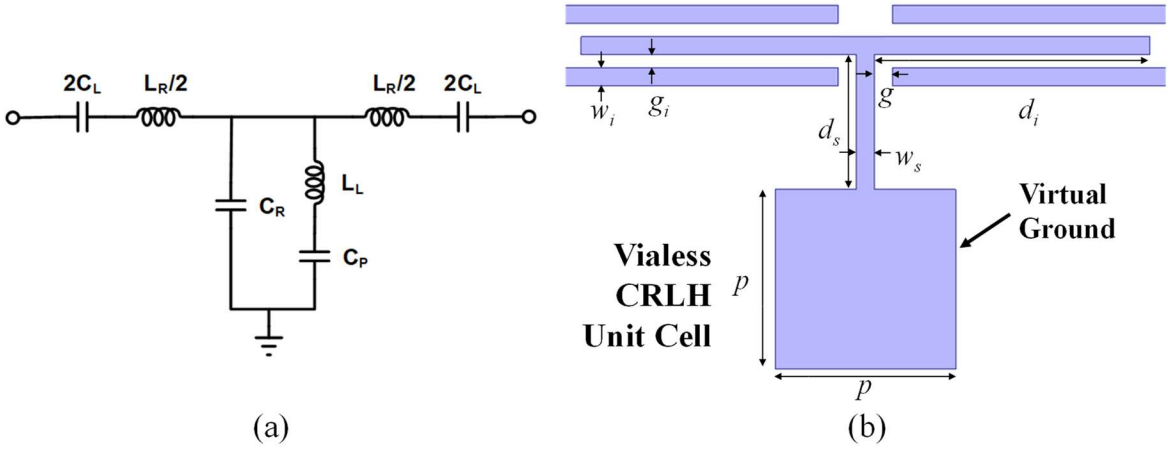


Figure 4-21 Microstrip CRLH leaky wave antenna layout.

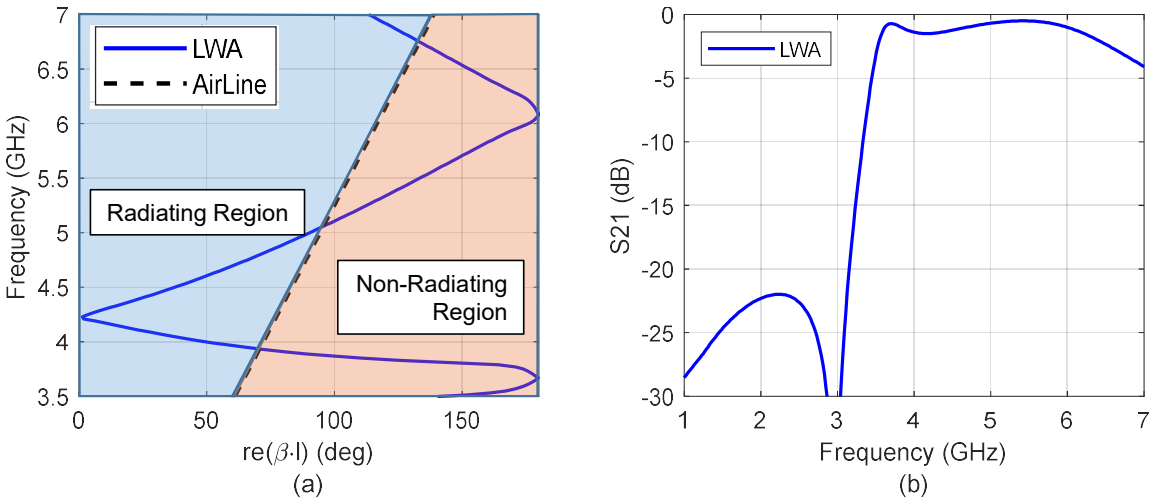


Figure 4-22 LWA unit cell characteristics: a) dispersion diagram and b) rejection.

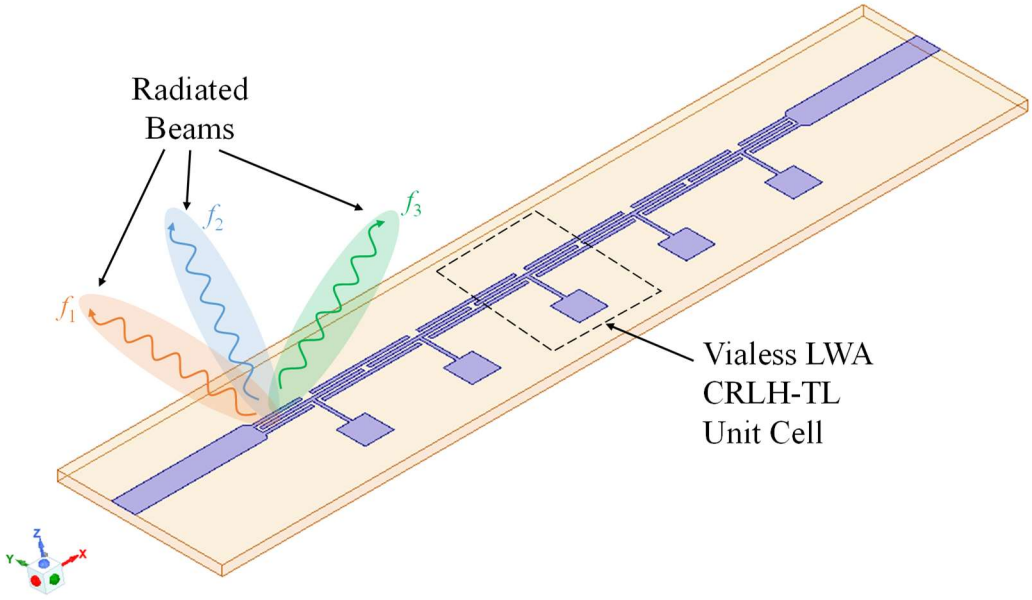


Figure 4-23 CRLH-TL LWA 5 cell prototype.

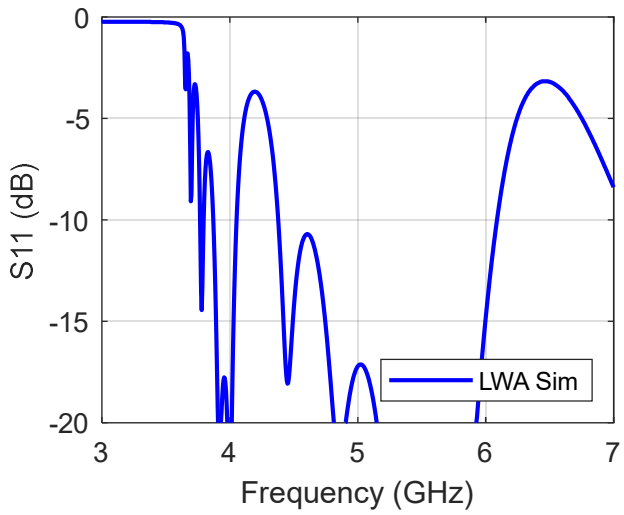


Figure 4-24 CRLH-TL LWA 5 cell prototype simulated return loss.

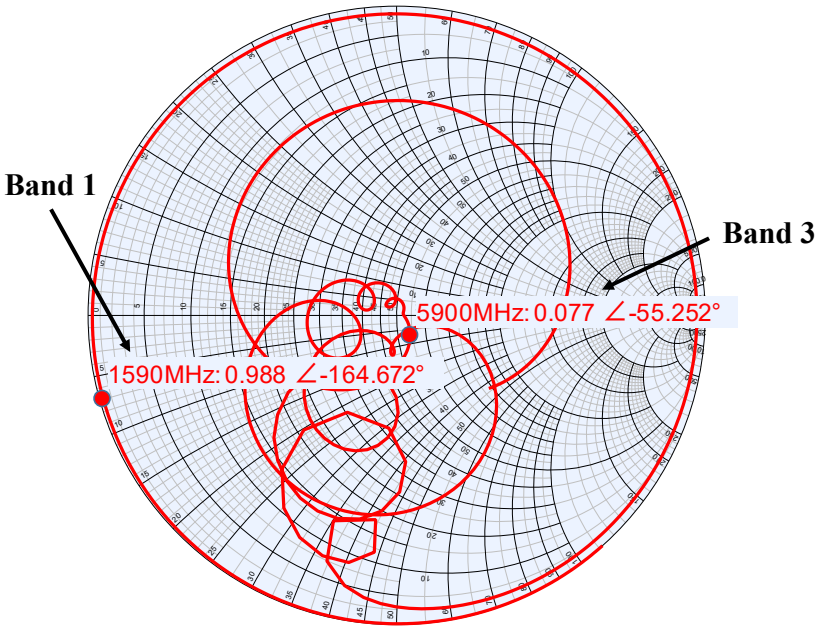


Figure 4-25 CRLH-TL LWA 5 cell prototype simulated input impedance on the Smith chart.

#### 4.4.1.2. CRLH Leaky Wave Filtenna Unit Cell

The LWA from the previous section has the frequency scanning capability needed for the 2D scanning with a linear array but lacks the out of band rejections at the other bands in order to be used in a multiplexed antenna feed. A filter on the input of this antenna could provide this but it would add additional space and complexity. Adding this filtering to the unit cell could achieve the same rejection without increasing the overall size of the antenna.

The equivalent circuit of the standard CRLH-TL unit cell does have the same structure as a band pass filter (BPF) [55]-[56], however the values of the right-hand components ($C_R$ and $L_R$) that control the high side cutoff are very large which push any high side rejection higher in frequency. This works well for a transmission line but not for a band limiting function. Additional features need to be added to the unit cell to achieve this rejection.

The equivalent circuit of the unit cell for the filtering antenna (known as a filtenna) is shown in

Figure 4-26a. The CRLH-TL is comprised of all the components of the LWA unit cell ($C_R$, $C_L$, $C_P$, $L_R$ and $L_L$) with the addition of band stop filtering (BSF) elements ($C_{BSF}$ and $L_{BSF}$). These filtering elements are used to provide a band stop response and give the desired rejection on the high side of the band to the unit cell.

The series components ($C_L$ and $L_R$) are again realized with interdigital capacitors and the shunt components ($C_R$, $C_P$ and $L_L$) are still implemented with inductive stubs terminated in the virtual ground. The BSF elements ($C_{BSF}$ and $L_{BSF}$) are implemented with a narrow spiral line for the inductor with a capacitive patch to ground in the center. The microstrip layout along with the dimensions of the unit cell is shown in Figure 4-26b.

The performance of the unit cell is tuned by adjusting the dimensions $w_i$, $g_i$, $d_i$, $g$, $w_s$, $d_s$, and $p$ so that $\beta$ is operating in the fast wave region (or radiating region, $\beta<k_0$) and with a closed band gap to ensure continuous beam scanning from backward to forward. The dimensions $w_f$, $g_f$ and $p_f$ are tuned to obtain a null at the desired frequency, in this case 5.5 GHz. The simulated performance of the leaky-wave filtenna (LWF) unit cell (as well as the LWA unit cell and the BSF performance) is shown in Figure 4-27.

The LWF is designed using 5 cascaded unit cells for manufacturability, just as the LWA in the previous section. This sacrifices some efficiency for handling concerns. It is centered at 4.2 GHz for broadside radiation and has continuous beam scanning from backward to forward radiation at 3.9-4.3 GHz like the LWA but has improved out of band rejection. The model of the 5 cell LWA prototype is shown in Figure 4-28.

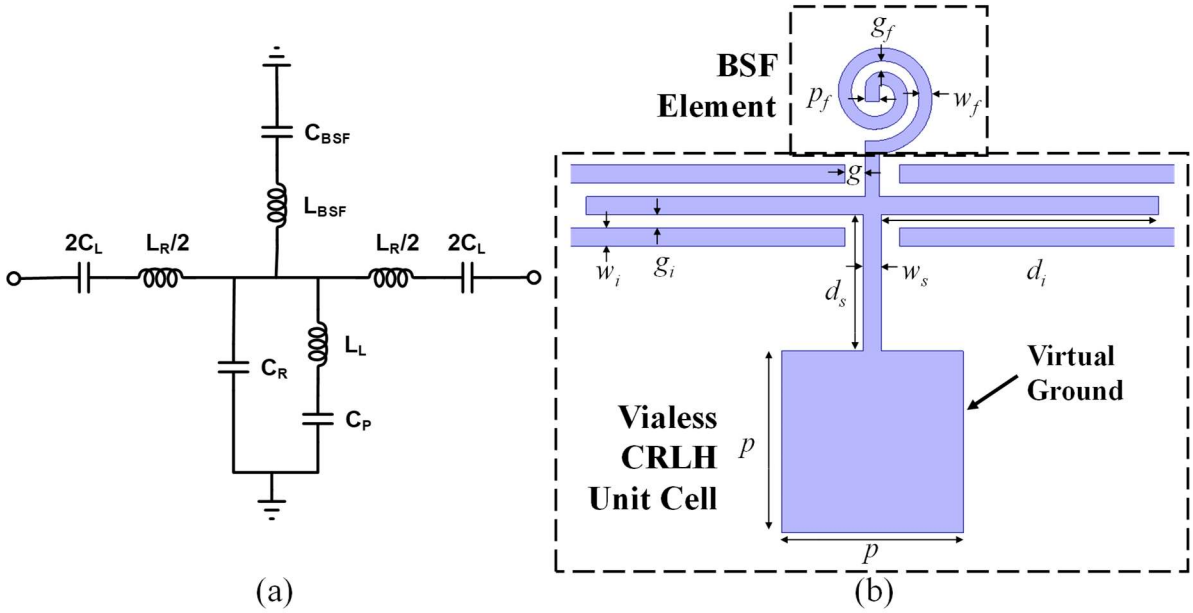


Figure 4-26 Microstrip CRLH leaky wave filtenna layout.

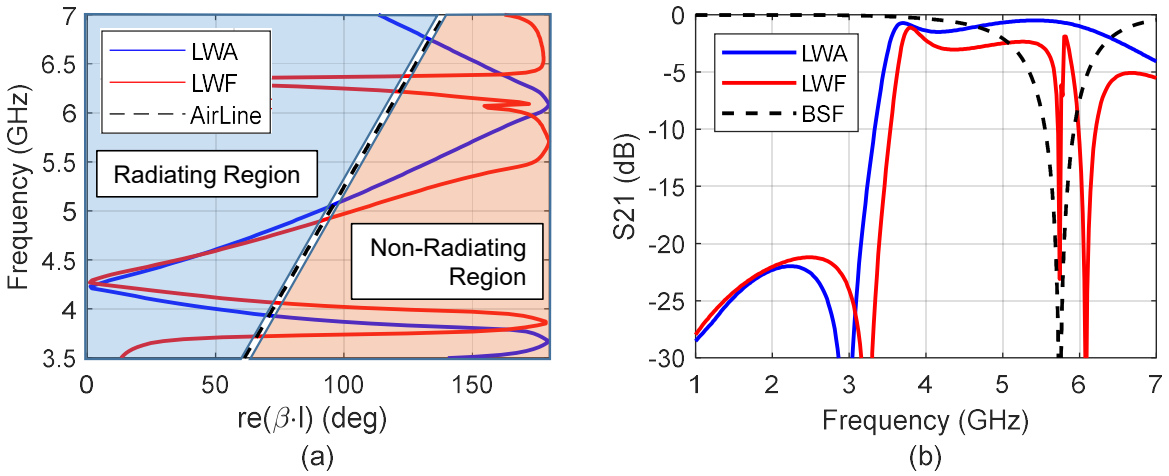


Figure 4-27 LWF unit cell characteristics: a) dispersion diagram and b) rejection.

The simulated return loss of the LWF is shown in Figure 4-29. The return loss is acceptable in the operating band although it was not tuned in for match, just as the LWA. The performance is still within acceptable limits to prove the antenna functionality. The input impedance is shown in the Smith chart in Figure 4-30. The input impedance for the other bands (Band 1 and Band 3) are

on the circumference of the Smith chart, showing that there is almost total reflection and therefore, will work for the multiplexed antenna feed.

The simulated gain of both the LWA and LWF antennas is shown in Figure 4-31. Both antennas have similar gain in band and the LWF has a distinct null of -14 dBc at 5.25 GHz and reduced gain past that compared to the LWA. The normalized radiation pattern for the LWF is shown in Figure 4-32 scanned in the $\theta$ direction for $\phi = 90^\circ$ and $\phi = 0^\circ$. Three separate frequencies are shown in these graphs: 3.9 GHz shown in the blue traces, 4.2 GHz shown in the red traces and 4.3 GHz shown in the green traces. The beam scanning capability is shown in Figure 4-32a when $\phi = 90^\circ$ with an angle of -25˚ at 3.9 GHz to +25˚at 4.3 GHz and broadside radiation at 4.2 GHz. When $\phi = 0^\circ$, as shown in Figure 4-32b, there is no beam scanning capability and the beam is consistent for the three frequencies.

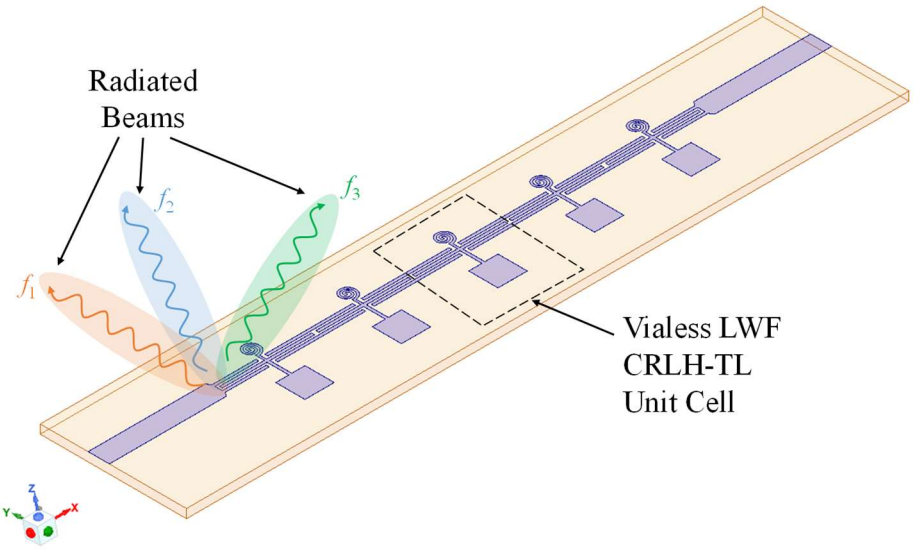


Figure 4-28 CRLH-TL LWF 5 cell prototype.

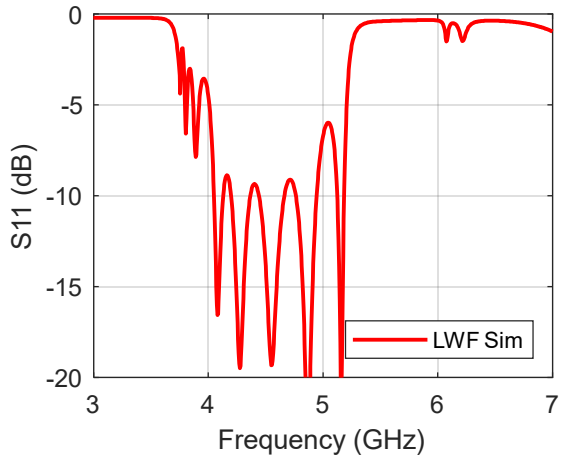


Figure 4-29 CRLH-TL LWF 5 cell prototype simulated return loss.

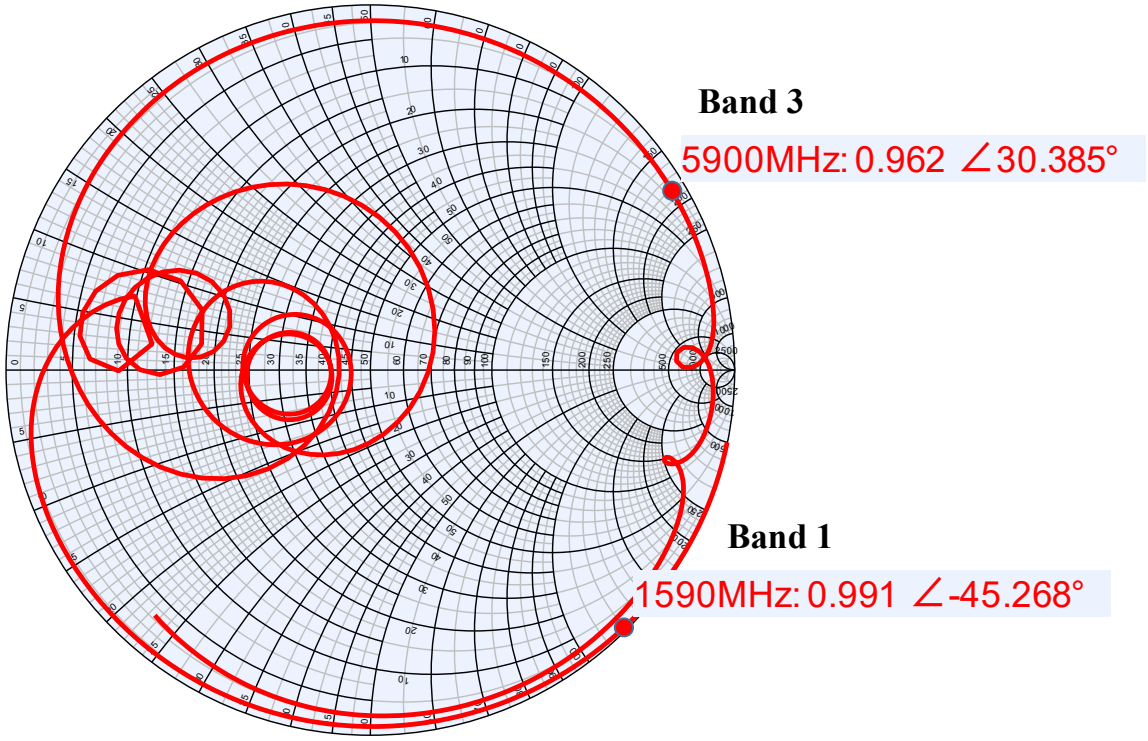


Figure 4-30 CRLH-TL LWF 5 cell prototype simulated input impedance on the Smith chart.

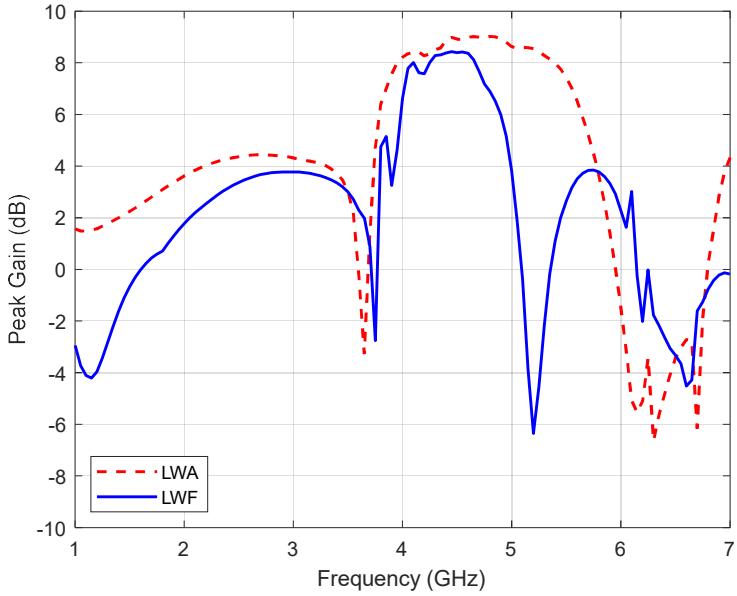


Figure 4-31 Simulated CRLH-TL LWA and LWF gain.

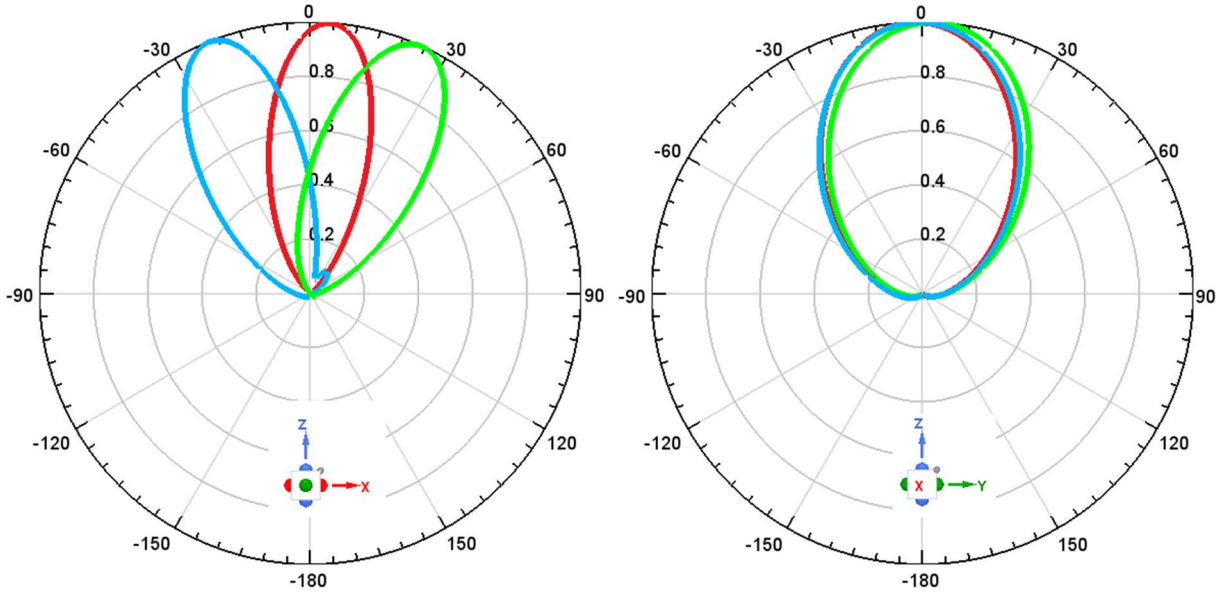


Figure 4-32 Simulated CRLH-TL LWF normalized radiation pattern scanning in $\theta$ with a) $\boldsymbol{\phi}$ = 90˚ and b) $\boldsymbol{\phi}$ = 0˚.

### 4.4.2. Antenna Element Fabrication

The LWF prototype is realized in microstrip technology on Rogers 3003 substrate ($\varepsilon_r$ = 3.0,

Height = 1.524 mm) with soldered edge launch SMA connectors. A LWA designed to the same frequency is also fabricated as a control. The assembled prototypes are shown in Figure 4-33.

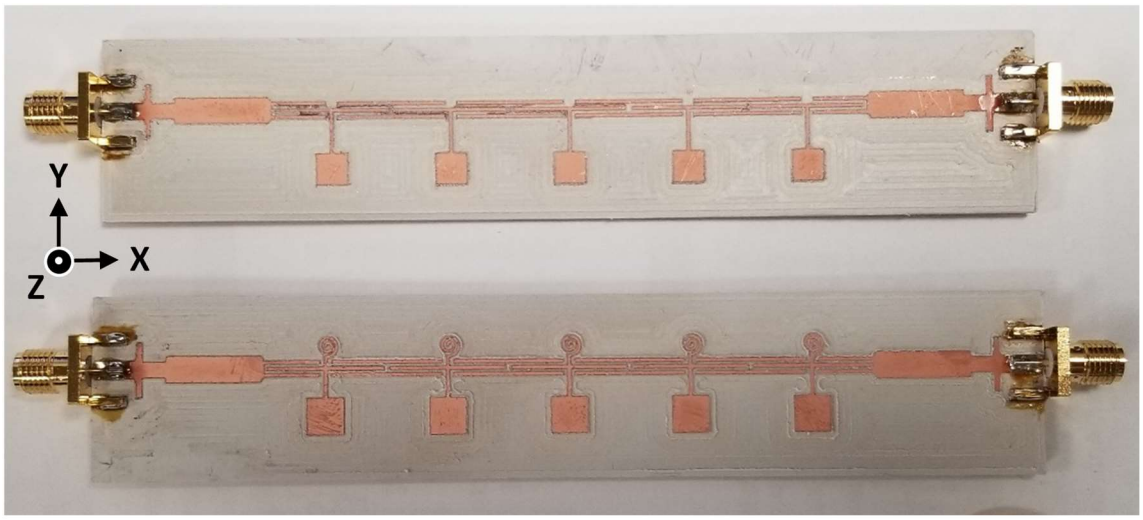


Figure 4-33 Assembled 5-cell LWA (top) and LWF prototype (bottom).

### 4.4.3. Antenna Element Testing and Measured Results

The fabricated band 2 LWA and LWF have been tested. The performance shows good agreement with simulation and the beam scanning capability of the antennas is demonstrated.

The testing is done in two parts — the S-parameters and the antenna radiation pattern. The S-parameters are simply tested with a network analyzer. This verifies the matching of the antennas and the rejection provided from the LWF. The antenna pattern is measured to verify the beam scanning capability of the antennas and this requires a test setup similar to that of the 1D scanning multiband array. The test supplies RF power to the input of the antennas with the second port terminated in 50Ω and using a receiving horn antenna connected to a spectrum analyzer to measure the received power at different rotation angles of the antennas. The receiving antenna is fixed and

the antenna array is rotated around the *y*-axis. The *z*-axis is oriented pointing towards the receiving antenna ($\theta = 0°$) and rotated in both directions until normal to the receiving antenna ($\theta = \pm 90°$). The distance between the measured antenna and the receiving antenna is set to 1 meter. This is large enough to ensure it is in the far field range for the operation frequency (calculated using Eq. (4.9). The input is set to a fixed frequency and the scan angle is swept. This is performed at frequencies for maximum forward and backward radiation angles and for broadside radiation. The block diagram of the test setup is shown in Figure 4-34.

To implement the test, the fabricated antenna is mounted in a holder and rotated in angle towards the receiving antenna. An angle finder (Pittsburg Tools 94963) is used to measure the rotation of the antenna with respect to the receiving antenna and a measurement is taken every 10˚ from -90˚ to +90˚. A single wide band horn antenna (AEL P/N H-1479) is used for the reciving antenna. Though an antenna chamber would be ideal for this measurement, one was not available at the time of testing. The test was performed in a lab with any potential interferance moved as far away as possible from the test area. The test setup is shown in Figure 4-35.

The measured return loss along with the simulated results is shown in Figure 4-36. There is a slight shift of the passband higher in frequency in the measured data compared to the simulated for both antennas. This is likely due to the feature sizes approaching the limit of the fabrication process capability. The LWF shows out-of-band suppression starting around 5.5 GHz compared to the LWA which shows no significant out-of-band suppression up to 7 GHz.

The antenna patterns of both antennas are measured to verify the beam steering capability of the antennas. The results along with the simulated results (displayed as dashed lines of the same color) are shown in Figure 4-37. The scanning is only measured in the $\theta$ direction with $\phi = 90˚$ since this is the dimension in which the beam is scanned. The measured radiation pattern of the

LWF shows beam scanning capability of -10˚ at 4.15 GHz (the blue traces) to +25˚at 4.25 GHz (the green traces) and broadside radiation at 4.2 GHz (the red traces). Similarly, the measured radiation pattern of the LWA shows beam scanning capability of -10˚ at 4.05 GHz (the blue traces) to +25˚at 4.3 GHz (the green traces) and broadside radiation at 4.2 GHz (the red traces). The loss of scan angle of the backward radiation seen in both antennas is because of the shift in passband.

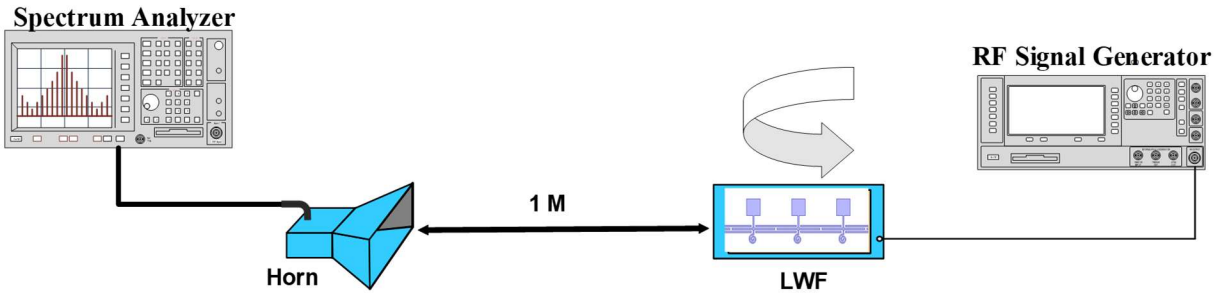


Figure 4-34 LWA and LWF radiation pattern test setup block diagram.

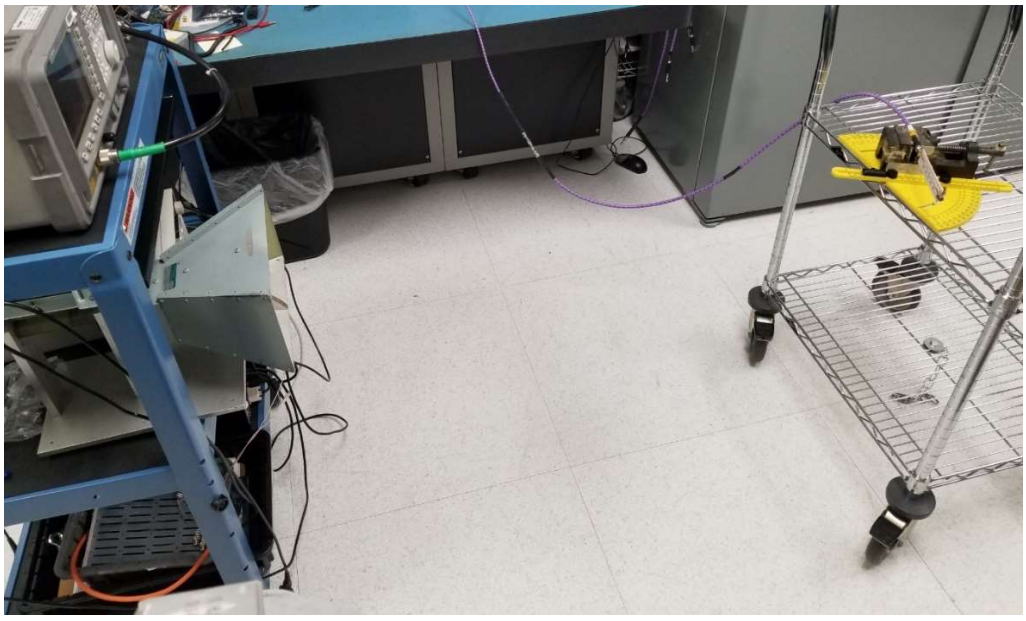

Figure 4-35 LWA and LWF radiation pattern test setup.

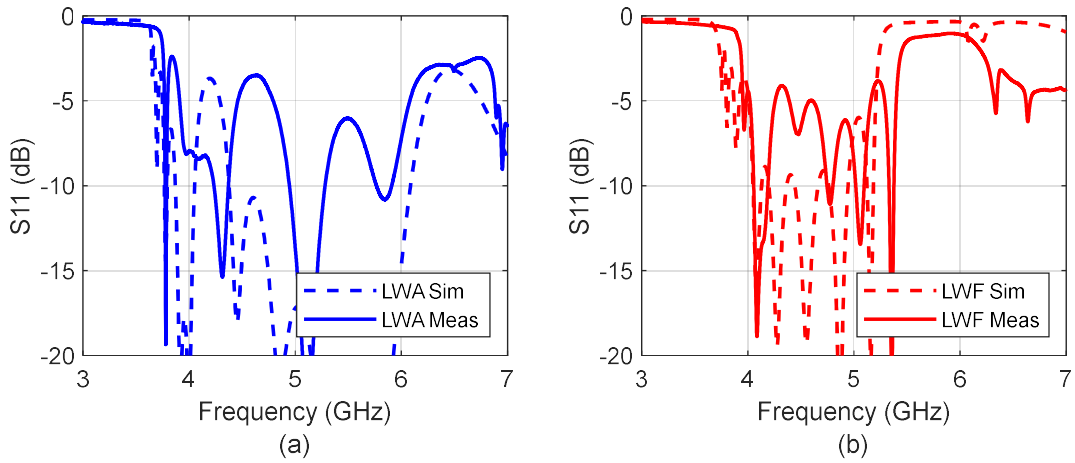


Figure 4-36 Antenna return loss a) LWA and b) LWF.

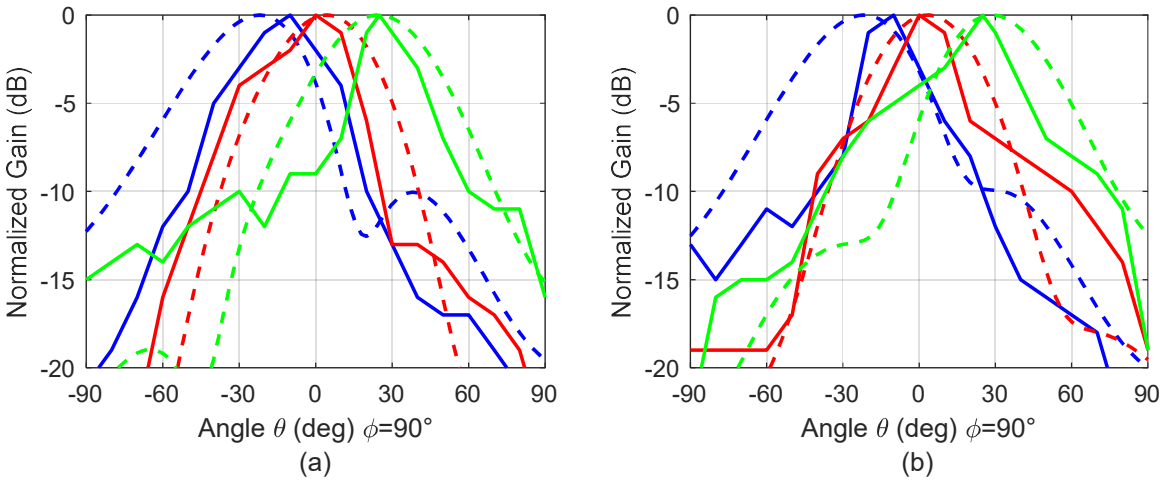


Figure 4-37 Radiation pattern a) LWA b) LWF.

### 4.4.4. Conclusion

A novel way of adding filtering to a LWA has been shown. The LWF was implemented without any vias, simplifying manufacture and without increasing the size of a similar LWA. The high side rejection of the LWF was brought in to around. 5.5 GHz with a gain null of -14 dBc around 5.25 GHz. It has continuous beam scanning from -10˚ to +25˚ from 4.15-4.25 GHz. Both simulated and

measured results are shown. The experimental results have shown good agreement with the theory. With the improved stop band, the antenna can now be used in a multiplexed antenna feed and these can be arranged in linear arrays with 2D beam steering capability.

### 4.5. Multiplexed Antenna Feeds Conclusion

The concept of multiplexing antennas using CRLH-TL isolation circuits and using them in an array has been demonstrated for 1D and 2D scanning capability. The 1D scanning capability was verified with microstrip patch antennas, though any resonant antennas could have been used. The prototype showed beam steering at each band without the introduction of grating lobes. The 2D scanning capability was proposed to be done with LWA in order to maintain the use of a linear arrangement of elements. A LWA needs better out of band rejection in order to be used with the multiplexed antenna feeds. A LWF prototype was designed that has the beam scanning capability of a LWA as well as providing the out of and rejection needed to make it suitable for application in the multiplexed antenna feeds.

# Chapter 5. Conclusions

The Knochel-Mayer power divider is well suited for planar beamforming design and is often used in beamforming applications that require high power handling or layout flexibility. This power divider can operate with 30% bandwidth and work well for antenna array applications with single element spacing. The research presented simplifies and expands the original design to include versions of *N*-way, unequal split and wider bandwidth cases. Each of these was analyzed and demonstrated with tested prototypes. A 4-way Knochel-Mayer was fabricated with a multilayer board solution with interconnects between layers, an unequal split 2-way with a 2:1 power split ratio was fabricated in microstrip and 2-way Knochel-Mayer with wider bandwidth was also fabricated in microstrip. The 4-way prototype presented the concept of the N-way divider. The performance showed good match at each of the ports and good isolation between them for around 35% bandwidth. The 2:1 unequal split prototype presented the concept of the unequal split divider. The performance showed good match at each of the ports and good isolation between them for around 35% bandwidth. The proper amplitude split was also maintained throughout this bandwidth. And a wider bandwidth Knochel-Mayer prototype presented the concept of expanded the bandwidth by adding additional sections to the input and isolation networks. The bandwidth in this case was able to be expanded to 50%. The performance showed good match at each of the ports and good isolation between them for this 50% bandwidth. In addition, this was also demonstrated to handle 10W of power, showing that the power handling capability of the original Knochel-Mayer was preserved. Also, a design that is capable of achieving 60% BW was verified through simulation, though not fabricated due to narrow line requirements.

The added versatility of the Knochel-Mayer presented in this research makes this component more useful in beamforming applications. The reduced footprint size of the *N*-way allows for more

area in the available space for more circuitry and the unequal split capability allows for tapering schemes to be implemented to reduce side lobes.

Future research of the Knochel-Mayer could include expanding the unequal split to include multiple outputs (an *N*-way unequal split Knochel-Mayer). This would present this function in a smaller footprint and save space in the layout. Another area to further the research is to overcome the manufacturing limitation of narrow linewidths needed to the ultra-wideband Knochel-Mayer. Increasing the impedance of these lines electrically without making them more narrow (such as with a defective ground structure) could make these producible.

For antenna arrays with operating bandwidths that are larger than 30%, single element spacing cannot be used without degradation of the array. A solution to use multiple antennas connected with multiplexed feed networks to create antenna arrays is proposed. It uses CRLH-TL isolation circuits to directly multiplex the antennas without needing a separate filter. A 3 band antenna array covering 115% bandwidth with 1D scanning capability was demonstrated using microstrip patch antennas in a linear arrangement. This was able to steer the beam in ±30˚ one dimension without grating lobes and had good match at the input for all bands.

The multiplexed antenna feed concept was expanded to a scheme capable of 2D scanning. It achieves this, maintaining its linear arrangement of elements and using leaky-wave antennas (LWAs). This provides beam steering in one direction with the phase between elements (like in the 1D case) and beam steering in the other direction with the frequency scanning capability of the LWA. The design of LWAs does not have sufficient out of band rejection like the resonant antennas that were used in the 1D case. A novel design of a LWA with suitable out of band rejection was demonstrated. This combined the performance of the LWA with the performance of a band pass filter to create a leaky-wave filtenna (LWF). This was done by modifying the unit cell

of the LWA by adding filtering elements to it so the overall size of the antenna was not significantly increased. The fabricated LWF showed the same antenna performance of the LWA but with the necessary rejection to be implanted in the multiplexed antenna feeds. This type of antenna can be used to implement the 2D beam scanning using the multiband antenna feeds.

A possible future research for the multiplexed antenna feeds is to eliminate the lumped elements in the isolation circuits. This will eliminate the cost of the components and simplify the assembly. Higher frequencies for the isolation circuits could also be achieved from removal of the lumped components and their associated parasitic elements. The CRLH-TL could be implemented in a planar configuration. This would be entirely planar and the same concept that removed the vias of the traditional CRLH-TL used in the LWF could be used as well. This would have to be a structure such as stripline to avoid unwanted radiation like in microstrip but would make a very cost effective design.

# References


[1] M. J. Skolnik, *Introduction to Radar Systems*, 3rd Ed., New York: McGraw-Hill, 2001.

[2] G. W. Stimsom, *Introduction to Airborne Radar*, 2nd Ed., NC: Scitech, 1998.

[3] R. C. Johnson, *Antenna Engineering Handbook*, 3rd Ed., New York: McGraw-Hill, 1993.

[4] R. Knochel and B. Mayer, "Broadband printed circuit 0°/180° couplers and high power inphase power dividers," *IEEE MTT-S Int. Microw. Symp. Dig.*, May 1990, pp. 471–474.

[5] Tahim, R. S., Foshee, J., and Chang, K., "Multiband radar for homeland security," in Sensors and Command, Control, Communications, and Intelligence (C3I) Technologies for Homeland Security and Homeland Defense III, 2004, vol. 5403, pp. 661–672.

[6] W. L. Stutzman, and G. A. Thiele, *Antenna Theory and Design*, 3rd Ed., New York: Wiley, 2013.

[7] C. A. Balanis, *Antenna Theory – Analysis and Design*, *3rd Ed.*, Hoboken, New Jersey: Wiley, 2005.

[8] Naval Air Warfare Center Weapons Division, Electronic Warfare and Radar Systems Engineering Handbook, 2013.

[9] R. L. Haupt, "Factors that define the bandwidth of a phased array antenna," *2019 IEEE International Symposium on Phased Array System & Technology (PAST)*, 2019, pp. 1-4.

[10] P. Delos, B. Broughton and J. Kraft, "Phased Array Antenna Patterns—Part 3: Sidelobes and Tapering," Analog Dialog, Vol. 54, No. 3, July 2020.

[11] J. Butler and R. Lowe, "Beamforming matrix simplifies design of electronically scanned Antennas," *Electron. Design*, Vol. 9, No. 7, pp. 170-173, April 1961.

[12] W. Rotman and R. Turner, "Wide-angle microwave lens for line source applications," in *IEEE Trans. Antennas Propag.,* 1963, 11, (6), pp. 623– 632.

[13] D. R. Jackson, C. Caloz and T. Itoh, "Leaky-Wave Antennas," in *Proceedings of the IEEE*, vol. 100, no. 7, pp. 2194-2206, July 2012.

[14] V. G. Veselago, "The electrodynamics of substances with simultaneously negative values of ε and μ," *Soviet Physics Uspekhi*, vol. 10, no. 4, p. 509, 1968.

[15] C. Caloz and T. Itoh, "Application of the transmission line theory of left-handed (LH) materials to the realization of a microstrip "LH line," *IEEE Antennas and Propagation Society International Symposium (IEEE Cat. No.02CH37313)*, San Antonio, TX, USA, 2002, pp. 412-415 vol.2.

[16] C. Caloz and T. Itoh, *Electromagnetic Metamaterials, Transmission Line Theory and Microwave Applications*, New York: Wiley, 2005.

[17] E. J. Wilkinson, "An N-way hybrid power divider," in *IRE Trans. Microw. Theory Techn.*, vol. 8, no. 1, pp. 116–118, Jan. 1960.

[18] U. H. Gysel, "A new N-way power divider/combiner suitable for high-power applications", *IEEE MTT-S Int. Microw. Symp. Dig.*, May 1975, pp. 116–118.

[19] F. Wang and H. Wang, "An N-Way transformer based Wilkinson power divider in CMOS," in *IEEE MTT-S Int. Microw. Symp. (IMS).*, May 2016, pp. 1-4.

[20] H. Beshary, I. A. Eshrah, M. A. Y. Abdalla and A. N. Mohieldin, "A compact low-loss on-chip N-way Wilkinson power divider for mm-wave 5G applications," *2020 IEEE 63rd International Midwest Symposium on Circuits and Systems (MWSCAS)*, 2020, pp. 444-447.

[21] N. Zhang, B. Wu, X. Wang, Z. Ma and C. -p. Chen, "Design approach of N-way Wilkinson power divider with complex isolation units," *2020 IEEE MTT-S International Wireless Symposium (IWS)*, 2020.

[22] D. S. Beyragh, S. Abnavi, and S. R. Motahari, "Implementation of N-way Gysel combiners using back to back microstrip structure," *Proc. IEEE Int. Conf. Ultra Wide-Band (ICUWB)*, Sep. 2010, vol. 2, pp. 1–4.

[23] F. Ardemagni, "An optimized L-band eight-way Gysel power divider-combiner," in *IEEE Trans. Microw. Theory Techn.*, vol. 31, no. 6, pp. 491–495, Jun. 1983.

[24] Y. Taryana, V. E. Bowo, Y. Sulaeman, P. K. Deni and T. Praludi, "Four way power divider using Wilkinson method for X-band radar," *2019 International Conference on Radar, Antenna, Microwave, Electronics, and Telecommunications (ICRAMET)*, Tangerang, Indonesia, 2019, pp. 41-45.

[25] S. -H. Javid-Hosseini, P. Toofanzadeh and V. Nayyeri, "Planar N-way power combiner with high isolation between input ports," *2021 51st European Microwave Conference (EuMC)*, London, United Kingdom, 2022, pp. 83-86.

[26] A. A. M. Saleh, "Planar electrically symmetric N-way hybrid power dividers/combiners," in *IEEE Transactions on Microwave Theory and Techniques*, vol. 28, no. 6, pp. 555-563, Jun. 1980.

[27] S. Cheng and M. Pavlick, "Synthesis of an N-way arbitrary power divider," *2017 47th European Microwave Conference (EuMC)*, Nuremberg, Germany, 2017, pp. 392-395.

[28] O. Hussein, K. A. Shamaileh, V. Devabhaktuni and P. Aaen, "Wideband impedance-varying N-way Wilkinson power divider/combiner for RF power amplifiers," *2016 88th ARFTG Microwave Measurement Conference (ARFTG)*, Austin, TX, USA, 2016, pp. 1-4.

[29] P. Toofanzadeh, S. -H. Javid-Hosseini and V. Nayyeri, "Printed circuit board implementation of N-way power combiner with isolated input ports," in *IEEE Access*, vol. 10, pp. 46128-46135, 2022.

[30] C. Li, L. Xu and H. Zhang, "A 4:1 unequal Wilkinson power divider using defected ground structure and short-circuited stub," *2019 International Applied Computational Electromagnetics Society Symposium - China (ACES)*, 2019, pp. 1-2.

[31] Ö. Kasar, "A new design for unequal way Wilkinson power dividers: Euler method approach," *2020 12th International Conference on Electrical and Electronics Engineering (ELECO)*, 2020, pp. 68-70.

[32] Y. Wu, Y. Liu and S. Li, "A modified Gysel power divider of arbitrary power ratio and real terminated impedances," in *IEEE Microwave and Wireless Components Letters*, vol. 21, no. 11, pp. 601-603, Nov. 2011.

[33] H. Chen, Y. Zhou, T. Zhang, W. Che and Q. Xue, "N-way Gysel power divider with arbitrary power-dividing ratio," in *IEEE Transactions on Microwave Theory and Techniques*, vol. 67, no. 2, pp. 659-669, Feb. 2019.

[34] S. Oh *et al*., "An unequal Wilkinson power divider with variable dividing ratio," *2007 IEEE/MTT-S International Microwave Symposium*, Honolulu, HI, USA, 2007, pp. 411-414.

[35] A. Mestezky, H. Matzner and E. Levine, "N-way unequal power divider with balanced excitation," *2013 7th European Conference on Antennas and Propagation (EuCAP)*, Gothenburg, Sweden, 2013, pp. 1816-1819.

[36] W. Choe and J. Jeong, "N-way unequal Wilkinson power divider with physical output port separation," in *IEEE Microwave and Wireless Components Letters*, vol. 26, no. 4, pp. 243-245, April 2016.

[37] H. Fan, X. Liang, J. Geng, R. Jin and X. Zhou, "Reconfigurable unequal power divider with a high dividing ratio," in *IEEE Microwave and Wireless Components Letters*, vol. 25, no. 8, pp. 514-516, Aug. 2015.

[38] Rogers Corporation, "Data sheet and processing guide for RO4450B and RO4450F prepregs," RO1.4400, 2008.

[39] D. M. Pozar, *Microwave Engineering*. MA: Addison-Wesley, 1990.

[40] K. Yang, X. Bao and M. J. Ammann, "A back-to-back beam switching microstrip patch antenna," *2015 Loughborough Antennas & Propagation Conference (LAPC),* 2015, pp. 1-4.

[41] Y. Li and Z. Hao, "A wideband switched beam antenna for full 360 coverage," *2017 Sixth Asia-Pacific Conference on Antennas and Propagation (APCAP)*, 2017, pp. 1-3.

[42] A. Lamminen, J. Säily, M. Kaunisto, M. Pokorný, J. Aurinsalo and Z. Raida, "Gain enhanced millimetre-wave beam-switching Rotman lens antenna designs on LCP," 2017 11th European Conference on Antennas and Propagation (EUCAP), 2017, pp. 2781-2785

[43] Young-Jun Kim, Ye-Bon Kim, Hyun-Jun Dong, Yong Soo Cho and Han Lim Lee, "Compact switched-beam array antenna with a Butler matrix and a folded ground structure," *MDPI Electronics*, 2020.

[44] A. Nguyen and Park Seoong Ook, "Compact switched and reconfigurable 4-ports beam antenna array for MIMO applications," *2011 IEEE MTT-S International Microwave Workshop Series on Intelligent Radio for Future Personal Terminals*, 2011, pp. 1-3.

[45] H. Lee and T. Itoh, "Dual band isolation circuits based on CRLH transmission lines for triplexer application," 2011 *Asia-Pacific Microwave Conference*, pp. 542-545, Dec. 2011.

[46] M. D. Enders and J. H. Choi, "3D space-to-microwave frequency mapping antenna," *2016 IEEE International Symposium on Antennas and Propagation (APSURSI)*, Fajardo, PR, USA, 2016.

[47] Tokio Kaneda, Atsushi Sanada and Hiroshi Kubo, "Design of an 8-element planar composite right/left-handed leaky wave antenna array for 2-D beam steering," *2006 Asia-*

*Pacific Microwave Conference*, Yokohama, Japan, 2006, pp. 1067-1070.

[48] H. Lee and T. Itoh, "Size reduced dual-band isolation circuits using hybrid right-handed transmission Lines for triplexers," *2012 Asia Pacific Microwave Conference Proceedings*, Kaohsiung, Taiwan, 2012, pp. 76-78.

[49] A. Sanada, C. Caloz and T. Itoh, "Characteristics of the composite right/left-handed transmission lines," in *IEEE Microwave and Wireless Components Letters*, vol. 14, no. 2, pp. 68-70, Feb. 2004.

[50] Y. Huang and K. Boyle, *Antennas: From Theory to Practice*, 2nd Ed., New York: Wiley, 2021.

[51] Cheng-Chi Hu, C. F. Jou and Jin-Jei Wu, "A two-dimensional beam-scanning linear active leaky-wave antenna array," in *IEEE Microwave and Guided Wave Letters*, vol. 9, no. 3, pp. 102-104, March 1999.

[52] C. A. Allen, K. M. k. h. Leong and T. Itoh, "2-D frequency-controlled beam-steering by a leaky/guided-wave transmission line array," *2006 IEEE MTT-S International Microwave Symposium Digest*, San Francisco, CA, USA, 2006.

[53] A. Sanada, K. Murakami, S. Aso, H. Kubo and I. Awai, "A via-free microstrip left-handed transmission line," *2004 IEEE MTT-S International Microwave Symposium Digest (IEEE Cat. No.04CH37535)*, Fort Worth, TX, USA, 2004.

[54] J. H. Choi, C. -T. M. Wu, H. Lee and T. Itoh, "Vialess composite right/left-handed stripline and its applications for broadband 3-dB and tunable couplers," *2014 44th European Microwave Conference*, Rome, Italy, 2014.

[55] B. E. Spielman et al., "Metamaterials face-off [Speaker's Corner]," in *IEEE Microwave Magazine*, vol. 10, no. 3, pp. 8-42, May 2009.

[56] C. Caloz and T. Itoh, "Novel microwave devices and structures based on the transmission line approach of meta-materials," *2013 IEEE MTT-S International Microwave Symposium Digest*, 2003, pp. 195-198 vol.1.

## VITA

Jeremy Michael Furgal was born May 16, 1977 in Syracuse, NY and currently resides in Fulton, NY.

## Academic Degrees

2012 *Master of Science in Electrical Engineering with specialty in Microwave Engineering*

Syracuse University, Syracuse, NY

2007 *Bachelor of Science in Electrical Engineering*

Syracuse University, Syracuse, NY

## Publications

J. Furgal, K. Xu, J. H. Choi and J. K. Lee, "Broadband equal-split planar 4-way power divider/combiner suitable for high power applications," *2020 50th European Microwave Conference*, pp. 840-843, 2021.

J. Furgal, H. Lee, J. H. Choi and J. K. Lee, "Multi-band array using a multiplexed antenna feed composed of CRLH transmission line-based dual band isolation circuits," *2021 IEEE International Symposium on Antennas and Propagation*, Singapore, Singapore, Dec. 2021.

J. Furgal, J. H. Choi and J. K. Lee, "Bandwidth enhanced equal-split planar Knochel-Mayer power divider capable of high power handling for antenna feed applications," *2022 IEEE International Symposium on Antennas and Propagation and USNC-URSI Radio Science Meeting (AP-S/URSI)*, Denver, CO, USA, 2022.

J. Furgal, J. H. Choi and J. K. Lee, “Microstrip CRLH-TL leaky wave filtenna for multiplexed antenna feed applications," *2023 IEEE International Symposium on Antennas and Propagation*, Portland, OR, July 2023.

## Professional Employment

2008 - Present: Sr. RF/Microwave Engineer, TTM Technologies (formerly Anaren), East Syracuse, NY.

2007 - 2008: Electrical Project Engineer, HMT Inc., Cicero, NY.

2006 - 2007: Electrical Engineering Intern, SRC, Inc., North Syracuse, NY.

2006 - 2006: Electrical Engineering Intern, E/PRO, Liverpool, NY.

**Professional Membership**

2014 - Present: IEEE (Institute of Electrical and Electronics Engineers) Member